Investigation of hydrocarbon stapled alpha-helical peptides as a novel method to interrupt protein-target interactions in bacteria

By

Daniel I. Pau

DISSERTATION

A thesis submitted to the Faculty of Science

In partial fulfillment of the requirements

Of a Master's of Science in

CHEMISTRY

At the University of Ottawa

September 30, 2015

University of Ottawa

Department of Chemistry and Biomolecular Sciences

Ottawa, ON, Canada

K1N 6N5

Approved: _____

Professor Christopher N. Boddy

Date: _____

Abstract

With the increasing threat of multidrug resistant bacteria, there is a growing need to invent new drug classes that combat untreatable infections. Small molecule antibiotics have been successful in the past, but humanity is now losing the arms race against previously treatable pathogens. However, the number of clinically approved drugs targeting traditionally undruggable targets in bacteria remains low. New targets of complex protein-target interactions must be targeted for future pharmacological development. In an effort to create clinically viable biologics, the Verdine lab has developed a class of therapeutics called hydrocarbon stapled α-helical peptides; these peptides are known to affect protein-protein interactions by retaining secondary structure *in vivo*.

Although this class of molecules has been extensively researched in cancer and viral therapies, there has been little work in bacteria due to the proposed endocytic method of entry. Moreover, DNA-binding stapled peptides have not been extensively investigated due the complexities in designing a peptide with gene selectivity. In an attempt to study peptides in bacteria, two stapled peptides based on the RpoN domain of σ^{54} and the FtsZ C-terminus have been synthesized. σ^{54} is a DNA-binding co-factor of RNA polymerase (RNAP) and has been shown to regulate virulence and nitrogen and carbon metabolism. FtsZ is the structural unit of the contractile Z-ring that induces cell division. By designing stapled α-helical peptides to target these untraditional PPIs, we anticipate that these molecules may be used for future antimicrobial pharmacological development that treat multidrug resistant bacteria.

Acknowledgements

I would like to thank my supervisor, Dr. Christopher Boddy, for guiding me throughout my graduate studies. On the first day I entered the lab, I really had no idea if I could make it to the end of grad school. I want to thank you for always being open and receptive to my new ideas and letting me try them out. As farfetched as some were, some turned out alright in the end. I am fortunate that you have assembled the most wonderful team of researchers and to have learned in such a welcoming environment. As I enter the final stage of my graduate career, I have gained much more than I could have possibly imagined being a part of the Boddy lab. I could not have asked for a better supervisor.

Secondly, I would like to thank Dr. Federico Bernal for inviting me to the National Cancer Institute in Bethesda, MD, and his stapled peptide team. I was truly fortunate to have worked with such an inspiring supervisor who is just as receptive to my ideas as Chris was. If anything, my biggest life lesson from you is to fear the Mexican drinks. In particular, I want to thank Amanda Whiting for putting up with my selfish needs as my peptide synthesizer jockey for the stapled peptides, but more importantly, for the guidance throughout the Master's road and for the wonderful talks about science and Canada. I am glad that she has been a part of my research experience; I could not ask for a better post-doc overlord. I want to thank her post-baccalaureate minions, Blaze Pharoah and Sterling Payne, for working on the EMSA and cytotoxicity experiments. And I want to thank Bethanie Lee (Morrison) for her advice in biology and life and welcoming me at the Bernal lab with such warmth and acceptance. To my NIH friends Shutong, Marol, and Samira, I am glad that I ended up rooming at that crazy woman's house since I could meet you all.

Hasitha de Alwis, I cannot believe you have stuck with me since third year, all the way up until graduate studies. Wherever I go next, I know that anytime we meet, it will always be like time never passed between us. I am especially grateful for all your help with the anisotropy and nanoparticle work. It has truly made this project something special. I would also like to thank Tito Scaiano and Emilio Alarcon for allowing Has and I to test our ideas and for the continuous support. Finally, I think I speak for everyone in the common biology labs, but I am glad that Phil Pelletier is there to help with anything at any time. I could not have completed the work with the qPCR and ddPCR without you. As much as I hate to say it, I will miss your teasing. I also want to thank Ron Shah and Amanda Saikaley. It's been a wild ride but I could not have done it with better friends and fellow 2013 grad student minions.

Finally, I would like to thank my lab mates, friends, and parents for supporting me throughout this journey. Thank you for being that escape that I needed to keep my sanity.

I truly feel lucky to have met such inspiring, talented, and accomplished individuals throughout my grad studies and feel humbled every day.

Table of Contents

List of Figures

List of Tables

List of Abbreviations

AAA+	ATPase associated with diverse cellular activities
ANOVA	Analysis of variance
APTES	3-aminopropyltriethoxysilane
AtoD	Acetate CoA-transferase α subunit
ATP	Adenosine triphosphate
ATPase	ATP synthase
AuNP	Gold nanoparticle
Bax	Bcl-2-associated X protein
Bcl-2	B-cell lymphoma 2
bEBP	Bacterial enhancer binding protein
BH3	Bcl-2 homology 3
BID	BH3 interacting-domain death agonist
CD	Circular dichroism
cDNA	Complementary DNA
CLL	Chronic lymphocytic leukemia
Clp	Caseinolytic mitochondrial matrix peptidase chaperonin
CPP	Cell penetrating peptide
Cq	Quantitation cycle
CoA	Coenzyme A
Cy5	Indodicarbocyanine
DAPI	4',6-diamidino-2-phenylindole
DCE	Dichloroethane
DCM	Dichloromethane
ddPCR	Digital droplet PCR
DEPC	Diethylpyrocarbonate
DIPEA	*N*,*N*-Diisopropylethylamine
DMF	Dimethylformamide
DMSO	Dimethyl sulfoxide
DNA	Deoxyribonucleic acid
dsDNA	Double stranded DNA

EDC	1-Ethyl-3-(3-dimethylaminopropyl)carbodiimide
EDTA	Ethylenediaminetetraacetic acid
EMSA	Electrophoretic mobility shift assay
FACS	Fluorescence-activated cell sorting
FITC	Fluorescein isothiocyanate
FLIM	Fluorescence lifetime imaging microscopy
FM4-64	*N*-(3-triethylammoniumpropyl)-4- (p-diethylaminophenyl-hexatrienyl) pyridinium dibromide
Fmoc	Fluorenylmethyloxycarbonyl chloride
FRET	Förster resonance energy transfer
FtsA	Filamentous temperature sensitive A
FtsZ	Filamentous temperature sensitive Z
gDNA	Genomic DNA
GlnA	Adenylyl glutamine synthetase
GTP	Guanosine triphosphate
GTPase	GTP synthase
HCTU	2-(6-Chloro-1H-benzotriazole-1-yl)-1,1,3,3-tetramethylaminium hexafluorophosphate
hDM2	Human double minute 2 homolog
HPLC/MS	High-performance liquid chromatography / Mass spectrometry
HSQC	Heteronuclear single-quantum correlation
HTH	Helix-turn-helix
IHF	Integration host factor
IR	Infrared
ISDA	Infectious Disease Society of America
ITC	Isothermal titration calorimetry
LB	Lysogeny broth (Luria-Bertani medium)
MAML	Mastermind-like
MHB	Müller-Hinton Broth
MIC	Minimum inhibitory concentration
MinC	Minicells
MES	2-(*N*-morpholino)ethanesulfonic acid
M-MLV	Moloney Murine Leukemia Virus

mRNA	Messenger RNA
MST	Microscale thermophoresis
MTBE	Methyl *tert*-butyl ether
MTT	3-(4,5-dimethylthiazol-2-yl)-2,5-diphenyltetrazolium bromide
NDM-1	New Delhi metallo-β-lactamase 1
NHS	*N*-Hydroxysulfosuccinimide
NICD	Notch1 intracellular domain
NMP	*N*-methyl-2-pyrrolidone
NMR	Nuclear magnetic resonance
NTP	Nucleoside triphosphate
NtrC	Nitrogen regulation protein
OD	Optical density
p53	Tumour protein p53
PBS	Phosphate buffer saline
PCR	Polymerase chain reaction
PDI	Protein-DNA interaction
PMF	Proton motive force
PPI	Protein-protein interaction
Psp	Phage shock protein
qPCR	Quantitative PCR
QseC	Quorum sensing *E. coli* regulator C
RFU	Relative fluorescence unit
RLU	Relative luminescence unit
RNA	Ribonucleic acid
RNAP	RNA polymerase
RpoN	RNA polymerase, nitrogen-limitation N
SAH	Stapled α-helix
SPPS	Solid-phase peptide synthesis
TAE	Tris-acetate-EDTA
TBE	Tris-borate-EDTA
TE	Tris-EDTA
TFA	Trifluoroacetic acid

TIPS	Triisopropylsilane
UV	Ultraviolet
ZipA	Z-interacting protein A

Chapter 1

Biological Applications of Stapled α-helical Peptides

1.1 Introduction

Throughout modern drug history, man has engaged in an evolutionary arms race with the multidrug resistance development of various microbes. The rate at which pathogens acquire multidrug resistance continues to outmatch antibiotic development and leaves few options to treat bacterial infections. With the emergence of powerful new resistance genes such as the New Delhi Metallo-β-lactamases,[1,2] humanity's most robust antibiotics are being rapidly neutralized. Over the past five years, these genes have developed a number of variants[3] and new reports of NDM-1 expressing Gram negative bacteria are appearing globally.[4–6] Accordingly, in 2010, the Infectious Diseases Society of America (ISDA) announced a global commitment to developing new antibacterial drugs by 2020.[7] With the ever increasing incidence of multidrug resistant infections, there is a growing and urgent need to design molecules capable of targeting new bacteria-specific targets.

Small-molecule based drug discovery has been extremely effective in developing therapies against many diseases. However, this approach relies on small molecules binding to a discrete, typically well-defined pocket.[8] Many superbug strains have gained resistance to nearly all small molecule antibiotics through selective evolutionary pressures that modify the binding pocket to inhibit drug binding. Complex natural products like polymyxins, a class of peptide-based antibiotics, are becoming our last line of defence against bacteria but possess more side effects than typical antibiotics.[1] As a result, current antibiotic research is highly focused in large complex natural products like non-ribosomal peptides and polyketides to circumvent small molecule limitations.[9,10]

These approaches are not practical for inhibiting extensive protein-protein interfaces (PPIs) common in biological processes due to their large, shallow, and hydrophobic binding

intefaces.[11,12] Discovering cell-permeable selective inhibitors of PPIs is one of the greatest challenges facing chemical biology today.[13] Consequently, biologics, a complex class of drugs ranging from proteins, sugars, or nucleic acids to cells and tissues, are gaining ground as a new class of therapeutics that bypass small-molecule limitations. Peptidomimetics are becoming an appealing candidate to evaluate interactions *in vivo* due to their specificity.[14–16] However, some classes, such as cell penetrating peptides (CPPs), are highly reliant on charge and permeate a wide variety of cells non-specifically.[17] While these molecules are a highly promising new group of drug candidates, the specificity and clinical applicability of CPPs are constantly under scrutiny and need further refinement.[18,19]

Many efforts have been directed towards the refinement of therapeutic biologics. Most peptide-based drugs are modeled on domains that adopt a secondary structure. The α-helix is a major structural motif of proteins and is a primary component of numerous protein-target interfaces in biological systems. In principle, helical peptides can be used to selectively interrupt protein-target interactions and control physiological processes. Early approaches to covalent helix stabilization involve the addition of polar or labile cross-linking residues to peptide sequences.[13,20–23] Unfortunately, this leaves peptides with poor pharmacological properties including reduced ability to cross biologically relevant membranes and significant metabolic instability *in vivo*. The ratio of peptides retaining a low energy secondary structure compared to an unstructured variant is small and activity decreases.

Hydrocarbon stapling is a chemical strategy that circumvents these problems for short peptide sequences.[24,25] The accepted method is to use α,α-disubstituted non-natural amino acids with olefin tethers to generate a hydrocarbon cycle or "staple" through ruthenium catalysis.[24] These substituted amino acids are used to increase the proteolytic stability of the

peptides to render them unrecognizable to native proteolysis mechanisms and restrict the conformational freedom of the peptide backbone. Thus, the synthesized cycles are "stapled peptides" that adopt α-helical secondary structure as their lowest energy forms. Due to this enforcement of secondary structure,[25] many pharmacological properties are improved, including protease stability,[26] and increased activity.[24–27]

Stapled peptides are an emerging class of peptide therapeutics developed within the last 15 years to successfully target both intracellular and extracellular PPIs. In particular, Aileron therapeutics recently completed the first stapled peptides clinical trial in targeting cancer-related pathways. Stapled peptides are now regarded as one of the top next-generation classes of biologics for treatment therapeutics. This chapter will review the current literature for stapled peptides and their place as research tools and a novel class of therapeutics.

1.2 Methods of stapling peptides

Although the most commercially available method of synthesizing stapled peptides is hydrocarbon ruthenium catalysis[28] based on the field's pioneering work,[24] a variety of cyclization methods have been reported. Factors such as the position, length, and flexibility of the crosslinking amino acids have been well studied. Many early methods include the use of non-covalent interactions like salt bridge, metal chelation, crown ether, and π stacking interactions or covalent modification at *i*, *i*+4, *i*+7, and *i*+11 positions with disulfide and lactam-based bridges.[29–31] Newer methods making use of ruthenium catalysis have been explored such as hydrogen bonding surrogates.[32] Variation of the amino acids themselves such as with β-peptides has been shown to increase the proteolytic stability of peptide therapeutics.[33]

New techniques in chemical biology have been applied to stapled peptides to further expand the methods of chemical synthesis. Among the new techniques is the use of engineered cysteines to install monoaryl and biaryl staples to stabilize *i*, *i*+4 and *i*, *i*+7 positions respectively.[34,35] By virtue of this modification of the staple, new avenues have been explored to control α-helix formation *in situ*. Azobenzene crosslinkers have been introduced, again through cysteine engineering, to confer photoswitchable α-helices based on cis-trans isomerization upon irradiation.[36] Various types of linkers such as cycloaddition click chemistry,[37] and oxime chemistry[38] have been applied to the staple to allow additional nucleation[39] and functionalization[40] for further modification and bioorthogonal manipulation.

1.3 Origins of stapled peptides

The stapling concept first arose in 2004 in the hopes of developing a method to combat chemotherapy-resistant cancer cells. Bcl-2 proteins are a prime target as a cancer therapeutic as the protein family is an essential control point in apoptosis inhibition and B cell proliferation in chronic lymphocytic leukemia.[24,41–44] Overexpression of Bcl-2 has been suggested to head to defects of apoptosis in chronic lymphocytic leukemia (CLL) and other types of lymphomas.[45,46] In general, an increase in malignant B cells will exhibit clonal ignorance, an inability to bind to their original antigen, due to ageing.[47] When returning to the bone marrow, the excess B cells interfere with the production of red blood cells, thus reducing the availability of oxygen for a patient.

Bcl-2 was the first proto-oncogene with anti-apoptotic function discovered and has since been thoroughly researched and tested in various bloodborne cancers.[45,46] In cancer cells associated with high levels of Bcl-2, BH3 domains can saturate the anti-apoptotic

protein to allow normal apoptosis.[48] BID, a pro-apoptotic member of the Bcl-2 protein family, interacts with both Bcl-2 and Bax, another pro-apoptotic Bcl-2 family protein, with its α-helical BH3 domain. Through the BID-Bax interaction, activated Bax localizes to the outer mitochondrial membrane to form pores that release cytochrome c and other pro-apoptotic factors.[48] This ultimately leads to caspase-induced apoptosis. However, Bcl-2 sequesters BID to inhibit Bax dimerization and prevent apoptosis. Overexpressed Bcl-2 will bind to BID and inhibit Bax activation, thus inhibiting cell death in lymphoma cells. In principle, the α-helix of BID's BH3 domain should compete with Bcl-2 for binding to BID, enabling the BID-Bax activation of apoptosis (**Fig.1.1**).[24]

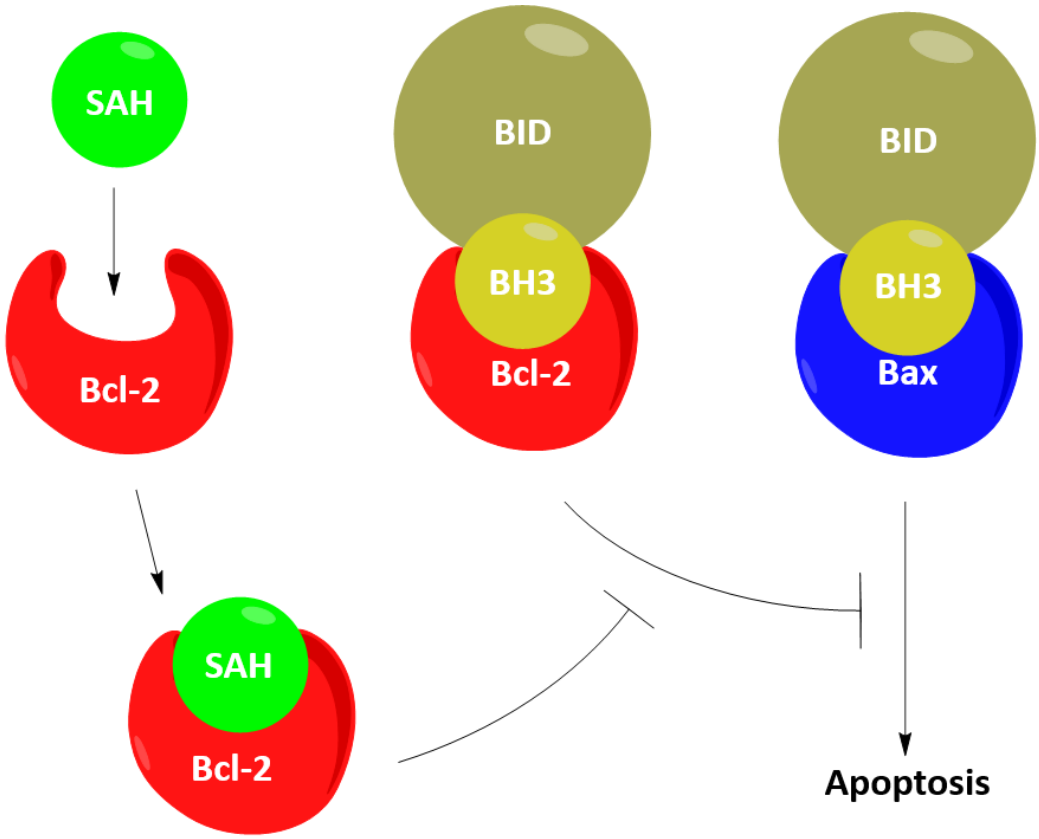

Figure 1.1. Conceptual model of BH3 stapled α-helical peptide. Stapled α-helical (SAH) peptide treatment of the BH3 domain inhibits anti-apoptosis Bcl-2 and reactivates pro-apoptotic Bax.

Walensky *et al.* developed an amphipathic α-helical BH3 segment of BID. A set of hydrocarbon-stapled peptides, $SAHB_A$ to $SAHB_D$, were synthesized through solid-phase peptide synthesis and purified through HPLC. The placement of the *i*, *i*+4 staple was adjusted in each peptide to provide a variety of candidates for biological activity. To demonstrate binding to the target, two-dimensional NMR ^{15}N-^{1}H HSQC of ^{15}N-labeled Bcl-2 and BH3 stapled peptide displayed structural changes similar to the native protein. Furthermore, a fluorescence polarization binding assay showed a six-fold enhancement in binding affinity compared to the native peptide (from 269 nM to 38.8 nM). All peptides were assessed for α-helicity through circular dichroism spectroscopy and each possessed helical content ranging from 35 to 87%.[24] In addition to enforcing the helical structure, the hydrocarbon staple conferred a high degree of protease-resistance and serum stability *in vitro* and *in vivo*. Overall, $SAHB_A$ proved to be the best candidate as it possessed the highest α-helical content and lowest K_D.

In vitro activity of $SAHB_A$ was assessed. Membrane penetration properties of all synthesized peptides were assessed through both FACS and confocal microscopy. The peptides entered Jurkat leukemia cells through an energy-dependent endocytosis mechanism for cellular import in a time-dependent manner. As predicted, $SAHB_A$ showed mitochondrial membrane colocalization in cells[24]. Mouse liver mitochondria were incubated with $SAHB_A$ and Cytochrome c release was observed in a dose-dependent manner consistent with pro-apoptosis activity[24]. Furthermore $SAHB_A$ was able to initiate annexin V-mediated apoptosis, even in cell lines that were overexpressing high levels of Bcl-2.[24] *In vivo* activity of immunodeficient mice with human leukemia cells expressed luciferase within localized

tumours of the spleen and liver. $SAHB_A$ (10 mg/kg) treatments proved to be effective at reducing tumour growth in leukemic mice.

This BH3 peptide was the first attempt at examining stapled peptides in mouse models. The short staple component of this class of molecules confers rigid secondary structure to the peptides enabling them to bind to large shallow surfaces and inhibit complex protein-protein interactions. The key observations include the need for ATP-mediated uptake to reach intracellular targets and the high affinity and specificity of binding to the target proteins. Since this initial development of the hydrocarbon crosslinker, many more therapeutic stapled peptides have been investigated, particularly in relation to the p53 apoptosis pathway.

1.4 Cancer stapled peptides therapeutics

1.4.1 p53 stapled peptides in caspase-mediated apoptosis

In 2007, Bernal *et al*. published a new stapled peptide that imitates the apoptotic transcription factor p53.[49] This peptide is the first example of a stapled peptide that kills cancer cells through a transcriptional pathway. E3 ubiquitin ligase hDM2 controls p53 levels by ubiquitination, thus decreasing its half-life and transcriptional activation capabilities.[50,51] Since p53 triggers programmed cell death, its mutation or hDM2 overexpression is commonly associated with malignant cancers.[52] A peptide designed to block overexpressed hDM2 will reactivate apoptotic pathways related to p53. The goal of this peptide is to block the E3 ubiquitin ligase hDM2 to prevent further degradation of native p53.[49] This peptide was modeled against the hDM2-p53 interface to restore p53 transcriptional activity and induce apoptosis.

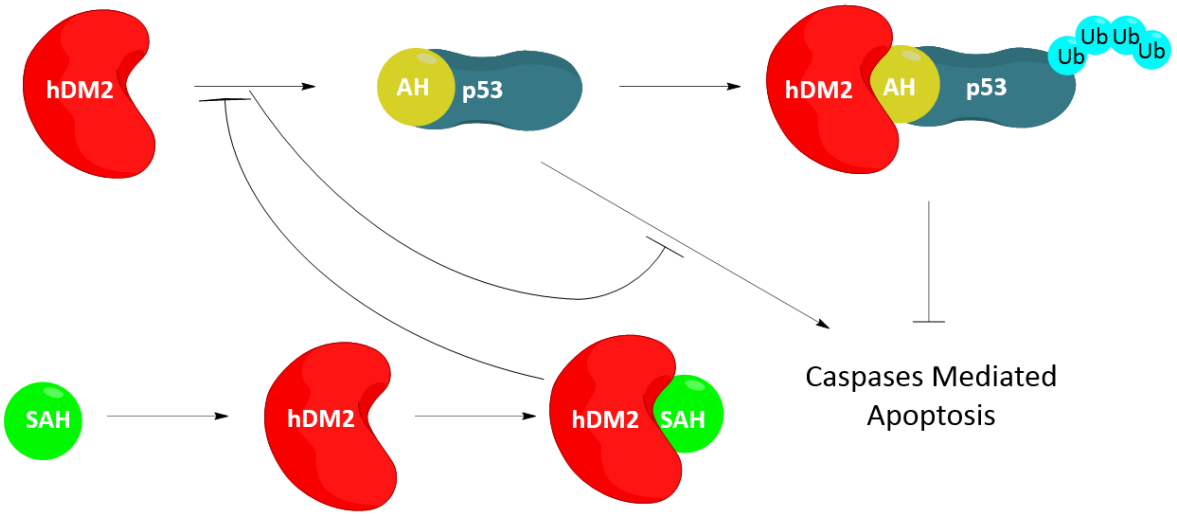

Figure 1.2. Conceptual model of p53 stapled α-helical peptide. Stapled α-helical (SAH) peptide treatment inhibits anti-apoptosis hDM2 and reactivate pro-apoptotic p53 functions. AH means α-helix, Ub for ubiquitination.

Compared to Walensky's *i*, *i*+4 staple, this peptide used an *i*, *i*+7 staple to model p53's binding interface with hDM2. Instead of the cyclization occurring at one helical turn away, the peptide was immobilized two helices away. Though *in vitro* studies show nanomolar binding constants with the native protein,[49] there was little cell penetration of the peptide in mammalian cells. The charge was investigated to examine the effects of charge on cell penetration. Aspartic and glutamic acid were replaced with asparagine and glutamine to decrease the negative charge of the molecule like with other types of cell-penetrating peptides.[17,53] With the increased positive charge, the binding was shown to increase. Interestingly, only one peptide specifically engineered with point mutations in both nuclear export and ubiquitylation sites, led to cytotoxicity.[49] Furthermore the compound showed dose-dependent inhibition of SJSA-1 cell viability and activation of caspase-3 activity, a hallmark of apoptosis. In summary, this study introduced a longer staple (*i*, *i*+7) and amino acid substitution to prevent inhibit degradation while promoting cell penetration.

1.4.2 MAML1 in Notch signalling

Transcriptional factors have long been an elusive target in eukaryotic systems. This is due to the sheer number of DNA permutations available to target, the lack of surface binding pockets suitable for high-affinity small molecules to bind to, and multiple membranous barriers to extracellular molecules.[54] While transcription factors typically lack hydrophobic pockets, they do engage in extensive PPIs. As such they are promising targets for binding by stapled peptides. In 2009, *Moellering et al.* sought to design a peptide targeting transcription factors in the Notch1 pathway.

Notch receptors are single-pass transmembrane proteins that conduct signalling between cells.[55] The downregulated activity of Notch signalling has been linked to growth suppression in T-cell leukemias.[56] Once a neighbouring cell's ligand is bound to the extracellular domain of Notch1, a sequence of proteolytic events leads to the release of Notch1's intracellular domain (NICD).[57] As NICD is translocated to the nucleus, it binds to the DNA-binding protein CSL[55] and together recruit MAML,[58] a co-activator, to create a ternary nuclear complex. In particular, MAML is bound to the NICD-CSL groove through an α-helix and it functions as a critical regulatory point in differentiation, proliferation, and cell death.[59] As with the BH3 and p53 peptides, Notch1 possessed a highly influential α-helix where many abnormal mutations are causally linked with cancer.[56,60,61]

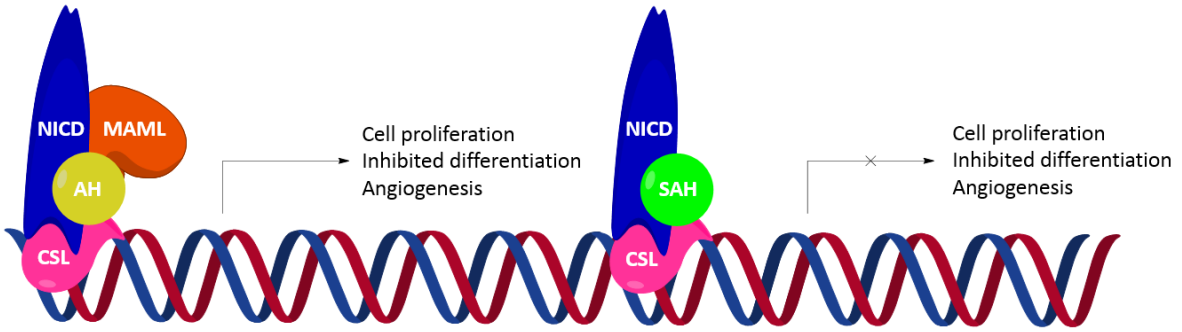

Figure 1.3. Conceptual model of MAML N-terminus stapled α-helical peptide. Stapled α-helical (SAH) peptide treatment inhibits cancer functions. AH represents the α-helix domain, Ub for ubiquitination.

Peptides imitating the N-terminus of MAML are thus expected to disrupt heterotrimer formation and thus transcription. As the MAML peptide is a 60-mer α-helix, a panel of analogs dividing this region was assessed. As predicted, the N-terminus was found to most effectively block Notch1 signalling. Without the C-terminus, RNAP cannot be recruited and therefore no expression will occur. As discovered by *Moellering*, the peptides prevent cell proliferation in T-cell acute lymphoblastic leukemia. In previous applications, stapled peptides have acted as rescue agents to allow the natural pathways to function (i.e. BH3 and p53). This peptide provides the first instance in which a stapled peptide exhibits direct antagonism of an "undruggable" transcription factor within the nuclei of cells.

From this discovery, many research programs have devoted their efforts into cell surface receptor activation or inhibition in estrogen receptors,[62] cholesterol efflux,[63] insulin,[64] and neuronal receptors.[65] Other studies in signalling pathway targets include the GTPase pathway[66,67] and kinase activity.[68] Non-human eukaryotes such as the *Plasmodium* genus have been investigated to develop peptides inhibiting new targets for drug development purposes.[69] Among these eukaryotic targets, only one protein-DNA interaction in mammalian cells has been observed but lacks extensive supporting research in phenotypic

studies.[70] Much of the work derived from cancer studies by both the Verdine and Walensky labs have spurred a renewed interest in therapeutic biologics.

1.5 Viral stapled peptides therapeutics

Stapled peptides have also been investigated as inhibitors of viral infection in mammalian cells. While still in its infancy, the main strategy for inhibiting viral infection is to target the viral fusion apparatus. The first attempt at viral stapled peptides was modeled based on enfuvirtide, a fusion inhibitor blocking HIV-1 in humans.[71] Enfuvirtide was designed to mimic the heptad repeat 2 (HR2) oligomerization domain of the gp41 transmembrane glycoprotein. This region plays a key role in promoting fusion of the viral and cell membranes.[72] Mimics of this α-helix exhibit dominant negative activity in preventing the gp41 six helical bundle assembly of the membrane fusion apparatus.[72]

As the peptide drug is 36 amino acids long, one staple between 4 or 7 amino acids will likely not confer α-helical character to all 36 amino acids. In response to this, yet another tool in the stapled peptide toolbox was developed. This peptide is the first instance of a doubly stapled structure on a lengthy peptide therapeutic. Two short *i*, *i*+4 staples were introduced in hopes of stabilizing the whole molecule. With the introduction of a second staple, its half-life when treated with chymotrypsin increased 3-4 fold compared to the singly stapled version and 24 fold compared to the unstapled drug. Further studies on oral absorption of the doubly stapled peptides demonstrated a high resistance to low pH and peptide; plasma samples detected trace amounts of the doubly stapled peptide.

Though this does provide strong evidence for interest in viral therapeutics, current efforts towards viral therapeutics have been focused on improving known peptide-based

inhibitors of α-helical interactions. One aspect under investigation is the targeting of the viral envelope and membrane fusion apparatus in Hepatitis C[73] and Respiratory Syncytial Virus[74] with the *i*, *i*+7 and doubly stapled techniques respectively. Other strategies involve using stapled peptide designed to inhibit genes specific to impair capsid formation,[75] and viral enzymes responsible for host genome integration.[76]

1.6 Efforts towards bacteria stapled peptide applications

One other notable aspect of the development of stapled peptide therapeutics is that, to date, they have been limited to eukaryotic systems and viruses. One group has recently published a stapled peptide functioning in membrane efflux pump disruption in bacteria.[77] However, this group has only demonstrated a method to act synergistically with other antibiotics. The vast majority of current stapled peptide research in bacteria, much like that of viruses, focuses on improving reported antimicrobial peptides (AMPs).[78–81] Although all these studies demonstrate excellent applications of stapled peptides as a tool to increase the pharmacokinetics of peptide therapies, these forms of research lack the inspiration to pursue the original intention of the field: to affect previously inaccessible targets for therapeutics.

No significant research is investigating new targets in bacterial systems with stapled peptides. As bacteria possess a peptidoglycan cell wall to retain structural integrity, lipopolysaccharides to limit hydrophobic molecule entry, and a phospholipid membrane, the typical mechanism of uptake for stapled peptides is not possible and thus their ability to penetrate the cell is unknown. To design molecules affecting bacterial intracellular targets, many barriers must be surmounted prior to targeting a specific interaction.

1.7 Conclusions and Prospects

In the past decade, the stapled peptide field has seen massive strides in both the development of the chemical toolbox and their potential to target a variety of pathways. Many proteins in cancer biology and viral microbiology have been successful targeted by stapled peptides. With the growing field, new techniques in chemical biology are being applied to these fields to further tune the potential of stapled peptide research. However, there remain plenty of unmapped territories in the realm of undruggable PPI targets. Many of the current techniques have been used to enhance existing bioactive peptides but few new peptide sequences have been reported. The development of compounds targeting specific DNA sequences presents a major opportunity to further expand stapled peptide methodology as protein-DNA interactions (PDIs) fundamentally contribute to all cellular processes.

1.8 References

1. Moellering, R. C. NDM-1 - A Cause for Worldwide Concern. *N. Engl. J. Med.* **363,** 2377–2379 (2010).

2. Yong, D. *et al.* Characterization of a new metallo-B-lactamase gene, bla NDM-1, and a novel erythromycin esterase gene carried on a unique genetic structure in Klebsiella pneumoniae sequence type 14 from India. *Antimicrob. Agents Chemother.* **53,** 5046–5054 (2009).

3. Rahman, M. *et al.* Prevalence and molecular characterisation of New Delhi metallo-β- lactamases NDM-1, NDM-5, NDM-6 and NDM-7 in multidrug-resistant Enterobacteriaceae from India. *Int. J. Antimicrob. Agents* **44,** 30–37 (2014).

4. Voulgari, E. *et al.* The Balkan region: NDM-1-producing Klebsiella pneumoniae ST11 clonal strain causing outbreaks in Greece. *J. Antimicrob. Chemother.* **69,** 2091–2097 (2014).

5. Qin, S. *et al.* High incidence and endemic spread of NDM-1 positive Enterobacteriaceae in Henan province, China. *Antimicrob. Agents Chemother.* **58,** 4275–4282 (2014).

6. Rozales, F. P. *et al.* Emergence of NDM-1-producing Enterobacteriaceae in Porto Alegre, Brazil. *Int. J. Infect. Dis.* **25,** 79–81 (2014).

7. IDSA. The 10 x ’20 Initiative: pursuing a global commitment to develop 10 new antibacterial drugs by 2020. *Clin. Infect. Dis.* **50,** 1081–1083 (2010).

8. Babine, R. E. & Bender, S. L. Molecular Recognition of Protein − Ligand Complexes : Applications to Drug Design. *Chem. Rev.* **97,** 1359–1472 (1997).

9. Genilloud, O. The re-emerging role of microbial natural products in antibiotic discovery. *Antonie van Leeuwenhoek, Int. J. Gen. Mol. Microbiol.* **106,** 173–188 (2014).

10. Lewis, K. Platforms for antibiotic discovery. *Nat. Rev. Drug Discov.* **12,** 371–87 (2013).

11. Gohlke, H. & Klebe, G. Approaches to the description and prediction of the binding affinity of small-molecule ligands to macromolecular receptors. *Angew. Chemie - Int. Ed.* **41,** 2644–2676 (2002).

12. Keppler, A. *et al.* A general method for the covalent labeling of fusion proteins with small molecules in vivo. *Nat. Biotechnol.* **21,** 86–89 (2003).

13. Azzarito, V. *et al.* Inhibition of α-helix-mediated protein-protein interactions using designed molecules. *Nat. Chem.* **5,** 161–73 (2013).

14. Brouwer, C. P. J. M. *et al.* Discovery and development of a synthetic peptide derived from lactoferrin for clinical use. *Peptides* **32,** 1953–1963 (2011).

15. Butler, M. S. *et al.* Glycopeptide antibiotics: Back to the future. *J. Antibiot. (Tokyo).* **67,** 631–644 (2014).

16. Di Luca, M. *et al.* Treatment of microbial biofilms in the post-antibiotic era: prophylactic and therapeutic use of antimicrobial peptides and their design by bioinformatics tools. *Pathog. Dis.* **70,** 257–70 (2014).

17. Rodriguez Plaza, J. G. *et al.* Cell penetrating peptides and cationic antibacterial peptides: Two sides of the same coin. *J. Biol. Chem.* **289,** 14448–14457 (2014).

18. Foerg, C. & Merkle, H. P. On The Biomedical Promise of Cell Penetrating Peptides: Limits Versus Prospects. *J. Pharm. Sci.* **97,** 144–162 (2008).

19. Heitz, F. *et al.* Twenty years of cell-penetrating peptides : from molecular mechanisms to therapeutics. *Br. J. Pharmacol.* **157,** 195–206 (2009).

20. Wu, C. W. *et al.* Structural and spectroscopic studies of peptoid oligomers with alpha-chiral aliphatic side chains. *J. Am. Chem. Soc.* **125,** 13525–13530 (2003).

21. Phelan, J. C. *et al.* A general method for contraining short peptides to an α-helical conformation. *J. Am. Chem. Soc.* **119,** 455–460 (1997).

22. Milroy, L. *et al.* Modulators of Protein − Protein Interactions. *Chem. Rev.* **114,** 4695–4748 (2014).

23. Henchey, L. K. *et al.* Contemporary strategies for the stabilization of peptides in the α-helical conformation. *Curr. Opin. Chem. Biol.* **12,** 692–697 (2008).

24. Walensky, L. D. *et al.* Activation of apoptosis in vivo by a hydrocarbon-stapled BH3 helix. *Science* **305,** 1466–1470 (2004).

25. Schafmeister, C. E. *et al.* An All-Hydrocarbon Cross-Linking System for Enhancing the Helicity and Metabolic Stability of Peptides. *J. Am. Chem. Soc.* **122,** 5891–5892 (2000).

26. Bird, G. H. *et al.* Hydrocarbon double-stapling remedies the proteolytic instability of a lengthy peptide therapeutic. *Proc. Natl. Acad. Sci. U. S. A.* **107,** 14093–14098 (2010).

27. Sun, T. L. *et al.* Membrane permeability of hydrocarbon-cross-linked peptides. *Biophys. J.* **104,** 1923–1932 (2013).

28. Blackwell, H. E. & Grubbs, R. H. Highly efficient synthesis of covalently cross-linked peptide helices by ring-closing metathesis. *Angew. Chemie - Int. Ed.* **37,** 3281–3284 (1998).

29. Andrews, M. J. I. & Tabor, A. B. Forming Stable Helical Peptides Using Natural and Artificial Amino Acids. *Tetrahedron* **55,** 11711–11743 (1999).

30. Geistlinger, T. R. & Guy, R. K. Novel selective inhibitors of the interaction of individual nuclear hormone receptors with a mutually shared steroid receptor coactivator 2. *J. Am. Chem. Soc.* **125,** 6852–6853 (2003).

31. Sia, S. K. *et al.* Short constrained peptides that inhibit HIV-1 entry. *Proc. Natl. Acad. Sci. U. S. A.* **99,** 14664–14669 (2002).

32. Chapman, R. N. *et al.* A Highly Stable Short α-Helix Constrained by a Main Chain Hydrogen Bond Surrogate. *New York* **126,** 12252–12253 (2004).

33. Cheng, R. P. *et al.* β-Peptides : From Structure to Function. *Chem. Rev.* **101,** 3219–3232 (2001).

34. Muppidi, A. *et al.* Achieving cell penetration with distance-matching cysteine cross-linkers: a facile route to cell-permeable peptide dual inhibitors of Mdm2/Mdmx. *Chem. Commun.* **47,** 9396–9398 (2011).

35. Muppidi, A. *et al.* Rational Design of Proteolytically Stable , Cell-Permeable Peptide - Based Selective Mcl - 1 Inhibitors. *J. Am. Chem. Soc.* **134,** 14734–14737 (2012).

36. Kumita, J. R. *et al.* Photo-control of helix content in a short peptide. *Proc. Natl. Acad. Sci. U. S. A.* **97,** 3803–3808 (2000).

37. Kawamoto, S. A. *et al.* Design of triazole-stapled BCL9 α-helical peptides to target the β-catenin/B-cell CLL/lymphoma 9 (BCL9) protein-protein interaction. *J. Med. Chem.* **55,** 1137–1146 (2012).

38. Haney, C. M. *et al.* Promoting peptide α-helix formation with dynamic covalent oxime side-chain cross-links. *Chem. Commun.* **47,** 10915 (2011).

39. Torres, O. *et al.* Peptide tertiary structure nucleation by side-chain crosslinking with metal complexation and double 'Click' cycloaddition. *ChemBioChem* **9,** 1701–1705 (2008).

40. Lau, Y. H. *et al.* Functionalised staple linkages for modulating the cellular activity of stapled peptides. *Chem. Sci.* **5,** 1804 (2014).

41. Hanada, M. *et al.* bcl-2 gene hypomethylation and high-level expression in B-cell chronic lymphocytic leukemia. *Blood* **82,** 1820–1828 (1993).

42. Danial, N. N. & Korsmeyer, S. J. Cell Death : Critical Control Points Review. *Cell* **116,** 205–219 (2004).

43. Vaux, D. L. *et al.* Bcl-2 gene promotes haemopoietic cell survival and cooperates with c-myc to immortalize pre-B cells.pdf. *Nature* **335,** 440–442 (1988).

44. McDonnell, T. J. *et al.* bcl-2-immunoglobulin transgenic mice demonstrate extended B cell survival and follicular lymphoproliferation. *Cell* **57,** 79–88 (1989).

45. Tsujimoto, Y. *et al.* Involvement of the bcl-2 Gene in Human Follicular Lymphoma. *Science* **228,** 1440–1443 (1985).

46. Reed, J. C. Bcl-2 – family proteins and hematologic malignancies : history and future prospects. *Blood* **111,** 3322–3330 (2008).

47. Chiorazzi, N. *et al.* Chronic Lymphocytic Leukemia. *N. Engl. J. Med.* **352,** 804–815 (2005).

48. Gross, A. *et al.* BCL-2 family members and the mitochondria in apoptosis BCL-2 family members and the mitochondria in apoptosis. *Genes Dev.* **13,** 1899–1911 (1999).

49. Bernal, F. *et al.* Reactivation of the p53 tumor suppressor pathway by a stapled p53 peptide. *J. Am. Chem. Soc.* **129,** 2456–2457 (2007).

50. Honda, R. *et al.* Oncoprotein MDM2 is a ubiquitin ligase E3 for tumor suppressor p53. *FEBS Lett.* **420,** 25–27 (1997).

51. Jain, A. K. & Barton, M. C. Making sense of ubiquitin ligases that regulate p53. *Cancer Biol. Ther.* **10,** 665–672 (2010).

52. Polsky, D. *et al.* HDM2 Protein Overexpression, but not Gene Amplification, is Related to Tumorigenesis of Cutaneous Melanoma. *Cancer Res.* **63,** 7642–7646 (2001).

53. Richard, J. P. *et al.* Cell-penetrating peptides: A reevaluation of the mechanism of cellular uptake. *J. Biol. Chem.* **278,** 585–590 (2003).

54. Verdine, G. L. & Walensky, L. D. The challenge of drugging undruggable targets in cancer: Lessons learned from targeting BCL-2 family members. *Clin. Cancer Res.* **13,** 7264–7270 (2007).

55. Artavanis-Tsakonas, S. *et al.* Notch Signaling: Cell Fate Control and Signal Integration in Development. *Science* **284,** 770–776 (1999).

56. Weng, A. P. *et al.* Growth Suppression of Pre-T Acute Lymphoblastic Leukemia Cells by Inhibition of Notch Signaling Growth Suppression of Pre-T Acute Lymphoblastic Leukemia Cells by Inhibition of Notch Signaling. *Mol. Cell. Biol.* **23,** 655–664 (2003).

57. De Strooper, B. *et al.* A presenilin-1-dependent gamma-secretase-like protease mediates release of Notch intracellular domain. *Nature* **398,** 518–522 (1999).

58. Nam, Y. *et al.* Structural basis for cooperativity in recruitment of MAML coactivators to Notch transcription complexes. *Cell* **124,** 973–983 (2006).

59. Kopan, R. & Ilagan, M. X. G. The Canonical Notch Signaling Pathway: Unfolding the Activation Mechanism. *Cell* **137,** 216–233 (2009).

60. Bedogni, B. *et al.* Notch1 is an effector of Akt and hypoxia in melanoma development. *J. Clin. Invest.* **118,** 3660–3670 (2008).

61. Garg, V. *et al.* Mutations in NOTCH1 cause aortic valve disease. *Nature* **437,** 270–274 (2005).

62. Phillips, C. *et al.* Design and structure of stapled peptides binding to estrogen receptors. *J. Am. Chem. Soc.* **133,** 9696–9699 (2011).

63. Sviridov, D. O. *et al.* Helix stabilization of amphipathic peptides by hydrocarbon stapling increases cholesterol efflux by the ABCA1 transporter. *Biochem. Biophys. Res. Commun.* **410,** 446–451 (2011).

64. Giordanetto, F. *et al.* Stapled Vasoactive Intestinal Peptide (VIP) Derivatives Improve VPAC2 Agonism and Glucose-Dependent Insulin Secretion. *ACS Med. Chem. Lett.* **4,** 1163–8 (2013).

65. Platt, R. J. *et al.* Stapling mimics noncovalent interactions of γ-carboxyglutamates in conantokins, peptidic antagonists of N-methyl-D-aspartic acid receptors. *J. Biol. Chem.* **287,** 20727–20736 (2012).

66. Patgiri, A. *et al.* An orthosteric inhibitor of the Ras-Sos interaction. *Nat. Chem. Biol.* **7,** 585–587 (2011).

67. Spiegel, J. *et al.* Direct targeting of rab-GTPase-effector interactions. *Angew. Chemie - Int. Ed.* **53,** 2498–2503 (2014).

68. Wang, Y. *et al.* Isoform-selective disruption of AKAP-localized PKA using hydrocarbon stapled peptides. *ACS Chem. Biol.* **9,** 635–642 (2014).

69. Douse, C. H. *et al.* Crystal Structures of Stapled and Hydrogen Bond Surrogate Peptides Targeting a Fully Buried Protein–Helix Interaction. *ACS Chem. Biol.* **9,** 2204–2209 (2014).

70. Iyer, A. *et al.* Stapling monomeric GCN4 peptides allows for DNA binding and enhanced cellular uptake. *Org. Biomol. Chem.* **13,** 3856–3862 (2015).

71. Kilby, J. M. *et al.* Potent suppression of HIV-1 replication in humans by T-20, a peptide inhibitor of gp41-mediated virus entry. *Nat. Med.* **4,** 1302–1307 (1998).

72. Chan, D. C. *et al.* Core structure of gp41 from the HIV envelope glycoprotein. *Cell* **89,** 263–273 (1997).

73. Cui, H.-K. *et al.* Stapled peptide-based membrane fusion inhibitors of hepatitis C virus. *Bioorg. Med. Chem.* **21,** 3547–54 (2013).

74. Bird, G. H. *et al.* Mucosal delivery of a double-stapled RSV peptide prevents nasopulmonary infection. *J. Clin. Invest.* **124,** 2113–2124 (2014).

75. Zhang, H. *et al.* Dual-acting stapled peptides target both HIV-1 entry and assembly. *Retrovirology* **10,** 136 (2013).

76. Long, Y. Q. *et al.* Design of cell-permeable stapled peptides as HIV-1 integrase inhibitors. *J. Med. Chem.* **56,** 5601–5612 (2013).

77. Bellmann-Sickert, K. *et al.* Efflux by small multidrug resistance proteins is inhibited by membrane-interactive helix-stapled peptides. *J. Biol. Chem.* **290,** 1752–1759 (2015).

78. Slootweg, J. C. *et al.* Semi-synthesis of biologically active nisin hybrids composed of the native lanthionine ABC-fragment and a cross-stapled synthetic DE-fragment. *Bioorg. Med. Chem.* **22,** 5345–5353 (2014).

79. Dinh, T. T. T. *et al.* Antimicrobial activity of doubly-stapled alanine/lysine-based peptides. *Bioorg. Med. Chem. Lett.* **25,** 4016–4019 (2015).

80. Chapuis, H. *et al.* Effect of hydrocarbon stapling on the properties of α-helical antimicrobial peptides isolated from the venom of hymenoptera. *Amino Acids* **43,** 2047–2058 (2012).

81. Pham, T. K. *et al.* Truncated and constrained helical analogs of antimicrobial esculentin-2EM. *Bioorganic Med. Chem. Lett.* **23,** 6717–6720 (2013).

Chapter 2

Examination of Atypical Antibiotic Targets

2.1 Introduction

2.1.1 Current issues with antibiotics

Despite humanity's ever expanding knowledge of bacterial cell-division pathways, most new antibiotics are simply functional-group modifications of the current classes. Since 1962, only three new antibiotic classes have been approved for the clinic: oxazolidinones (1962), cyclic lipopeptides (2003), and pleuromutilins (2007).[1] While there is a need for antibiotic discovery, narrow-spectrum antibiotics, targeting specific infections without disturbing the natural flora of humans, should be encouraged to avoid the rapid generation of resistant species. The typically short duration of treatment needed to combat bacterial infections makes these drugs less financially appealing to develop than therapies that treat chronic conditions, thus leading to a decrease in antibiotic development by big pharmaceutical companies. Regardless of the likely higher investment, it is necessary to pursue new therapeutics to continue to compete against bacteria once more.[2]

In addition, attempts to discover new antibiotics using high-throughput screening and rational drug design methods been unsuccessful, in part because of a lack of diversity in libraries and difficulties in cell penetration and antibiotic efflux.[3] The barriers presented by Gram negative bacteria, representing three layers of protection, makes development of new antibiotics toward this class of pathogens even more difficult. Innate resistance mechanisms are hard to predict as resistance can already reside in the bacterial genome or be acquired through mutations and horizontal gene transfer of resistant mutants.[4] Dormant enzymes that can inactivate targets through genetic mutation, posttranslational modification, or hydrolysis pose another problem for the use of small molecules.[4]

The majority of antibiotics target one of four processes: protein synthesis, nucleic acid synthesis, cell-wall synthesis, or folate synthesis. Antibiotics are designed to target processes unique to bacteria to minimize toxicity to eukaryotic cells. Bacterial cytokinesis has not been successfully targeted by a clinically approved antimicrobial, thus representing a large field of untapped essential interactions. Identification of druggable targets in bacterial cell division has proved challenging. In particular many potential targets lack the small hydrophobic binding pockets targeted by traditional small molecule drug development. However there are a number of exciting new potential targets in cell division that rely on extensive protein-protein interactions (PPIs).[1] This chapter will discuss the efforts towards inhibitors of FtsZ, the structural unit required to initiate bacterial cytokinesis.

Furthermore, efforts towards the inhibition of bacterial pathogenesis are beginning to emerge as a support class of antimicrobial compounds. Small molecules have been identified to target bacterial adhesion[5] and quorum-sensing.[6] There is a growing interest in the benefits of inhibiting bacteria infectivity as a means to circumvent the issues with antibiotic resistance development. This chapter also will discuss the application of σ^{54}, a transcriptional regulator, as a method of reducing pathogenicity in bacteria.

2.1.2 Virulence factors are promising targets

Pathogenic bacteria undergo a relatively similar course of infection and colonization. Bacteria must overcome pH, temperature, defence systems, and existing flora at infection points to colonize and successfully infect the host. Bacteria use a number of strategies to help them perform this task. Over the last 7 years, development of drugs that target these virulence factors has gained ground and antivirulence compounds are emerging as a new therapeutic class.[7]

Antivirulence compounds seek to inhibit bacterial host persistence mechanisms like toxin secretion, adhesion, biofilm formation, quorum-sensing, and immune invasion.[8] The advantage to these types of molecules is that they do not exert a life or death selection pressure since they prevent colonization rather than killing the organism. This reduced selection pressure is predicted to decrease the rate at which resistance to antivirulence drugs develops. QseC, an adrenergic receptor linked to activation of quorum-sensing during infection, was among the first antivirulence targets for which small molecule drugs were synthesized.[9] Since this discovery, small molecule inhibitors have been developed for colonization toxins,[10] other quorum-sensing pathways[11,12] and adhesins.[13]

However, some difficulties with the antivirulence approach are due to the heterogenic nature of infection. Natural biofilms are comprised of various populations and species of bacteria. Consequently, antivirulence agents affect biofilms to varying degrees as the unique bacterial makeup of each infection significantly varies between hosts as their natural flora. Furthermore, resistance can still be developed against small molecules.[14] By targeting genes that affect the transcription of these pathogenic characteristics, molecules targeting PDIs related to these functions would confer new life to pathogenesis targeting.

2.2 σ^{54} as a target for stapled peptide antivirulence therapeutics

2.2.1 σ^{54} Transcriptional Pathway

Bacterial transcription requires sequence-specific recognition to successfully localize the transcriptional machinery to a gene of interest. RNA polymerase (RNAP) is a multisubunit enzyme consisting of a core enzyme with four subunits: α, α, β, and β', and an additional σ unit that is exchangeable.[15] To direct protein expression, multiple σ factors are

capable of targeting RNAP to selectively transcribe specific genes.[16,17] These sigma factors belong to one of two classes: σ^{70} or σ^{54} (often called σ^{N}). Both σ^{70} and σ^{54} are able to bind to RNAP and their promoter region to form a holoenzyme-activator complex. The major difference is that systems with σ^{70} will spontaneously induce DNA melting, generating the transcriptionally active open complex,[18] whereas σ^{54} requires co-activation to generate the open complex. Overall, σ^{54} binds tighter to its promoter elements compared to σ^{70}, therefore leading to the differences between both families. Due to its low binding affinity, it is able to bind without RNAP-complexing. Thus far, it is the only σ factor outside of the σ^{70} family, prompting over 30 years of research to understand the domain organization of σ^{54}.

Sigma factors bind to the promoter element recognition site, which is upstream of the transcriptional start site. In general, the promoter element is found centered at -12[19] and -24[20] nucleotides from the transcriptional start site for σ^{54}. In the case of σ^{70} the promoter is approximately -10 and -35 from the transcriptional start site.[21,22] In addition, σ^{54} differs from σ^{70} as it requires binding of an enhancer binding protein (EBP) to an upstream activator sequence (UAS) to initiate transcription. These bacterial EBPs[23–25] are similar in structure and function to AAA^{+} ATPase proteins.[26] In general, DNA looping is assisted by integration host factors (IHFs) and is heavily implicated in the regulation of RNAP with its promoters.[27,28] Additionally, IHFs confer another level of specificity by selectively bending the bEBPs bound to meet with RNAP positioned at an exact interface. bEBPs hydrolyze ATP and use the mechanical energy to change the conformation in the holoenzyme to stabilize an open complex and compensate for the higher energy difference between both families. As a result, bEBPs are capable of interacting with the RNAP-σ^{54} complex to initiate transcription.[29–31] Many bEBPs are required in the different pathways under σ^{54} regulation.

Since there are many σ^{54} promoter sequences in a genome, bEBPs are required to confer selectivity to the genes that are transcribed.

2.2.2 Genes under σ^{54} regulation

The sections below describes three systems under σ^{54} regulation that make use of the same transcriptional pathways as described above. σ^{54} activation is known to occur in nutrient-limited conditions and during infection. These system are under investigation due to their links to nitrogen and carbon metabolism, or virulence properties such as flagellar motility and biofilm formation. By monitoring these properties, the changes in these genes' expression should be linked to phenotypic outcomes related to antivirulence in pathogenicity.

2.2.2.1 *GlnA* Nitrogen Assimilation

In 1985, nitrogen starvation studies have demonstrated that a σ^{54} binding site is located upstream of the glutamine synthetase gene: *glnA*.[32–34] In this native environment, *Xylella fastidiosa* must cope with the nitration limitations of low variety of environmental amino acids.[35] Da Silva *et* al. has shown in DNA microarray experiments of global gene expression that σ^{54} regulates ammonium assimilation from *glnA* gene expression in this bacteria.[36] In *E. coli* and other enterobacteriaceae, similar phenomena are observed in mammalian environments with nitrogen-limiting environments, thus inducing ammonium and nitrogen-scavenging pathways.[37] A number of these genes are transcribed through RNAP-σ^{54} and bEBP activation.[37,38] This hexameric bEBP, NtrC, is thought to have three domains, one DNA-binding domain, one ATPase domain, and a receiver domain that becomes phosphorylated to induce activation.[38] Glutamine synthetase expression is under regulatory control of this NtrC-RpoN pathway.

2.2.2.2 *Psp* Operon-Regulated Virulence

In 1991, σ^{54} was linked to the expression of the phage shock protein (*psp*) operon.[39] This operon functions as a homeostatic mediator in response to stressors such as filamentous phage infection, alkalinity, and heat shock.[40,41] Within this operon, RNAP-σ^{54} mediated expression produces five genes in this operon, *pspA*, *B*, *C*, *D*, and *E*. Much like *glnA*, the activation of σ^{54} mediated transcription requires a bEBP, in this case PspF.[42] Interestingly, PspF is negatively regulated by PspA, thus creating a negative feedback loop to regulate expression from the psp operon.[43] PspF is thought to be induced through a disruption of membrane integrity and decreased proton motive force (PMF). Although its expression is not extensively triggered unless stressed, it is implicated in repairing damage to the inner cell membrane[44] and promoting maintenance of PMF by inducing anaerobic respiration.[45]

Although these effects are seemingly homeostatic in nature, the PMF plays a significant role in a variety of virulent processes. As many types of bacteria use Type III Secretion Systems to cause virulence, the secretin components are toxic to mammalian cells as they form pores in membranes.[46] PspC inactivation was shown to sensitize *Y. enterocolitica*,[47] causing growth defects due to secretin insertion within the cytoplasmic membrane and decreased PMF. This may be due to self-induced death due to a lack of protection from secreted toxins. PspF mutants have been shown to fail to maintain minimum PMF required for survival.[48] Inactive PMF leads to a decrease in protein export and flagellar motility.[49] Although not a direct synthesizer, the *psp* operon has been shown to overexpress in concert with other genes to form biofilms in *Y. enterolitica*.[50]

2.2.2.3 *AtoD* Short-Chain Fatty Acid Catabolism

The *atoDAEB* regulatory locus codes for a group of enzymes involved in short-chain fatty acid metabolism, which was elucidated in 1987.[51] AtoC has been long known to positively regulate the operon. Acetoacetate, a four-carbon β-keto short-chain fatty acid, is degraded to acetyl-CoA by this operon.[51] Since 2007, σ^{54} has been linked to this metabolic node based on bioinformatic sequence studies.[52] If these genes are compared to the *glnA* operon, AtoC appears to fulfill the same functions as NtrC, and is likely a bEBP. Little is known apart from the fatty acid metabolism of small carbon sources. AtoC has been shown to be a posttranslational regulator of polyamine biosynthetic enzymes. It is believed that this link to polyamines is connected to genes with flagellar biosynthesis, among other genes;[53] this work is still in its infancy.

2.2.3 Targeting the σ^{54}-DNA PDI as a transcription inhibition antivirulent

Over the course of infection, bacteria and host cells compete against one another for nitrogen and carbon energy sources. As protein sources become scarce, ammonium naturally produced from the urea cycle must be used as an energy source, leading to the upregulation of *glnA* expression. Due to the hostile environment of the host during infection, bacteria initiate the stringent response, a bacterial stress response activated during nutrient limitation conditions. σ^{54} becomes activated based on a deficient concentration of guanosine pentaphosphate,[54,55] carbon, and nitrogen energy sources. Apart from common sugars, bacteria can make use of acetoacetate by upregulating the *ato* regulon's expression. As *glnA* is regulated by σ^{54}, the cofactor's expression and many σ^{54}-regulated genes have increased expression within these environmental conditions. Upon increased expression, genes like

pspA, contributors to virulent activity, will increase both the infectivity and durability of the pathogens.

One way to approach this problem would be to inhibit the bacteria's ability to process ammonia from its environment. This can be done by interrupting σ^{54}'s functioning. By interrupting the bacteria's nitrogen and carbon sources, these cells must outcompete infected mammalian cells for nutrients with inoperative pathways. At the same time, the virulent activities such as motility, biofilm formation, and secretin secretion will be downregulated and the bacteria's native defence mechanisms will be weakened. By removing both metabolism and virulent properties, the cells will be more susceptible to attack from their environment.

To prevent the expression of these genes all together, we propose that a stapled α-helical peptide can be used to interrupt the PDI of the RNAP-σ^{54}-DNA complex. With the downregulation of virulence, the host's own immune defences would be able to clear the infection more easily. The bacteria will be killed through the use of an anti-σ^{54} drug in concert with the body's natural immunity. By approaching antimicrobial therapeutics from this method, bacteria will not undergo the selective pressures of normal bactericidal antibiotics that encourage the emergence of resistance mechanisms. Furthermore, these synthetic peptides are less likely to awaken resistance enzymes due to their natural protease-resistant properties.

2.3 FtsZ as a target for stapled peptide antibiotic therapeutics

As it has been demonstrated many times that stapled peptides can activate or interrupt essential processes in mammalian cells, we hypothesize that this is possible in essential

bacterial processes that feature extensive PDIs. By making use of the comprehensive literature available for the unique PDIs in bacteria, bacteriostatic and bactericidal agents may be produced by targeting these interactions. FtsZ represents one of these targets of interest.

2.3.1 FtsZ polymerization and Z-ring membrane anchoring

Bacterial cells divide through a mechanochemical septation process of membrane constriction at the divisome. FtsZ, a structural GTPase homologue to tubulin in humans,[56] localizes at the nascent division site early in the cell division process and remains with the invaginating septum during cytokinesis.[57] GTPase activity has been shown to mediate the polymerization of FtsZ monomers into a ring-structure called the Z-ring.[58] This ring acts as a scaffold to recruit downstream division proteins and to coordinate peptidoglycan synthesis, membrane fission, and septation.

ZipA and FtsA, bitopic membrane-bound proteins, are known to attach FtsZ to the inner membrane in *E. coli*.[59] Studies with FtsA have shown artificial liposome division with FtsZ and demonstrate force generation caused by Z-ring contraction.[60] ZipA protects FtsZ from ClpXP-directed degradation by blocking the interaction site while stabilizing FtsZ to form the membrane-attached septum.[61] MinC, a cell division inhibitor, also interacts with FtsZ to localize Z-ring formation primarily at the middle of the cell.[62] In each of these interactions, they bind to the C-terminus of FtsZ.[59] This indicates that FtsZ acts as a central hub for cell division as its regulation is controlled by four other enzymes.[63] Slight variations in the FtsZ C-terminus provide selectivity in protein interactions between species.[64] Upon 3D-structured illumination microscopy, a form of super resolution microscopy, FtsZ filaments have been observed as fragments rather than a fully joined ring structure.[65] These fragments overlap to form loose bundles with increasing radial thickness. Although it is not

completely understood, it has been shown that these bundles generate the force necessary to induce cytokinesis.

2.3.2 Targeting the ZipA-FtsZ PPI as an anti-cytokinesis antibiotic

Methods that target FtsZ and prevent the Z-ring from causing either attachment or constriction would prevent cytokinesis. The ZipA-FtsZ interaction is an ideal candidate to begin the exploration of a novel antimicrobial-acting stapled peptide. Based on Western blotting, the ratio of FtsA:FtsZ is 1:5 whereas the ZipA:FtsZ is 1:3;[66] this suggests that its blocking degradation properties may be highly necessary along various points on the Z-ring. The effects of both overexpression and deletion of *zipA* have demonstrated a lack of septation, preventing cell division.[67] ZipA appears to have higher homology in Gram negative bacteria but remains sparse in Gram positive bacteria[68]. Although deletion of *zipA* does not prevent Z-ring formation, it does reduce the number of rings generated.[69] Furthermore, both FtsZ[70] and ZipA[71] inhibitors are currently under development .

We propose that stapled peptide analogs of FtsZ's C-terminus will be capable of disrupting cell division in bacterial cells, while retaining a high level of selectivity relative to mammalian cells. Membrane anchors will be saturated with the stapled peptide as the staple will be installed while avoiding important interactions specific to ZipA-FtsZ, thus preventing the membrane anchoring necessary for septation and inhibiting cell division. Because FtsZ plays a role in a number of different protein-protein interactions, a number of peptides and staple lengths will be tested to determine if binding of proteins other than ZipA are impacted. While MinC- and ClpXP-directed degradation may be prevented with this FtsZ analog, the membrane anchoring proteins will also be targeted and the Z-ring will be unable

to induce membrane constriction. Overall, FtsZ stapled peptide analogs should prevent cell division in cells.

2.4 Conclusions and Prospects

Although small molecules have successfully demonstrated both antibiotic and antivirulent activity, their mechanism of action leads to resistance. For antivirulent compounds to be taken to the clinic, a non-resistance-inducing molecule must be created to bring attention to the class's value. New antibiotic targets must be investigated with anti-resistance classes of compounds to create clinically relevant antibiotics. To study both σ^{54} and FtsZ in Gram negative bacteria, the problems associated with cell penetration, disruption of extensive PPIs, the emergence of resistance, and specificity to prokaryotic organisms over eukaryotes must be taken into account.

Development of rationally designed stapled peptides that target these proteins and their PPIs will help to address these issues. As these neither target has yielded clinically approved molecules, stapled peptides may be the first step towards the next class of chemotherapy against bacteria.

2.5 References

1. Lock, R. L. & Harry, E. J. Cell-division inhibitors: new insights for future antibiotics. *Nat. Rev. Drug Discov.* **7,** 324–338 (2008).

2. Projan, S. J. & Youngman, P. Antimicrobials: new solutions badly needed. *Curr. Opin. Microbiol.* **5,** 463–465 (2002).

3. Lewis, K. Platforms for antibiotic discovery. *Nat. Rev. Drug Discov.* **12,** 371–87 (2013).

4. Blair, J. M. A. *et al.* Molecular mechanisms of antibiotic resistance. *Nat. Rev. Microbiol.* **13,** 42–51 (2015).

5. Oh, K.-B. *et al.* Discovery of diarylacrylonitriles as a novel series of small molecule sortase A inhibitors. *J. Med. Chem.* **47,** 2418–21 (2004).

6. Gerdt, J. & Blackwell, H. Competition studies confirm two major barriers that can preclude the spread of resistance to quorum-sensing inhibitors in bacteria. *ACS Chem. Biol.* **9,** 2291–2299 (2014).

7. Rasko, D. A. *et al.* Targeting QseC Signaling and Virulence for Antibiotic Development. *Science* **321,** 1078–1080 (2008).

8. Ruer, S. *et al.* Virulence-targeted Antibacterials: Concept, Promise, and Susceptibility to Resistance Mechanisms. *Chem. Biol. Drug Des.* **86,** 379–399 (2015).

9. Clarke, M. B. *et al.* The QseC sensor kinase: a bacterial adrenergic receptor. *Proc. Natl. Acad. Sci. U. S. A.* **103,** 10420–5 (2006).

10. Hung, D. T. *et al.* Small-molecule inhibitor of Vibrio cholerae virulence and intestinal colonization. *Science* **310,** 670–674 (2005).

11. Smith, K. M. *et al.* Library Screening for Synthetic Agonists and Antagonists of a Pseudomonas aeruginosa Autoinducer. *Chem. Biol.* **10,** 563–571 (2003).

12. Ganguly, K. *et al.* Design, synthesis, and a novel application of quorum-sensing agonists as potential drug-delivery vehicles. *J. Drug Target.* **19,** 528–539 (2011).

13. Pinkner, J. S. *et al.* Rationally designed small compounds inhibit pilus biogenesis in uropathogenic bacteria. *Proc. Natl. Acad. Sci. U. S. A.* **103,** 17897–902 (2006).

14. Maeda, T. *et al.* Quorum quenching quandary: resistance to antivirulence compounds. *ISME J.* **6,** 493–501 (2012).

15. Burgess, R. R. *et al.* Factor Stimulating Transcription by RNA Polymerase. *Nature* **224,** 43–46 (1969).

16. Bush, M. & Dixon, R. The Role of Bacterial Enhancer Binding Proteins as Specialized Activators of 54-Dependent Transcription. *Microbiol. Mol. Biol. Rev.* **76,** 497–529 (2012).

17. Francke, C. *et al.* Comparative analyses imply that the enigmatic sigma factor 54 is a central controller of the bacterial exterior. *BMC Genomics* **12,** 385 (2011).

18. Brodolin, K. *et al.* Remodeling of the σ70 subunit non-template DNA strand contacts during the final step of transcription initiation. *J. Mol. Biol.* **350,** 930–937 (2005).

19. Wang, L. & Gralla, J. D. Multiple in vivo roles for the -12-region elements of sigma 54 promoters. *J. Bacteriol.* **180,** 5626–5631 (1998).

20. Burrows, P. C. *et al.* Mapping σ54-RNA polymerase interactions at the -24 consensus promoter element. *J. Biol. Chem.* **278,** 29728–29743 (2003).

21. Wong, C. *et al.* The Domain Structure of σ54 as Determined by Analysis of a Set of Deletion Mutants. *J. Mol. Biol.* **236,** 81–90 (1994).

22. Barrios, H. *et al.* Compilation and analysis of σ54-dependent promoter sequences. *Nucleic Acids Res.* **27,** 4305–4313 (1999).

23. Joly, N. *et al.* ATPase Site Architecture Is Required for Self-Assembly and Remodeling Activity of a Hexameric AAA+ Transcriptional Activator. *Mol. Cell* **47,** 484–490 (2012).

24. Rappas, M. *et al.* Bacterial enhancer-binding proteins: unlocking σ54-dependent gene transcription. *Curr. Opin. Struct. Biol.* **17,** 110–116 (2007).

25. Schumacher, J. *et al.* ATP-dependent transcriptional activation by bacterial PspF AAA+protein. *J. Mol. Biol.* **338,** 863–875 (2004).

26. Studholme, D. J. & Dixon, R. Domain architectures of σ54-dependent transcriptional activators. *J. Bacteriol.* **185,** 1757–1767 (2003).

27. Hoover, T. R. *et al.* The integration host factor stimulates interaction of RNA polymerase with NIFA, the transcriptional activator for nitrogen fixation operons. *Cell* **63,** 11–22 (1990).

28. Arfin, S. M. *et al.* Global gene expression profiling in Escherichia coli K12: The effects of integration host factor. *J. Biol. Chem.* **275,** 29672–29684 (2000).

29. Zhang, N. *et al.* A key hydrophobic patch identified in an AAA+ protein essential for its in trans inhibitory regulation. *J. Mol. Biol.* **425,** 2656–2669 (2013).

30. Sysoeva, T. A. *et al.* Nucleotide-induced asymmetry within ATPase activator ring drives σ^{54}-RNAP interaction and ATP hydrolysis. *Genes Dev.* **27,** 2500–2511 (2013).

31. Huo, Y. X. *et al.* IHF-binding sites inhibit DNA loop formation and transcription initiation. *Nucleic Acids Res.* **37,** 3878–3886 (2009).

32. Hunt, T. P. & Magasanik, B. Transcription of glnA by purified Escherichia coli components: core RNA polymerase and the products of glnF, glnG, and glnL. *Proc. Natl. Acad. Sci. U. S. A.* **82,** 8453–8457 (1985).

33. Hirschman, J. *et al.* Products of nitrogen regulatory genes ntrA and ntrC of enteric bacteria activate glnA transcription in vitro: Evidence that the ntrA product is a σ factor. *Proc. Natl. Acad. Sci. U. S. A.* **82,** 7525–7529 (1985).

34. Reitzer, L. J. *et al.* Mutations that create new promoters suppress the sigma 54 dependence of glnA transcription in Escherichia coli. *J. Bacteriol.* **169,** 4279–4284 (1987).

35. Pate, J. S. *et al.* Nitrogen Nutrition and Xylem Transport of Nitrogen in Ureide-producing Grain Legumes. *Plant Physiol.* **65,** 961–965 (1980).

36. Da Silva Neto, J. F. *et al.* Global gene expression under nitrogen starvation in Xylella fastidiosa: contribution of the σ54 regulon. *BMC Microbiol.* **10,** 231 (2010).

37. Zimmer, D. P. *et al.* Nitrogen regulatory protein C-controlled genes of Escherichia coli: scavenging as a defense against nitrogen limitation. *Proc. Natl. Acad. Sci. U. S. A.* **97,** 14674–14679 (2000).

38. De Carlo, S. *et al.* The structural basis for regulated assembly and function of the transcriptional activator NtrC. *Genes Dev.* **20,** 1485–1495 (2006).

39. Weiner, L. *et al.* Stress-induced expression of the Escherichia coli phage shock protein operon is dependent on σ54 and modulated by positive and negative feedback mechanisms. *Genes Dev.* **5,** 1912–1923 (1991).

40. Elderkin, S. *et al.* Mechanism of action of the Escherichia coli phage shock protein PspA in repression of the AAA family transcription factor PspF. *J. Mol. Biol.* **320,** 23–37 (2002).

41. Brissette, J. L. *et al.* Phage shock protein, a stress protein of Escherichia coli. *Proc. Natl. Acad. Sci. U. S. A.* **87,** 862–866 (1990).

42. Bordes, P. *et al.* The ATP hydrolyzing transcription activator phage shock protein F of Escherichia coli: identifying a surface that binds sigma 54. *Proc. Natl. Acad. Sci. U. S. A.* **100,** 2278–2283 (2003).

43. Dworkin, J. *et al.* The PspA protein of Escherichia coli is a negative regulator of σ54-dependent transcription. *J. Bacteriol.* **182,** 311–319 (2000).

44. Kobayashi, R. *et al.* Escherichia coli phage-shock protein A (PspA) binds to membrane phospholipids and repairs proton leakage of the damaged membranes. *Mol. Microbiol.* **66,** 100–109 (2007).

45. Kleerebezem, M. *et al.* Involvement of stress protein PspA (phage shock protein A) of Escherichia coli in mmaintenance of the protonmotive force under stress conditions. *EMBO J.* **15,** 162–171 (1996).

46. Darwin, A. J. & Miller, V. L. The psp locus of Yersinia enterocolitica is required for virulence and for growth in vitro when the Ysc type III secretion system is produced. *Mol. Microbiol.* **39,** 429–444 (2001).

47. Joly, N. *et al.* Managing membrane stress: The phage shock protein (Psp) response, from molecular mechanisms to physiology. *FEMS Microbiol. Rev.* **34,** 797–827 (2010).

48. Jovanovic, G. *et al.* Induction and function of the phage shock protein extracytoplasmic stress response in Escherichia coli. *J. Biol. Chem.* **281,** 21147–21161 (2006).

49. Minamino, T. & Namba, K. Distinct roles of the FliI ATPase and proton motive force in bacterial flagellar protein export. *Nature* **451,** 485–488 (2008).

50. Beloin, C. *et al.* Global impact of mature biofilm lifestyle on Escherichia coli K-12 gene expression. *Mol. Microbiol.* **51,** 659–674 (2004).

51. Jenkins, L. S. & Nunn, W. D. Genetic and molecular characterisation of the genes involved in short-chain fatty-acid degradation in Escherichia coli: the ato system. *J. Bacteriol.* **169,** 42–52 (1987).

52. Grigoroudis, A. I. *et al.* Molecular modeling and functional analysis of the AtoS-AtoC two-component signal transduction system of Escherichia coli. *Biochim. Biophys. Acta* **1770,** 1248–1258 (2007).

53. Yoshida, M. *et al.* A unifying model for the role of polyamines in bacterial cell growth, the polyamine modulon. *J. Biol. Chem.* **279,** 46008–46013 (2004).

54. Laurie, A. D. *et al.* The Role of the Alarmone (p)ppGpp in σN Competition for Core RNA Polymerase. *J. Biol. Chem.* **278,** 1494–1503 (2003).

55. Srivatsan, A. & Wang, J. D. Control of bacterial transcription, translation and replication by (p)ppGpp. *Curr. Opin. Microbiol.* **11,** 100–105 (2008).

56. De Boer, P. *et al.* The essential bacterial cell-division protein FtsZ is a GTPase. *Nature* **359,** 254–256 (1992).

57. Dai, K. & Lutkenhaus, J. FtsZ is an Essential Cell Division Gene in Escherichia coli. *J Bacteriol* **173,** 3500–3506 (1991).

58. Addinall, S. G. *et al.* FtsZ ring formation in fts mutants. *J. Bacteriol.* **178,** 3877–3884 (1996).

59. Pazos, M. *et al.* A specific role for the ZipA protein in cell division: Stabilization of the FtsZ protein. *J. Biol. Chem.* **288,** 3219–3226 (2013).

60. Osawa, M. & Erickson, H. P. Liposome division by a simple bacterial division machinery. *Proc. Natl. Acad. Sci. U. S. A.* **110,** 11000–4 (2013).

61. Camberg, J. L. *et al.* ClpXP protease degrades the cytoskeletal protein, FtsZ, and modulates FtsZ polymer dynamics. *Proc. Natl. Acad. Sci. U. S. A.* **106,** 10614–10619 (2009).

62. Mosyak, L. *et al.* The bacterial cell-division protein ZipA and its interaction with an FtsZ fragment revealed by X-ray crystallography. *EMBO J.* **19,** 3179–3191 (2000).

63. Shen, B. & Lutkenhaus, J. Examination of the interaction between FtsZ and MinCN in E. coli suggests how MinC disrupts Z rings. *Mol. Microbiol.* **75,** 1285–1298 (2010).

64. Buske, P. J. & Levin, P. A. Extreme C terminus of bacterial cytoskeletal protein FtsZ plays fundamental role in assembly independent of modulatory proteins. *J. Biol. Chem.* **287,** 10945–10957 (2012).

65. Strauss, M. P. *et al.* 3D-SIM Super Resolution Microscopy Reveals a Bead-Like Arrangement for FtsZ and the Division Machinery: Implications for Triggering Cytokinesis. *PLoS Biol.* **10,** (2012).

66. Rueda, S. *et al.* Concentration and assembly of the division ring proteins FtsZ, FtsA, and ZipA during the Escherichia coli cell cycle. *J. Bacteriol.* **185,** 3344–3351 (2003).

67. Hale, C. A. & De Boer, P. A. J. Direct binding of FtsZ to ZipA, an essential component of the septal ring structure that mediates cell division in E. coli. *Cell* **88,** 175–185 (1997).

68. RayChaudhuri, D. ZipA is a MAP-Tau homolog and is essential for structural integrity of the cytokinetic FtsZ ring during bacterial cell division. *EMBO J.* **18,** 2372–2383 (1999).

69. Hale, C. A. & De Boer, P. A. J. Recruitment of ZipA to the Septal Ring of Escherichia coli Is Dependent on FtsZ and Independent of FtsA. *J. Bacteriol.* **181,** 167–176 (1999).

70. Keffer, J. L. *et al.* Chrysophaentins are competitive inhibitors of FtsZ and inhibit Z-ring formation in live bacteria. *Bioorganic Med. Chem.* **21,** 5673–5678 (2013).

71. Tsao, D. H. H. *et al.* Discovery of novel inhibitors of the ZipA/FtsZ complex by NMR fragment screening coupled with structure-based design. *Bioorganic Med. Chem.* **14,** 7953–7961 (2006).

Chapter 3

RpoN-based Stapled α-helical Peptides Permeate Bacteria and Exhibit Antivirulence Effects in Escherichia coli *and* Pseudomonas aeruginosa

3.1 Introduction

In this chapter, we discuss the design, synthesis, and testing of a stapled peptide imitating the DNA-binding domain of σ^{54} in the efforts to understand if stapled peptides are able to interrupt protein-DNA binding. Furthermore, this chapter seeks to discover whether stapled peptides can target new targets within a new, untested model host: bacteria.

3.1.1 σ^{54} Binding Complex

A number of structural studies have confirmed the binding of the σ^{54} cofactor to RNA polymerase (RNAP). Preliminary work on σ^{54} sought to identify the binding domain through classical footprinting[1] and alanine mutation studies.[2] Footprinting studies were able to isolate the promoter regions in which σ^{54} bound to DNA which narrows both the target and range of DNA that may be examined. Alanine mutational work determined the exact base pairs in which σ^{54} was binding through binding affinity examination. Relative to the +1 transcription site, σ^{54} generally binds to the -24/-12 site to initiate DNA melting.[3–7] Further protein studies identified a 66 amino acid long helix-turn-helix motif in *Aquifex aeolicus*[8] and elucidated its protein NMR structure of this interaction.[9] The N-terminal end of σ^{54} points to the -12 promoter element[1] whereas the C-terminal adopts a helix-turn-helix (HTH) motif. Within this motif, the α-helix essential to binding to DNA is termed the RpoN box (A**RR**TVA**KYR**E) at residues 377 to 386 (*PDB*: 2O8K).[9] Arg378, Arg379, Tyr384 and Arg385 were found to decrease DNA binding the most when replaced with alanine residues, as shown in bold, with Lys383 having a modest reduction in binding.[10]

The protein NMR structure shows that this sequence interacts with the -24 region (5'-TGGCACG-3') of the promoter sequence with high affinity (K_d = 114 ± 10 nM).[9] Arg378

and Arg379 are localized to the -24 element of the interaction and make multiple hydrogen bonding and ionic interactions with Gua-25 and Gua-26 on the non-coding strand of DNA based on significant line-broadening of a ^{15}N-HSQC spectrum.[9] Ala377 and Thr380 hydrogen bond with the phosphate of Thy -23 with the hydroxyl group of Thr380 interacting with the DNA backbone as well. Lys383 is localized to the major groove to hydrogen bond with O4 of Thy -23 or N7 of Gua -25.[9]

3.1.2 Functional design of RpoN-based σ^{54} stapled peptides

The RpoN-based σ^{54} stapled peptides are designed as inhibitors of the binding of DNA to the RNAP-σ^{54} complex (**Fig. 3.1**). The concept is similar to that of vaccination; a microorganism becomes attenuated while the host builds immune defences to overwhelm the invaders and clear infection without further pharmacological intervention. Once the binding has been inhibited through these peptides, the pathogenicity of bacteria that display σ^{54}-regulated virulence will decrease, thus attenuating the bacteria. With weakened invaders, host immune defences will naturally clear antibiotic-resistant bacterial infections while building immunity to future exposure. This will have a major clinical benefit as it will enable the host to clear bacterial infections more rapidly while mirroring the previous successes of vaccination efforts.

The peptides themselves are not targeting an essential gene. In theory, these molecules will not be bactericidal like conventional antibiotics. They are less likely to initiate drug resistance mechanisms due to two reasons: stapled peptides are highly resistant to native proteases due to their locked cyclic nature, and these peptides do not apply a strong life-or-death selective pressure compared to current antibiotics. It is expected that they will work

well against multidrug resistant bacteria due to their different approach to combatting bacteria.

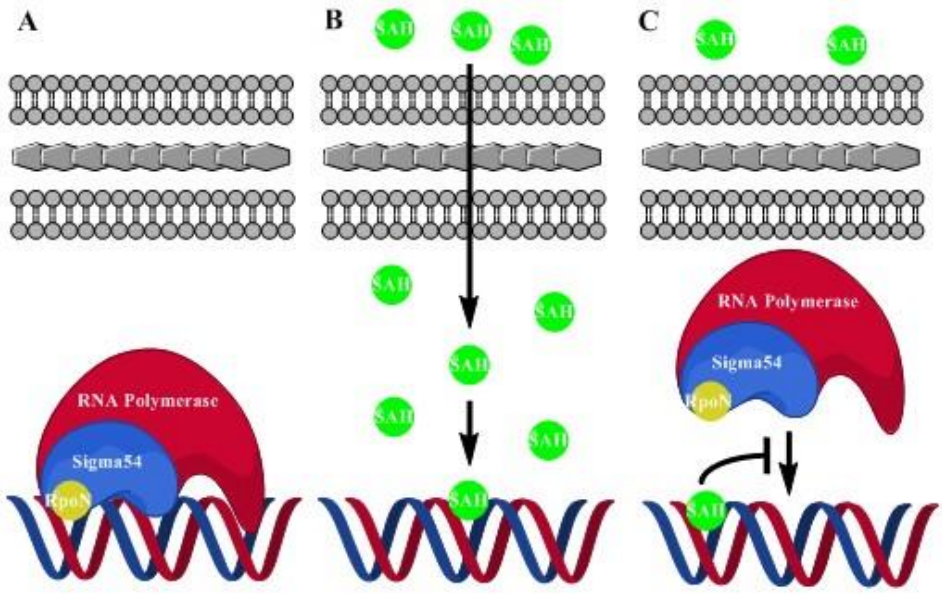

Figure 3.1. Schematic of stapled α-helical peptide as it interrupts transcriptional regulation. **A)** Cell without treatment, **B)** σ^{54} modeled stapled peptides as they penetrate the Gran negative bacteria, and **C)** stapled peptides that inhibit σ^{54}-mediated transcription.

3.2 Results and Discussion

3.2.1 Peptide synthesis & viability screening

3.2.1.1 Peptide design and conceptualization

To begin the peptide design process, it must first be confirmed that the α-helix of interest is conserved well across various species of bacteria. It is critical to have structural data and complementary circular dichroism (CD) data that demonstrates that the protein domain of interest is indeed α-helical. With the Wemmer lab's protein NMR structural characterization of the PDI, it was shown that a single α-helix is the key binding interaction to stabilize the cofactor.[9] In **Fig. 3.2**, the analysis based on the protein NMR structure shows that the RpoN box is highly conserved across various Gram positive (*E. faecium and S.*

aureus) and Gram negative bacteria (*A. aeolicus, E. coli, P. aeruginosa, K. pneumoniae, A. baumannii and E. aerogenes*). With the full characterization of the DNA-protein binding domain, the stapled peptides were modeled according to the RpoN helix (FKVARRTVAKYREML) of *A. aeolicus* as seen in **Fig. 3.2**. Since σ^{54}'s RpoN domain has now been determined to be present in a variety of clinically relevant pathogens, the peptide can be tested as a model to knockdown the expression of σ^{54} with its DNA binding.

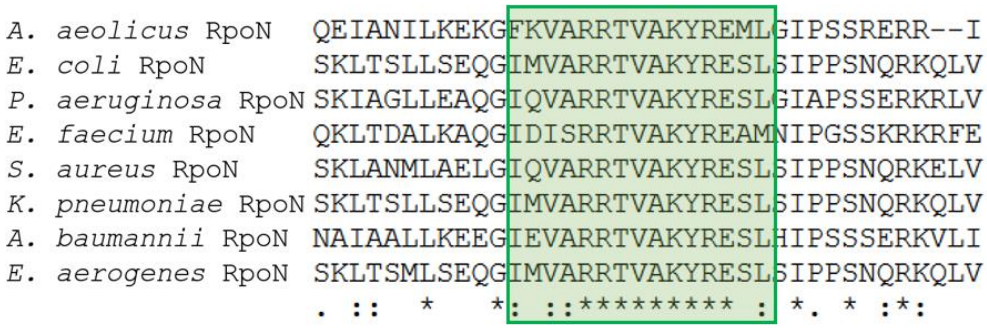

Figure 3.2. Sequence alignment of σ^{54} in a select number of bacteria for the RpoN box region. Peptides sequences match *Aquifex aeolicus* due to the crystal structure analysis of its σ^{54} binding. Both binding sites are conserved throughout multiple species of Gram negative bacteria. Sequences were generated from ClustalOmega. Blank spaces represent low levels of homology, periods represent partially homologous regions, colons represent highly homologous regions, and asterisks represent amino acids of consensus sequences. The green box depicts the sequence domain in which the peptide will imitate σ^{54}'s DNA-binding domain RpoN.

Secondly, both a charge assessment and helical wheel diagram must be constructed to determine the ideal placement of the staple relative to its structural data. In the case of σ^{54}, the staple placement must remain away from the DNA binding domain of the peptide. The overall charge of the peptide is +4 so it will likely be an ideal candidate to function *in vivo*. With a highly charged molecule, the solubility of the peptide in water will be high and its positive charge will allow passage through membranes. Furthermore, as the charge is not localized in adjacent areas on the sequence, staples can be placed to avoid specific residues.

Upon examination of the helical wheel diagram (**Fig.3.3**), it is evident that this α-helical interaction heavily relies on charged resides on one face and a mix of hydrophobic

and hydrophilic residues on the other side. As previously discussed, R7, R8, K12, and R14 are the key residues interacting with the σ^{54} promoter domain sequences.[9] DNA itself is negatively charged and its bases are in electron-rich areas. It appears that the RpoN box is clearly divided into half its face interacting with DNA and the other half with the rest of the σ^{54} protein. Staples can be placed in areas outside of the binding domain to confer the α-helicity without affecting binding affinity. In other peptide examples, the staple can align itself along the protein grooves to further increase binding affinity.[11] The staples were chosen in areas that likely border the DNA-σ^{54} interface to encourage increased binding affinity. Although stapled peptides binding to DNA is a new concept, these staples were designed to test whether these concepts may be transferable to general PDIs.

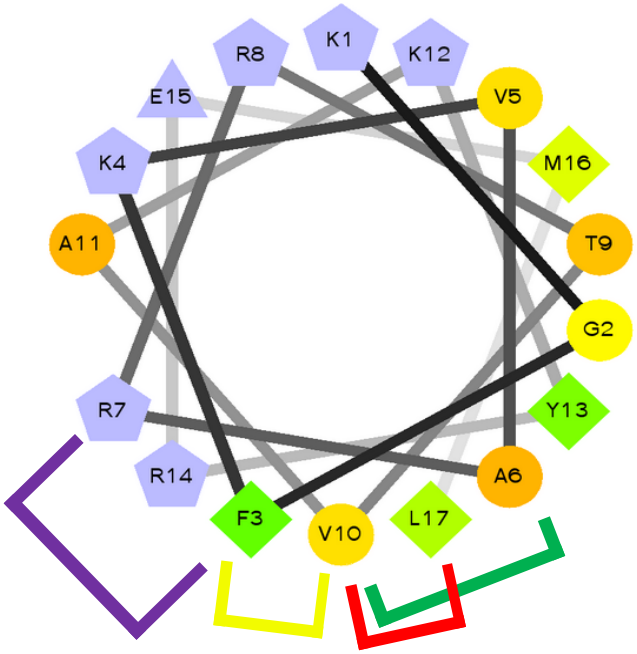

Figure 3.3. Helical wheel diagram of the RpoN box α-helix with hypothetical staples placed within the wheel. The amino acid sequence corresponds to the protein sequence KGFKVARRTVAKYREML. Hydrophilic residues are circles whereas hydrophobic ones are diamonds. Potentially negatively charge amino acids are triangular and positively charge ones are pentagons. Charged residues are in blue, hydrophobic residues in green, moderately hydrophilic residues in yellow and strongly hydrophilic residues are in orange. The red staple represents the staple for σ^{54}-1, green for σ^{54}-2, yellow for σ^{54}-3, and purple for σ^{54}-4. Helical wheel was generated by wheel.pl.

Four peptides were conceived based on the protein NMR structure of DNA binding with the σ^{54} cofactor in water.[9] As the stereochemical effects of *i*, *i*+4 stapled peptides have been well studied,[12] two combinations of staples that span approximately one helical turn were selected. Two *i*, *i*+7 peptides spanning approximately two helical turns were synthesized. These types of peptides have been less studied and, as a result, may exhibit different effects in bacteria. Since these peptides are an exploratory concept, it was decided to make both staple lengths to determine if their placement and length display similar behaviour in bacteria as compared to the previously reported mammalian cell studies.

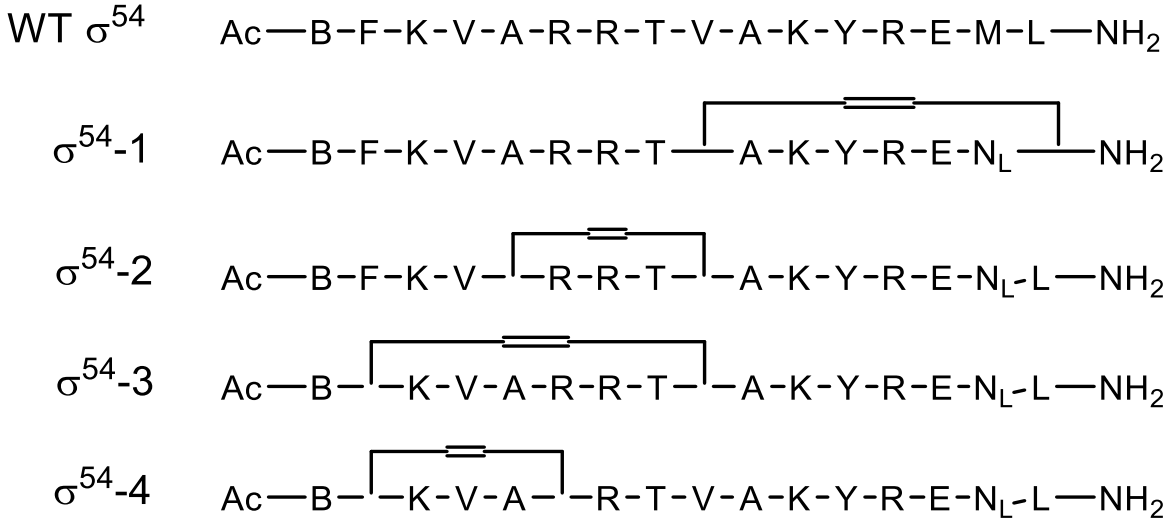

Figure 3.4. Acetyl-capped chemically synthesized σ^{54} stapled α-helical peptide analogs designed with varying staple length. B represents a β-alanine spacer, N_L represents norleucine, and the staple-like structure represents the locations of each staple within the peptides.

Stapled peptides were synthesized by the Bernal lab at the National Cancer Institute in Frederick, MD. Peptides 1 and 3 (i.e. σ^{54}-1 and σ^{54}-3) were placed at hydrophobic sites with one common amino acid on the helical wheel diagram (**Fig.3.3**). Peptides 2 and 4 (i.e. σ^{54}-2 and σ^{54}-4) make use of a smaller staple (**Fig.3.4**) to study if the α-helical constraints of staple size posed problems to the properties of the peptides.

In particular, peptide 4 includes a knockout element in its design. A partial knockout of one of the binding residues will assist in understanding the number of interactions necessary to bind for an appreciable phenotypic effect. By decreasing both the charge and its supposed binding affinity, peptide 4 will provide the chance to observe tunable affinity of stapled peptides. Based on observations of the Bernal lab, staples placed towards the N-terminus of the peptide sequence tend to exhibit a higher α-helical character. This set of peptides could be used to understand the effects of staple placement with PDIs.

3.2.1.2 Peptide chemical synthesis

By making use of the Bernal lab's expertise in solid-phase peptide synthesis (SPPS), all four peptides were synthesized on Rink amide resin in a TETRAS peptide synthesizer from Advanced ChemTech. In brief, Rink amide resin was used to support peptides synthesized in the C to N direction. This direction was used because the amino acids were Fmoc-protected at the N-terminus. As the amino acid R groups lacked Fmoc in their protecting groups, this would confer specific functionalization at the terminal position once cleaved while allowing the rest of the peptide to remain protected. The general principle of SPPS is to repeat the cycles of wash-couple-wash-deprotection. (**Fig. 3.5** for synthetic scheme). By adding HCTU and DIPEA to increase the coupling reactivity, each monomer was added sequentially until fully grown. Depending on the purpose of the peptide, it was capped with either acetic anhydride or fluorescein and cleaved from the resin using standard TFA-mediated cleavage. The crude peptide was purified by HPLC and characterized by high-resolution mass spectrometry. The final mass was taken and the peptides were analyzed by nanodrop to ensure purity. In all cases, peptides of greater than 95% purity were obtained.

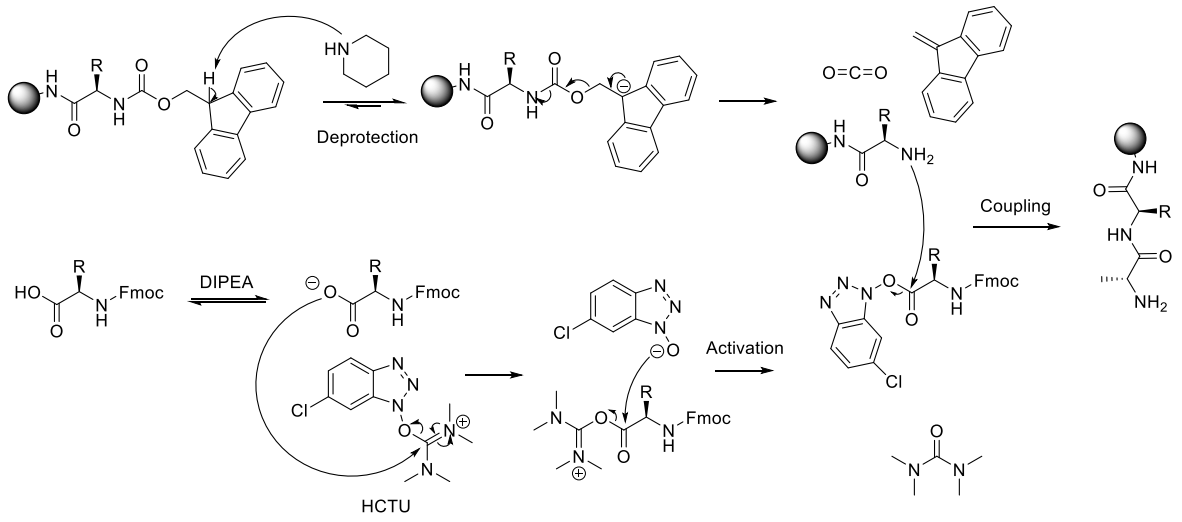

Figure 3.5. General synthetic scheme of the solid-phase peptide synthesis of stapled alpha-helical peptides. This process is repeated for the addition of each amino acid monomer.

3.2.1.3 Circular Dichroism assessment

CD was used to determine the α-helical nature of these peptides. In the context of peptides, CD is used to detect the secondary structure of a molecule or protein based on the differences between left-handed and right-handed circularly polarized light across multiple stereogenic chromophores.[13] By examining the profile of the far-UV spectrum of light, an α-helix is characterized by a two-trough character at 208 and 222 nm.[13,14]

All synthesized peptides, along with the unstapled controls, were examined with circular dichroism in aqueous solution. As shown in **Fig. 3.6**, the unstapled peptide lacks secondary structure as evidenced by the absorbance profile of only a negative peak at less than 200 nm. Each of the stapled peptides displays an α-helical character based on a negative peak at the two characteristic absorbances. However, as CD displays the summation of a molecules secondary structure, it appears that the peptides have some unordered character as the 208 nm trough is deeper than the 222 nm rather than the opposite.

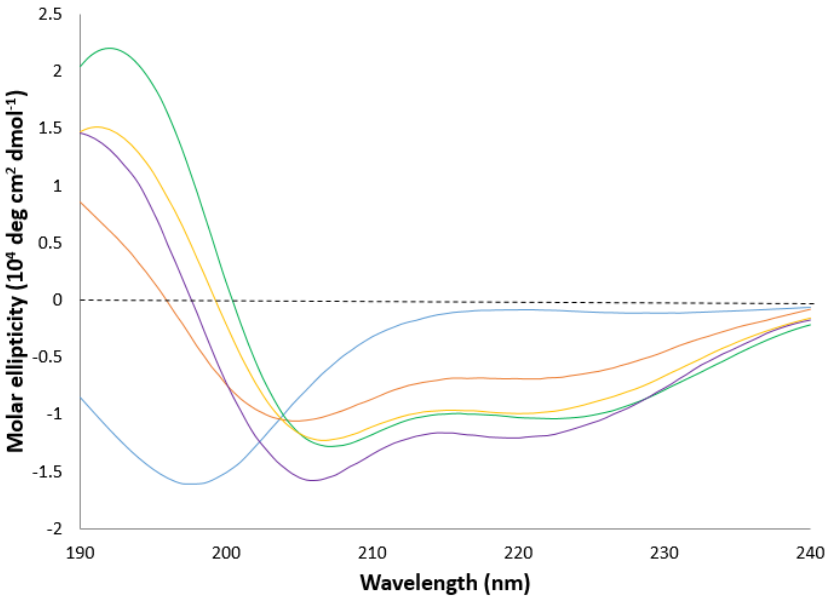

Figure 3.6. Circular dichroism spectrum of chemically synthesized peptides at 60-77 μM. Blue represents the WT-σ^{54} unstapled peptide, red for σ^{54}-1, green for σ^{54}-2, yellow for σ^{54}-3, and purple for σ^{54}-4 (n = 8).

3.2.1.4 Minimum Inhibitory Concentration

These peptides have been designed to inhibit virulent activity of Gram negative bacteria exhibiting σ^{54} regulation. It is necessary to determine whether cells will die due to the peptide's innate properties as opposed to displaying inhibitory effects. To assess the peptide's antimicrobial activity, we used a modified version of the microbroth dilution method of clinical minimal inhibitory concentration (MIC) assay from the National Committee for Clinical Laboratory Standards.[15]

Table 1: MIC Results of σ^{54} peptides in BW25113 *E. coli* cells using the microbroth dilution method (n = 3)

Peptide	MIC (μg/mL)
Cells alone	>512
0.4% DMSO	>512
Wild-type σ^{54}	>512
Stapled σ^{54} Helix 1	32
Stapled σ^{54} Helix 2	32
Stapled σ^{54} Helix 3	64
Stapled σ^{54} Helix 4	128

The MIC value was measured to verify that bacteria were not dying at low concentrations and to ensure that the peptides' σ^{54} inhibitory effect could be detected at reasonable concentrations. As all values are above 32 μg/mL, these compounds do not exhibit significant antibiotic activity. If we compare this molecule to other classes of commercially available antibiotics, compounds that exhibit MIC values less than 4 μg/mL are taken to be used as practical clinical antibiotics.[15] From **Table 1**, we can conclude that concentrations below these values should be used to validate the antivirulence activity of σ^{54} stapled peptide analogs. The peptides themselves lack bactericidal tendencies as designed.

3.2.1.5 Cytotoxicity evaluation

Traditionally, the MTT colorimetric assay has been used to assess cell viability and proliferation in a quantitative way. MTT, a yellow tetrazole salt, is reduced to formazan, a blue-purple and its absorbance is quantified through plate reading between 500 and 600 nm.[16–18] The weakness of the MTT method is that is uses mitochondrial reductase from the electron transport chain to reveal live cells, thus conferring a reliance on metabolically active cells.[19] Since σ^{54} is highly linked to a variety of metabolic functions, another assay was used. As a result, cell viability experiment using CellTiter-Glo, a luminescent cell viability assay kit based on ATP, was used to determine mammalian cytotoxicity. Compared to MTT's need to transform itself via metabolic activation, the CellTiter-Glo reagent generates a luciferase-based signal proportional to the amount of ATP present. This assay was used as it is unknown if the stapled peptides have any cross-reactivity with metabolic enzymes due to metabolic inhibition or other effects.

Based on the data in **Fig. 3.7**, cell viability appears to be similar among the peptides compared to both the vehicle and unstapled peptides in fibroblasts. The current results show

promise as the peptides only begin to display cytotoxic effects above micromolar concentrations. These compounds appear to be non-toxic to WS1 cells over a concentration range peaking at 10 μM. At this time, the cell viability assay requires further refinement.

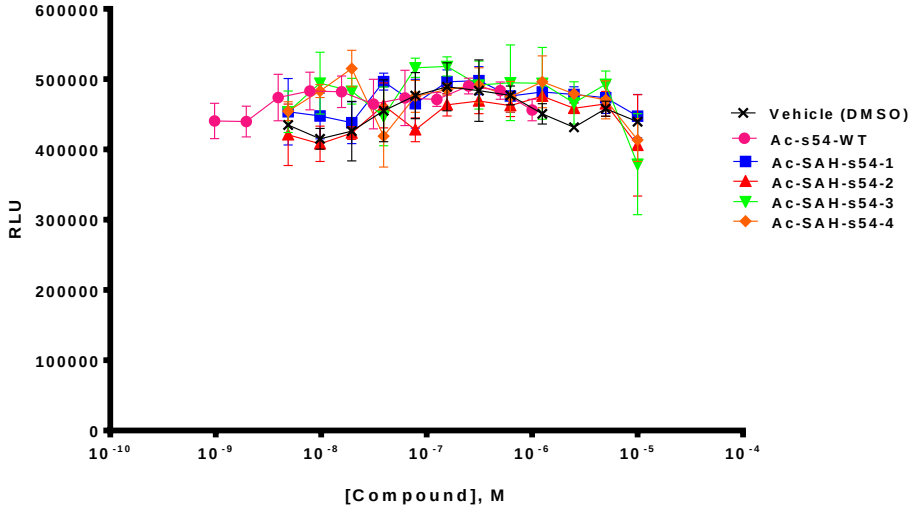

Figure 3.7. Relative luminescence units (RLU) of WS1 cells after incubation with peptide at varying concentrations for 24 hours in Opti-MEM medium. Luminescence readings were taken 40 minutes after introduction of the CellTiter-Glo ATP-detection reagent. Black represents the DMSO vehicle control, pink represents the wild-type unstapled peptide, blue represents σ^{54}-1, red represents σ^{54}-2, green represents σ^{54}-3, and orange represents σ^{54}-4. Staurosporin treatment under identical conditions produced a mean RLU value of 1.42 x 10^3 (n = 3) (not shown). Untreated control wells consisted of cells in Opti-MEM with no peptide treatment, producing a mean value of 3.77 x 10^5 (n = 30). Error bars = SD, n = 3.

Although the staurosporin-treated cells produce a significantly lower RLU (1.42 x 10^3), serial dilutions of staurosporin demonstrating gradual cell death must be conducted to ensure that the assay was performed with a control following the same treatment as the peptides. This would establish the range in which cell death should be seen. Other cell lines relevant to the clinic such as epithelial, intestinal cells, and kidney cells should be tested.

Compared to the MIC values, it appears that the peptides will induce cell death selectively against bacteria more than mammalian cells. Further characterization experiments are possible as there is little danger at relevant concentrations under study.

3.2.2 Permeability Assays

3.2.2.1 Flow Cytometry

Flow cytometry was used to gain a high-throughput perspective on the effectiveness of each stapled peptide in a large population of bacteria. By making use of its individual event detection, it is possible to determine the percentage of cells that take up the peptide. Each peptide under investigation through flow cytometry was tagged with FITC, whose excitation is 488 nm and emission is 525 ± 20 nm. This was detected using the FL1 channel. All the work discussed was done on a Beckman Coulter Gallios Flow Cytometer. For both *E. coli* and *P. aeruginosa*, the same protocol was used due to their similar size and Gram negative membrane cell typing.

To develop the protocol, BW25113 *E. coli* cells were grown overnight. The log phase was reactivated to remove 5.0 x 10^7 cells. The correct voltage was initially determined to locate the proper method to displaying the cells on the flow cytometer's cell plots. This would show the cell profile of the *E. coli* cells in phosphate buffer saline (PBS) on the Gallios's submicron setting for bacterial detection. A sample of cells with the vehicle, 0.4% v/v DMSO, was examined to determine the fluorescent background noise of the species. Cells were incubated with 4 μM peptide for 1h at 37°C for 1h. This concentration was used as it is less than the MIC value for each peptide. Trypan blue (0.4% w/v) was added to quench extracellular fluorescence in dead cells and the cell surface. It was seen that the peptides do not demonstrate a strong displacement in FL1 shift, demonstrating that the peptides are not entering the cells at appreciable values. However, there is modest levels of shifting in some peptide samples, a phenomenon that has not been reported. The protocol required further refinement to determine the best conditions for peptide uptake.

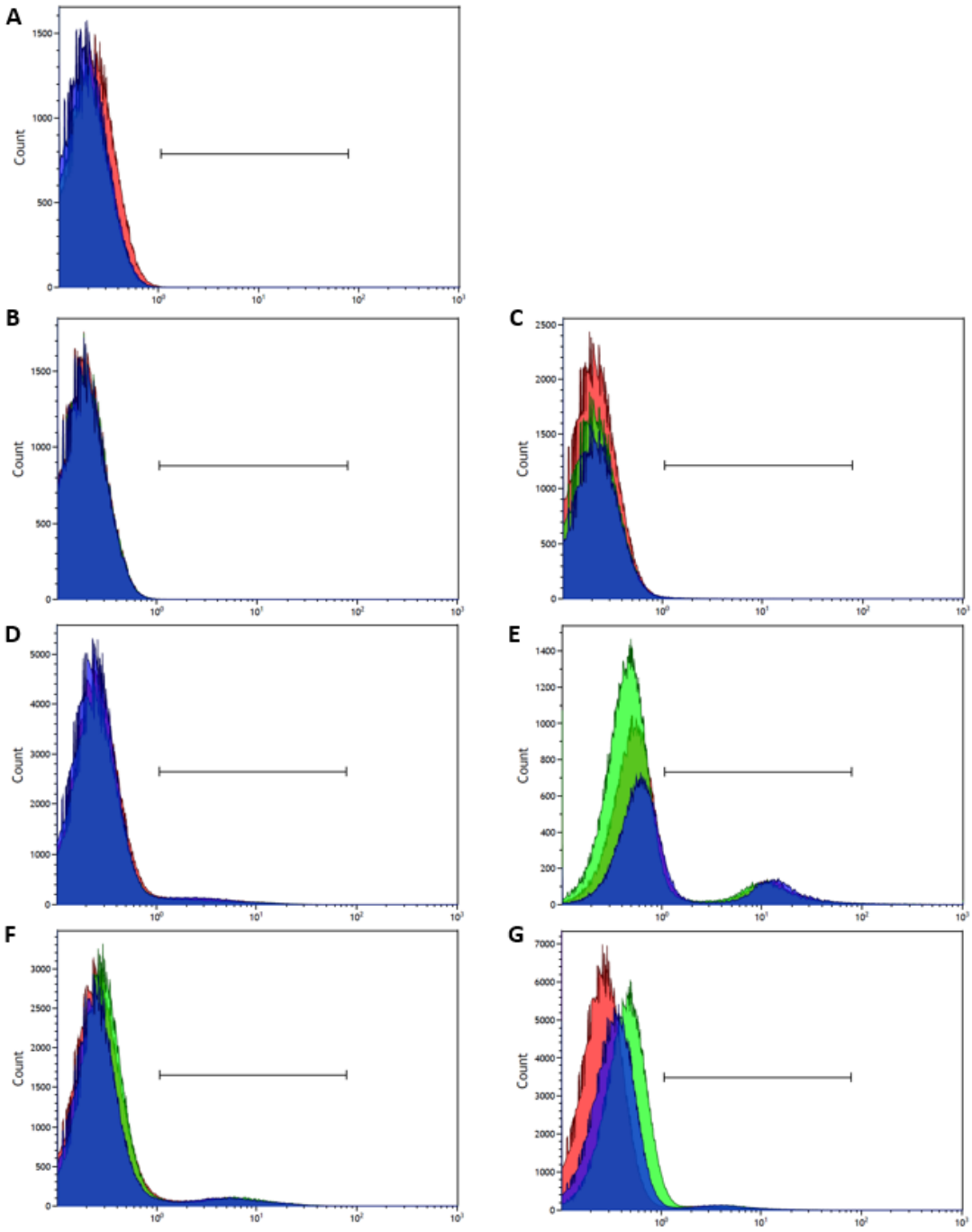

Figure 3.8. Initial flow cytometry testing of *E. coli* strain BW25113 with peptides with a heating incubation only for **A)** Cells alone, **B)** 0.4% DMSO vehicle, **C)** Wild type unstapled σ^{54}, **D)** peptide analog 1, **E)** peptide analog 2, **F)** peptide analog 3, and **G)** peptide analog 4. The red, green, and blue all represent different trials with the same conditions. Approximately 200 000 events were collected for each sample (n =3).

In **Fig. 3.8**, the gate shows 0.01% background based on cells without treatment. The gate range was chosen due to a 99.99 percentile of the population being below this gate threshold in the untreated control. As shown above in **Fig. 3.8A-B**, both cells alone and the DMSO vehicle give virtually identical signals with DMSO with a 0.01% within the gate. With the wild type in **Fig. 3.8C**, 0.2 ± 0.1% of cells were detected in the gate. This could mean that the unstapled peptide does penetrate cells to a degree. Peptides 1, 3, and 4 had low penetration percentages with 4.1 ± 0.3%, 6.1 ± 0.4%, and 3.6 + 1.3%. However, with Peptide 2, it is shown to have two populations with the second having 18.7 ± 6.4%. Although one population took up the peptide more compared to the other, it appears that the bacteria uptake the peptide marginally in the whole population. From this data set, it is difficult to tell if the peptide penetrates two separate populations or if it penetrates all cells at varying amounts. In order to understand this bimodal distribution in **Fig. 3.8E** and marginally in **Fig. 3.8F-G**, the protocol was further developed.

The cell count was raised to 1.0×10^8 cells to determine if a higher cells:peptide ratio provided any differences. This was done to evaluate whether the compound was not entering cells well, as observed in **Fig. 3.8D-G**, or if there was a problem with the initial experimental conditions.

Each peptide widely penetrated for peptides 1, 3, and 4 whereas σ^{54}-2 stayed the relatively uniform (**Fig. 3.9A**). Interestingly, if peptide 1 is compared with the DMSO vehicle treatment, it appears to have a slight but full shift whereas peptides 2 and 3 display the same bimodal pattern as before. Peptide 4 appears to be conferring a trimodal profile. Upon repetition in triplicate (**Fig. 3.9B**), it was shown that this particular protocol was not reproducible with accuracy, as indicated by the error bars. However, less than 20% of cells

were penetrated regardless of the peptide. This was an improvement compared to initial experiments, indicating that an increase in cell count may allow the peptides to be absorbed more easily.

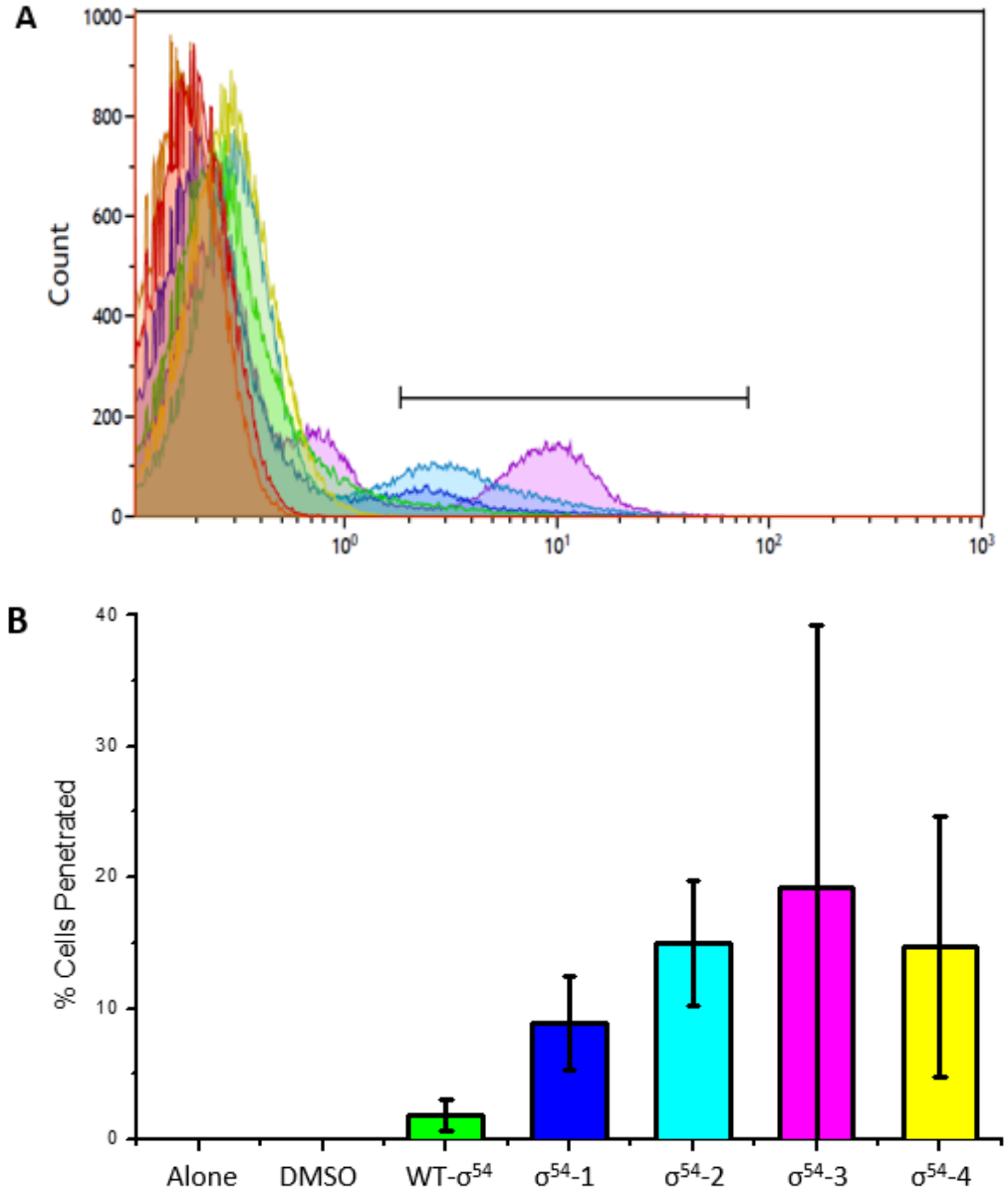

Figure 3.9. Flow cytometry with a higher number of cells. **A)** Representative histogram depiction of flow cytometry results for 1.0 x 10^8 for 4 μM FITC-tagged stapled peptides in 0.4% DMSO. The gating was changed to satisfy the 99.99 percentile requirement of the controls. Red is cells alone, orange is DMSO vehicle treated, yellow is the unstapled peptide, green is peptide 1, light blue is peptide 2, navy blue is peptide 3, and purple is peptide 4. Cells were quenched with 0.4% Trypan Blue and 100 000 events were collected for analysis. **B)** Percent of cells with the gate with all treatments (Error bars = SD, n = 3).

Next, both the incubation time and temperature were assessed to determine the proper conditions for cell entry. It was hypothesized that a longer incubation time would increase the permeability of the cells. The cells were examined at room temperature (22°C), 37°C, and 37°C with a 4°C incubation when pelleted. This ice incubation would serve to limit dead cells, cell surface signaling, and peptide efflux. The incubation-ice method mirrors various fixation protocols; however it lacks the fixative agent to keep membranes as natural as possible. This process is similar to the histological staining of various antibodies as they also require an icing period to eliminate background effects.

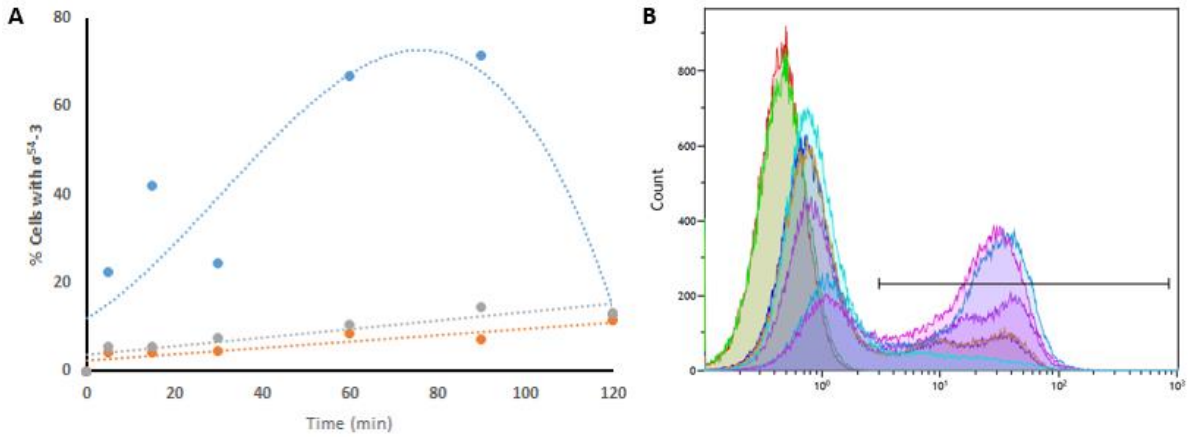

Figure 3.10. Flow cytometry results of time course and temperature assessment with 100 000 collected events from 1 x 10^8 cells (n =1). **A)** Time course trial and temperature assessment for flow cytometry of BW25113 cells with 4 µM FITC-tagged σ^{54}-3 in 0.4% DMSO. Orange represents room temperature uptake, gray represents uptake at 37°C, blue represents uptake at 37°C and followed by 4°C ice treatment. 100 000 events were collected. **B)** Flow cytometry histogram analysis of time course data. Red is cells alone, green for 0.4% DMSO, navy blue for 5 min, purple for 15 min, orange for 30 min, turquoise for 60 min, magenta for 90 min, and light blue for 120 min.

Both the room temperature and 37°C uptake appear to be similar. From this time course (**Fig. 3.10A**), it seems that 90 minutes with a 30 minute incubation appears to confer the best amount of cell permeability at 71.5%. As seen in the flow cytometry profiles, the cells are all shifted relative to non-fluorescent controls. Certain populations shift greater than others, with a higher number of cells retaining the stapled peptides. The bimodal peak is still

present at 15 and 30 min but disappears at later time points (**Fig. 3.10B**). From this experiment, the twin-peak profile may be attributed to cells that have a specific permeability mechanism that retains the peptides better than others or, as hypothesized, that the metabolic ability of the cells varies in large proportions and this plays a role in the peptide's absorption.

A trimodal shape is still present at 15 min and 30 min; this problem has not been solved yet. However, at time points above 30 min, the bimodal profile is present instead. This would lend to the theory that an in-between state exists at the early stages of peptide uptake, exhibiting a third population, before conforming to the staple bimodal profile. However, it may be that the fluorophore adopts an intermediary state as the middle peak disappears; there may a change in its intensity prior to its stabilization past 30 min.

To determine the mode of transportation, 10 mM sodium azide was used to inactivate proton ATPases of bacteria.[20] By using a chemical method to knockdown active transport, all peptide uptake would be attributed to passive diffusion methods such as diffusion or facilitated diffusion. Any general extracellular-directed ATP-linked pumps would be disabled so the peptide would be retained more easily. By using both types of treatments, it's possible to determine whether the mode of uptake of stapled peptides is through active or passive transport. Furthermore, with passive transport, the entry of the peptide should be faster than active due to the lack of metabolic means necessary to promote cell entry.

When treated with 10 mM NaN_3, cells undergoing the same heating/icing protocol appeared to show a percentage of cells similar to that of the time course experiment. As seen in **Fig. 3.11A**, stapled peptide 2 appears to penetrate cells the most at 89.5 ± 3.0% with

peptide 3 in second with 83.2 ± 3.9% and the others less than 70% each. Furthermore, the peptides themselves still exhibit either the bimodal or trimodal distribution (data not shown).

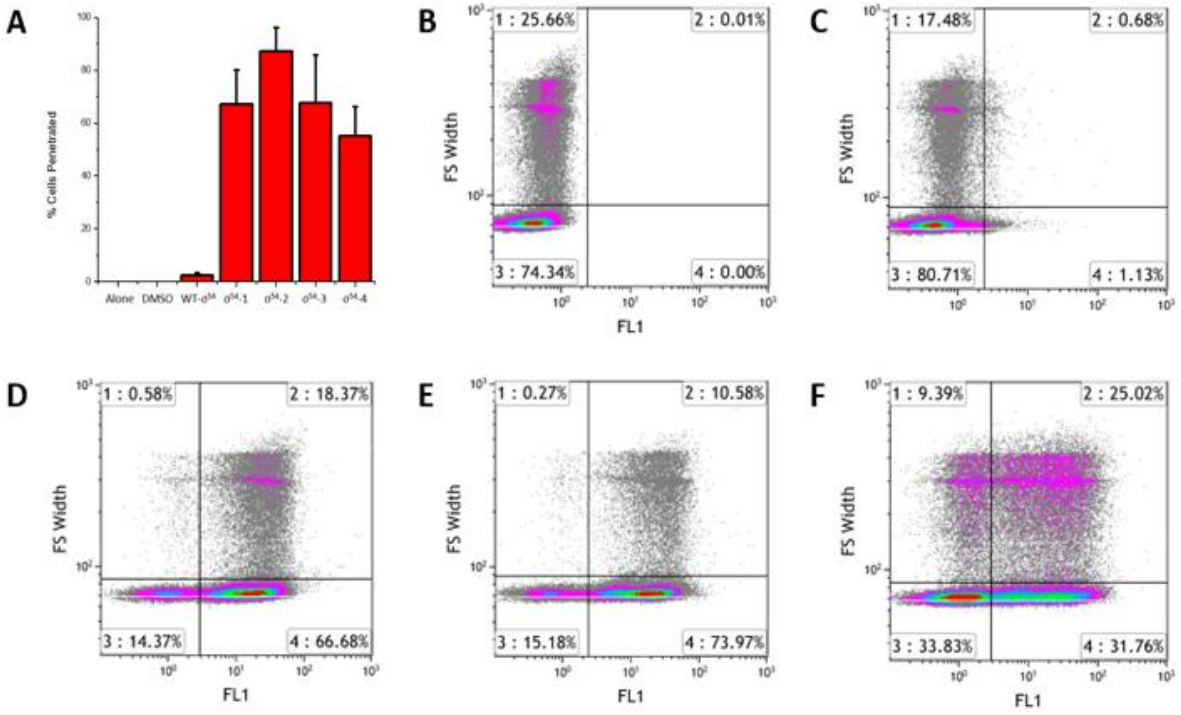

Figure 3.11. **A)** Flow cytometry histogram analysis of BW25113 cells treated with 10 mM sodium azide with 4 μM FITC-tagged σ^{54} peptide analogs in 0.4% DMSO. Representative density plots for the following treatments: **B)** DMSO vehicle, **C)** WT-σ^{54} unstapled peptide, **D)** σ^{54}-2, **E)** σ^{54}-3, and **F)** σ^{54}-4.

To understand this distribution, the cell density plots were examined. In **Fig. 3.11B**, this shows the general distribution of cells within the four quadrants of the gate setup. The majority of cells are in quadrant 3, which show the *E. coli* in their unicellular form. Quadrant 1 shows bacteria undergoing cell division. This is due to the forward scatter detecting a longer width but similar length of each cell compared. **Fig. 3.11C** shows moderate amounts of unstapled peptide penetrating bacteria due to small amounts of fluorescence within quadrants 2 and 4. With stapled peptide 2, **Fig. 3.11D** shows two fairly distinct populations within their groups. However, peptides 3 and 4 in **Fig. 3.11E-F** show the presence of the

third population lying on the gate division between quadrants 3 and 4. Of note, cells undergoing cell division uptake the peptides as well as their unicellular counterparts.

At this time, it is difficult to determine what processes are causing this third population. Upon further investigation, it appears to be a smaller size of cells that emit green fluorescence (data not shown). The side scatter of these cells appears to line up with the viable cells absorbing the peptides (**Fig. 3.11F**). Upon examination of the forward scatter (data not shown), it may be possible that a portion of that cell population is undergoing cell death processes. This change in fluorescence ability of the FITC-tagged peptides maybe due to a number of factors such as cell death post treatment, an intermediate between saturation and unsaturation of cells, or a change in the electronic environment of the fluorophore.

Once the protocol was finalized, it was tested again with two bacterial cell lines: *E. coli* BW25113 line and *P. aeruginosa* PA01 line. *Pseudomonas* and *Escherichia* have similar rod shapes while both being Gram negative so no conditions required modification.

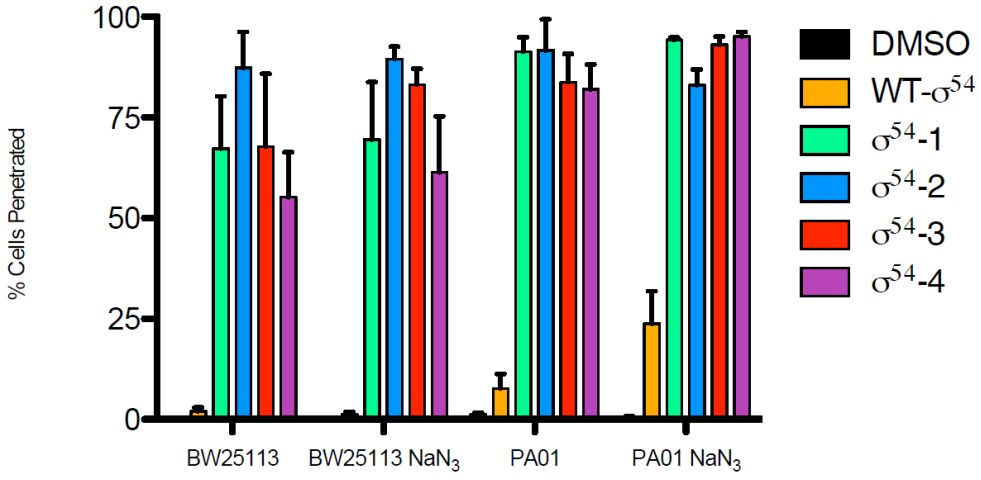

Figure 3.12. Flow cytometry analysis of BW25113 and PA01 cells in 0.4% DMSO and 4 μM FITC-tagged stapled α-helical peptides. Column groups 2 and 4 were treated with 10 mM NaN_3 in ddH_2O (n = 3, error bars = SD). Two-way ANOVA statistical analysis was conducted with the Bonferroni post-tests to determine significance in all peptide penetration compared to the DMSO vehicle control.

As depicted in **Fig. 3.12** in both *E. coli* and *P. aeruginosa* species of Gram negative bacteria, all four peptide analogs are capable of penetration. Compared to the vehicle control, the wild type peptide, the sequence in which no staple is present, shows minor penetration in PA01 *P. aeruginosa* (p-value < 0.05) and insignificant levels of penetration in BW25113 *E. coli* (p-value > 0.05). With each peptide, there is a penetration of at least 50% of cell in each peptide sample (p-value < 0.001). When comparing both species with or without sodium azide treatment, there appears to be a global increase in cellular uptake, especially with PA01. It is possible that the peptides are being excreted by the cells through pumps or other ATP-dependent means. Overall, there is clear statistically significant evidence that stapled peptides can cross membranes of cells.

In relation to staple placement, σ^{54}-4 exhibits the worst penetration. This is likely due to its lowered positive charge based on its knocked out arginine (+3 charge overall). This would suggest charge dependent cellular uptake along with α-helicity to uptake the peptides as the unstapled peptide (+4 charge) was not readily taken up by *E. coli* in appreciable amounts. σ^{54}-1 has a staple placed towards the C-terminus end; its penetration is low in *E. coli* and high in *P. aeruginosa*. It may be possible that the lower staple may confer a level of selectivity towards different species. Peptides 2 and 3 display the highest penetration. This data falls in line with the tendency of increased α-helicity in staples placed near the N-terminal region.

3.2.2.2 Confocal Microscopy

Confocal microscopy was used to assess the bacteria in a low-throughput method. By making use of fluorescence microscopy techniques, it is possible to visualize the localization and dynamics of the peptides in living cells.[21] In order to examine the effects of stapled peptides *in vivo*, the Z stack images were collected by deconvolution fluorescence microscopy to observe the subcellular localization of the FITC-tagged stapled peptides in *E. coli*. Upon visualization, if the peptide has been taken up by the cells, a stronger intensity in the green channel will be observed as the FITC will fluoresce within the cell membrane stained with FM4-64.

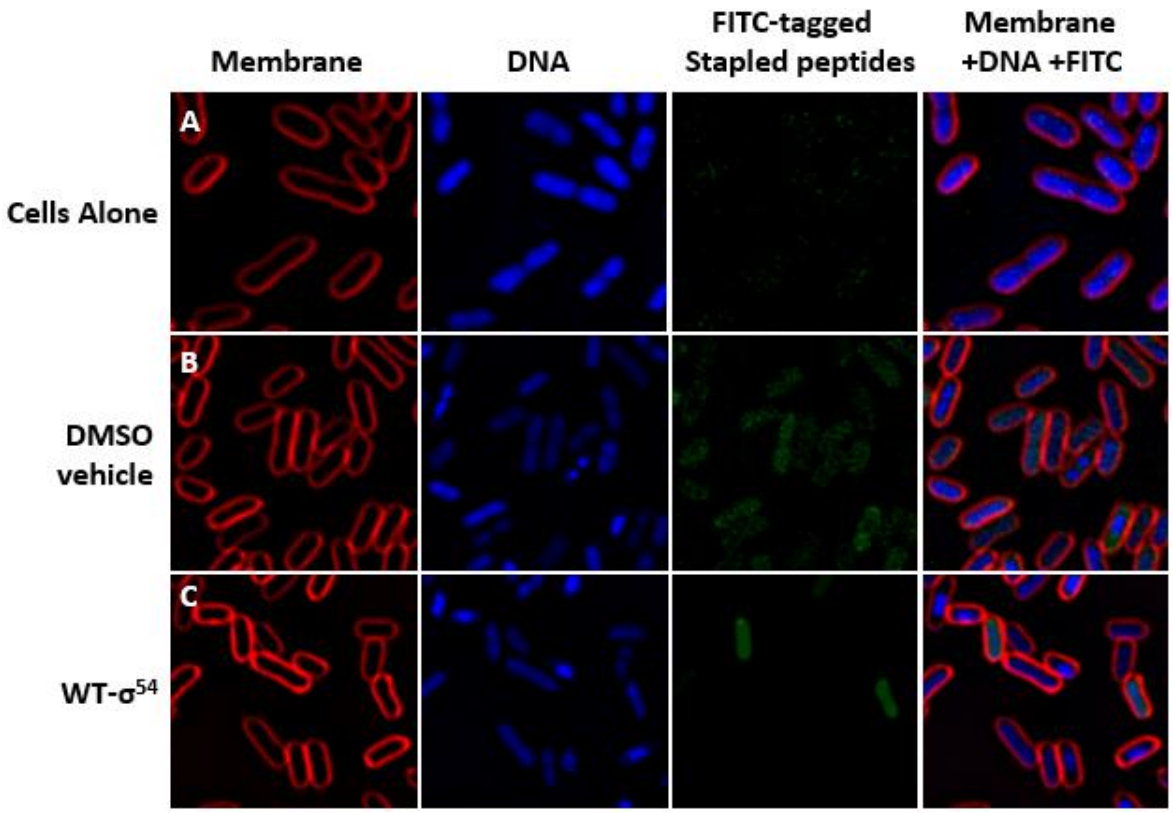

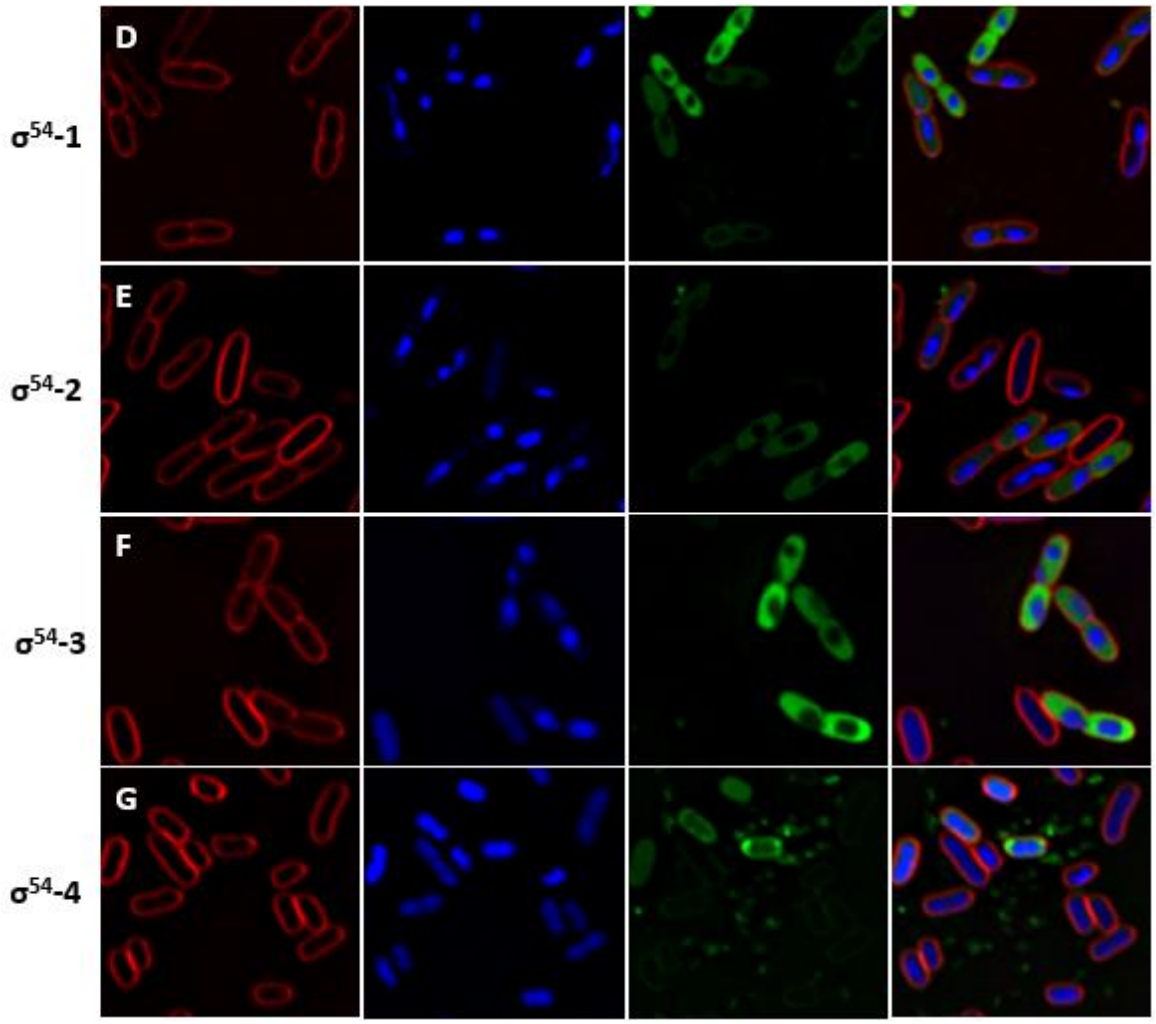

Figure 3.13. Confocal microscopy of BW25113 cells treated with 4 μM FITC-tagged stapled α-helical peptide. Cell membranes are stained with FM4-64 in red (1 μg/mL) and DNA is stained with DAPI (2 μg/mL). Bacteria were treated with peptide for 1 hour at 37°C with **A)** nothing, **B)** 0.4% DMSO, **C)** WT unstapled σ^{54} peptide, **D)** σ^{54}-1, **E)** σ^{54}-2, **F)** σ^{54}-3, **G)** σ^{54}-4.

Upon visualization of the cells, this data confirms and supports the flow cytometry data (**Fig. 3.12**) demonstrating that the peptides are entering cells. Various new characteristics are observed using this method. Firstly, in non-stressed cells, the DNA loosely occupies the entire cell as seen in **Fig. 3.13A-B**. As a result, it will undergo normal metabolic processes. In bacteria with any peptide treatment, the peptides induce the DNA aggregation in the central area of the cell. This could be the effect of the peptide binding to the DNA and

a response of the cell based on the stress of the peptide. However, it may also be that the significant number of peptides within the molecule causes the DNA and peptide to aggregate into an insoluble complex. Furthermore, in **Fig. 3.13G**, the treatment demonstrates that cells undergoing cell death throughout the procedure release the peptide into the environment, allowing it to be readily absorbed by other cells. In **Fig. 3.13D-F**, in this small sample, it appears that parent cells currently undergoing cell division are able to retain all stapled peptides compared to parent cells in their growth phase. It is interesting to note that certain cells display a stronger fluorescence intensity compared to others while being examined within the same sample. This may be a possible explanation for the previous data displaying the trimodal profile (**Fig. 3.9A, 3.10B, 3.11F**). As there is no green or yellow overlap on top of the FM4-64 stained cell membranes, it is likely that the peptide is not integrating itself with within the cell membrane, thus remaining in the cytoplasm.

The reasoning behind the trimodal population remains speculative. It is possible that the cell death is occurring more in cells in their growth phase as opposed to their division phase, thus creating a new population. Another possibility is that the dividing cells are able to retain more peptide without cell death. However, the bimodal population seems to be cells that simply did not uptake the peptide during the incubation. This aligns with previous hypotheses that the concentration used was not sufficient to penetrate all cells at the maximum detectable intensity based on the flow cytometer. Overall, the peptides are properly absorbed by the Gram negative bacteria while causing phenotypic changes to their DNA localization.

3.2.3 Evaluation of the peptide-DNA interaction

3.2.3.1 Electrophoretic Mobility Shift Assay

The initial work to determine the peptide's binding ability was conducted through EMSA. This is a gel electrophoresis technique in which DNA and its bound protein or peptide are separated by electrophoresis through a polyacrylamide gel to observe a change in mass, with the DNA-peptide complex running a shorter distance due to an increased molecular weight.[22,23] This assay was initially used to determine that the complex is forming.

Varying conditions of both peptide concentration and agarose concentration (8% to 20% gradient) were tested. IRDye$_{700}$ oligomers of the glnA -24 sequence were solvated in 1x TE buffer (20 pmol/μL) and annealed together. This experiment was unsuccessful as the results indicated no change in both vehicle and unstapled peptide controls (data not shown). It is possible that the peptide was bound but the slight change in molecular weight (1.3 kDa) is difficult to visualize.

His$_6$-σ^{54}, a construct obtained from the Wemmer lab at UC Berkeley, was expressed in pET28b in *Klebsiella pneumoniae* to explore the initial binding of the RpoN box to DNA and use as a control. The goal was to produce a dose-response curve that shows the displacement of the DNA band in the EMSA. With the addition of peptide, a similar dose-response curve was expected. However, the problem with this system is that the peptide itself will still show little displacement. If the peptide is truly capable of binding to DNA stronger than the native cofactor, the protein will be displaced.

The designed EMSA experiment seeks to use a constant concentration of σ^{54} protein and dose the σ^{54}-DNA complex with increasing concentrations of stapled peptide to remove

the complex in a dose-dependent manner. This will demonstrate that the binding affinity of the peptide is comparable to the σ^{54} protein. On the gel, the cofactor-DNA complex band would disappear and the peptide-complex should appear if the binding of the peptide occupies the same area on the DNA. Furthermore, on a longer strand of DNA, the peptide will demonstrate specificity due to the σ^{54} protein binding at only the -24 site of the oligomer.

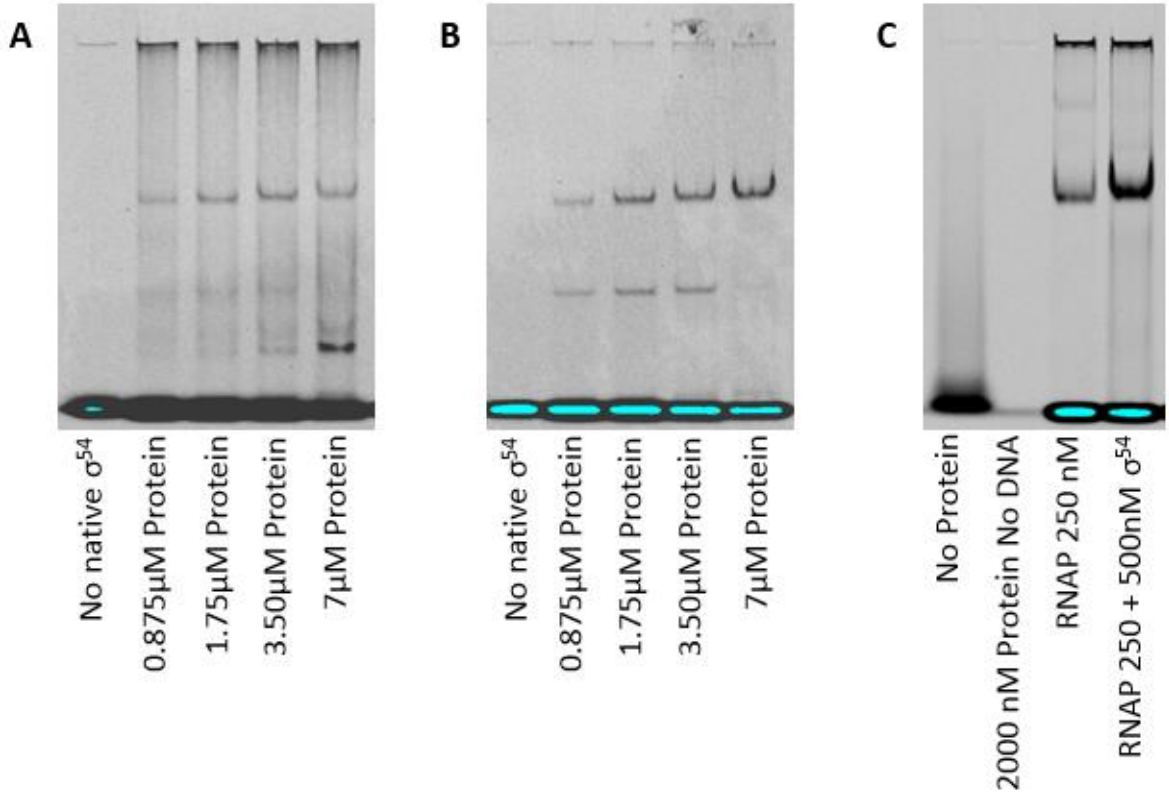

Figure 3.14. Optimization of electrophoretic mobility shift assays of σ^{54} protein and oligomers by examining the $IRDye_{700}$ DNA displacement. **A)** WT-σ^{54} co-factor bound to 2 nM 30-mer of -24 glnA binding site. **B)** WT-σ^{54} co-factor bound to 2 nM GG24TT mutation. **C)** Holoenzyme complex of RNAP-σ^{54} cofactor with 2.5 nM WT-DNA 88-mer.

In **Fig. 3.14A-B**, the full σ^{54} protein is shown to bind specifically to the 30-mer as it lacks binding to the double mutant. As a result, peptides can be compared to this control to perform a dose-response EMSA, based on observation of a change in the molecular weight of the complex compared to DNA alone. Since all these parameters have been monitored, it is possible to test the displacement EMSA assay with the stapled peptides. However, with

the addition of RNAP in **Fig. 3.14C**, it appears that the displacement itself, although present, provides little change in the band. Furthermore, the amount of aggregate in the top of the well with RNAP appears to be stronger. The concentration read by the gel may not be proportional to the amount within the sample if this aggregation effect proves true.

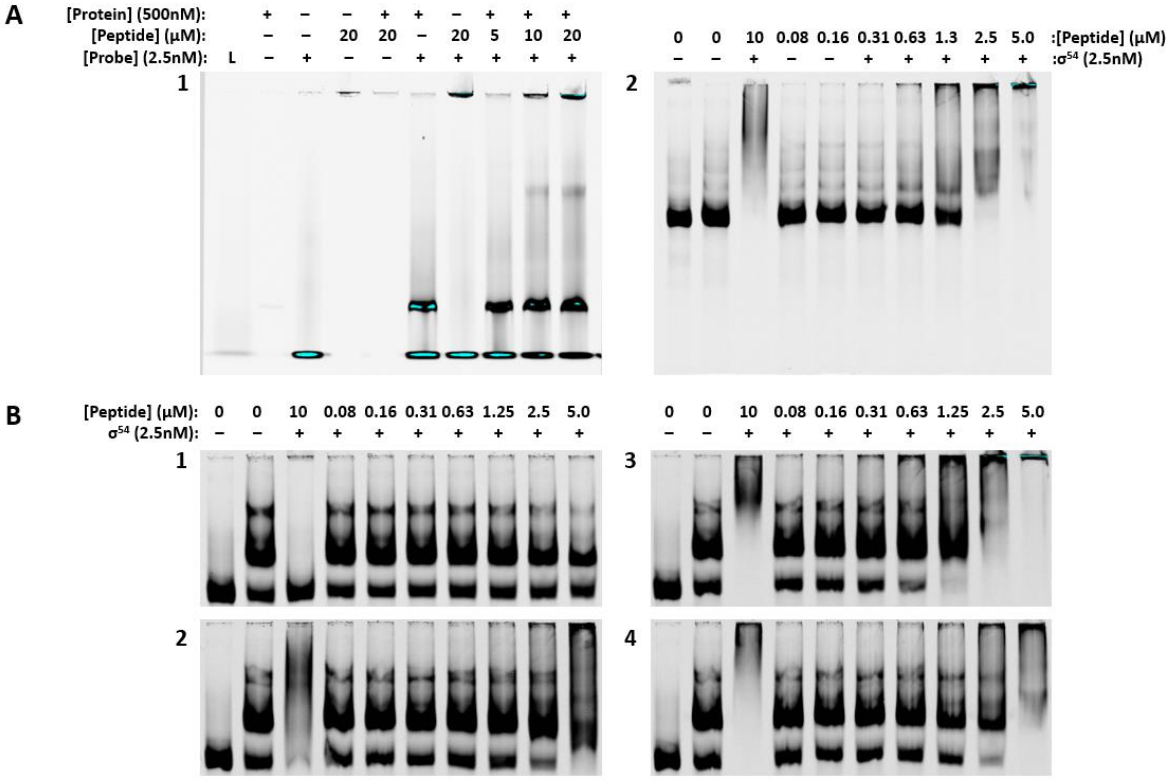

Figure 3.15. Electrophoretic mobility shift assays of peptides using the IRDye$_{700}$ oligomers. **A) 1.** σ^{54}-DNA complex competition assay with increasing acetylated stapled peptide concentrations. **2.** 88-mer GG-24TT with σ^{54}-2. **B)** Competition assay with increasing **1)** WT unstapled, **2)** σ^{54}-1, **3)** σ^{54}-2, and **4)** σ^{54}-4. Peptide 3 was not shown due to its similarity to σ^{54}-2.

With the addition of the 88-mer, σ^{54} protein, and acetylated stapled peptide, there appears to be little effect in the displacement of the DNA- σ^{54} complex. In **Fig. 3.15A1**, the right gel shows the IRDye$_{700}$-tagged 88-mer demonstrate little displacement or decrease in signaling with the addition of acetylated stapled peptide with complexing with 500 nM σ^{54} protein and 2.5 nM DNA probe. To solve this problem, the concentration of peptide was

optimized to fully displace the unbound oligomers at the end of the gel; this will minimize the amount of σ^{54} protein within the mixture. **Fig. 3.15B1-4** shows that the peptide displacement assay works, as evidenced by the change in the bottom oligomer's displacement position (seen in the first lane from the left of each gel). The second lane shows the profile displayed with σ^{54} protein and lanes 3 to 10 with varying concentrations to titrate out the complex. In this experiment, the binding affinities would rank as follows: WT < 1 < 4 < 3 ≈ 2.

Unfortunately, in **Fig. 3.15A2**, when an 88-mer with the GG-24TT mutation was incubated with σ^{54}-2, a displacement was observed. However, when compared with **Fig. 3.15B3**, there appears to be a concentration window in which mutations do not bind. This EMSA assay does display the peptide shifting; however, it is not the ideal method to showcase specificity. As the peptides were removed from the bottom band, they remained at the top of the well in the aggregate of peptide-cofactor-DNA mixture, seemingly adopting an insoluble complex. Although this gel displays binding affinities for the overall complex displacement, it does not display single molecule binding affinity between the stapled peptides and oligomer. We explored other methods of examining specific binding.

3.2.3.2 Anisotropy

The binding ability of the RpoN σ54 stapled peptides with the -24 site of glnA in *A. aeolicus* was thoroughly examined with the use of fluorescence anisotropy. This was a necessary step in establishing that the peptide is able to target its intended DNA sequence with high affinity. Fluorescence anisotropy is a powerful tool used to determine the binding affinity of biomolecular interactions at concentrations as low nanomolar concentrations.[24,25]

The emission polarization and the molecular rotational diffusion are affected by the binding strength of the species under investigation.[26] In this study, the change in anisotropy of the FITC-tagged σ^{54} stapled α-helical peptides was evaluated against varying concentrations of the double stranded -24 glnA sequence to determine the dissociation constant (K_D) of the DNA-peptide interaction. Without binding, the FITC-tagged peptide is able to tumble freely with a high degree of freedom, as seem by the lower saturation region. Upon binding, the movement of the fluorophore is hindered and therefore a change in its anisotropy measurement is detected. To determine the K_D itself, the inflection point, the point in the middle of the two states, is taken as the binding constant. The DNA segment tested was 30 base pairs in length with the -24 site situated in the middle of the sequence.

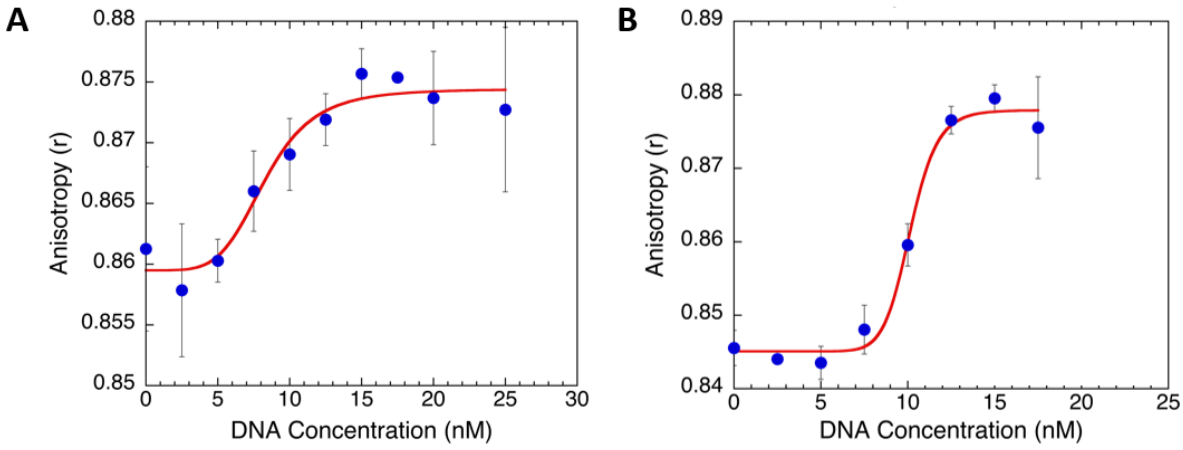

Figure 3.16. Anisotropy of FITC-tagged stapled α-helical peptides for **A)** σ^{54}-2 and **B)** σ^{54}-4 bound to a 30 base pair DNA sequence modeled against the -24 region of *A. aeolicus*. 5 nM of peptide was used at ambient temperature. The line was modeled using a semi-log Hill equation. (Error = SD, n = 3)

The saturation curve, the region of hindered fluorophore movement, does show full saturation past 15 nM for both peptides in **Fig. 3.16**. Peptide 2 exhibits a K_D of 8.3 nM and peptide 4 for 10.1 nM. This is promising as the native K_D based on the Wemmer lab's studies is 1 order of magnitude weaker than that of the stapled peptides.

3.2.3.3 Fluorescence Lifetime Imaging Microscopy

DNA is principally composed of a various sequences of four base pairs; If the peptide is shown to bind to glnA -24 promoter-like sites, it must be established that the peptide will bind based on its innate abilities. It is important to establish that the stapled peptide is binding to its double stranded promoter sequence of interest. With a limited supply of the peptide, a nanoparticle-based detection assay was devised to prove specificity with high resolution (**Fig. 3.17**). Nanoparticles have been shown to functionalize with thiolated DNA.[27,28] By making use of DNA-functionalized gold nanoparticles (AuNP), we intend to use Förster resonance energy transfer (FRET) to determine specific binding. FRET is a widely used technique in detecting the specific binding of an engineered pair of biomolecules.[29,30] In this experimental setup, the Cy5-tagged dsDNA acceptor was immobilized on a thin film of AuNPs and FITC-tagged peptides were applied to the nanoparticles to bind to the DNA. The purpose of using AuNPs is to enhance the signal of the single molecular fluorescence events[31] while immobilizing the DNA in a solid phase.

Fluorescence lifetime imaging microscopy (FLIM) was used to examine the lifetime of both fluorophores of the FRET pair: FITC and Cy5. To provide evidence of FRET, it is essential to measure the proximity of the protein and DNA with a resolution equal to the FRET distance of the two fluorophores: approximately 1-10 nm.[32] FRET innately changes the lifetime of the donor molecule due to its transfer in energy. Combined with an *in vitro* imaging technique, each pixel in the image can be measured to generate multiple data points without significant effects from relative localized concentrations or diffusion rates.[32] With this FLIM-FRET approach, it is possible to visualize the direct interaction between one molecule of Cy5-tagged dsDNA and one molecule of FITC-tagged stapled peptide.

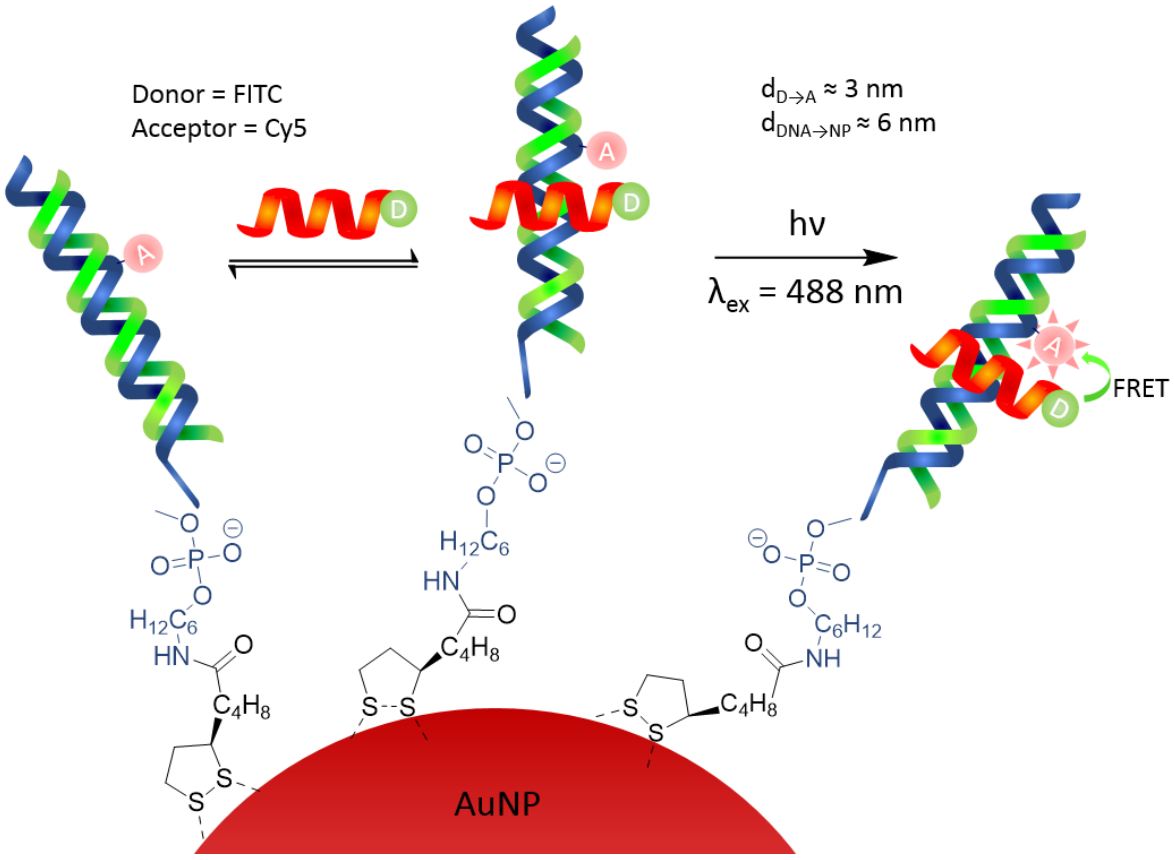

Figure 3.17. FRET nanoparticle binding assay schematic diagram. The orange peptide "D" represents the stapled peptide, and the blue and green helix "A" represents the glnA double stranded DNA.

Quantitative analysis has been used in conjunction with FRET-based techniques to detect structural and conformational changes.[33–35] In general, the donor fluorophore emits a photon within the absorption spectrum of the acceptor fluorophore. The acceptor will absorb this energy and emit its own lower energy photon due to the non-radiative loss of energy at during the energy transfer.[36] FITC was selected as the peptide donor due to its prior use in previous experiments and for its excitation and green emission at 488 nm and 520 nm respectively. Cy5 was selected as the acceptor based on its lack of 488 nm excitation and absorption within FITC's emission range while emitting a red photon after 650 nm (**Fig. 3.18**). As an overlap is present between the emission spectrum of the donor and the

absorption spectrum of the acceptor, coupled with the exclusive detection of the acceptor with the cut-off filter detector, this pair of fluorophores will function for this study.

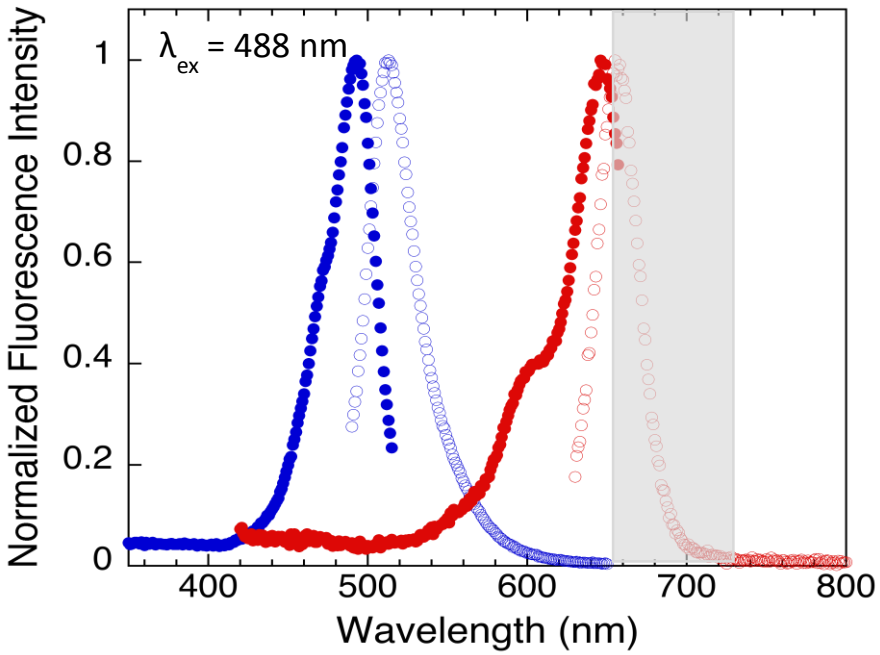

Figure 3.18. Absorption and emission spectra of FITC-tagged σ^{54} stapled peptide and Cy5-tagged dsDNA strand in aqueous solution. Blue represents the stapled peptide, red represents the dsDNA, filled represents the fluorescence excitation, and open represents the emission spectra. The gray box represents the cut-off filter used to detect the FRET emission. (n = 3)

To determine the correct placement of the Cy5 acceptor in conjunction with the FITC-tagged peptides, PyMol was used to predict the distances required for FRET to occur. As the FITC attached to the stapled peptide is attached to the N-terminus of the peptide next to a β-alanine, it was estimated that FITC is approximately two amino acids away from the start at of the amino acid sequence. This is placed at the Lys327 when comparing to the *A. aeolicus* sequence in **Fig.2**. With the distances shown in **Fig. 19**, the sites one helix turn away lie within the 1-10 nm range but the helix adjacent to the interface is pushing the limits of the FRET distance. As a result, the C-T pair upstream of the sequence was selected as it was the distance closest to the middle of the range at 3.11 nm.

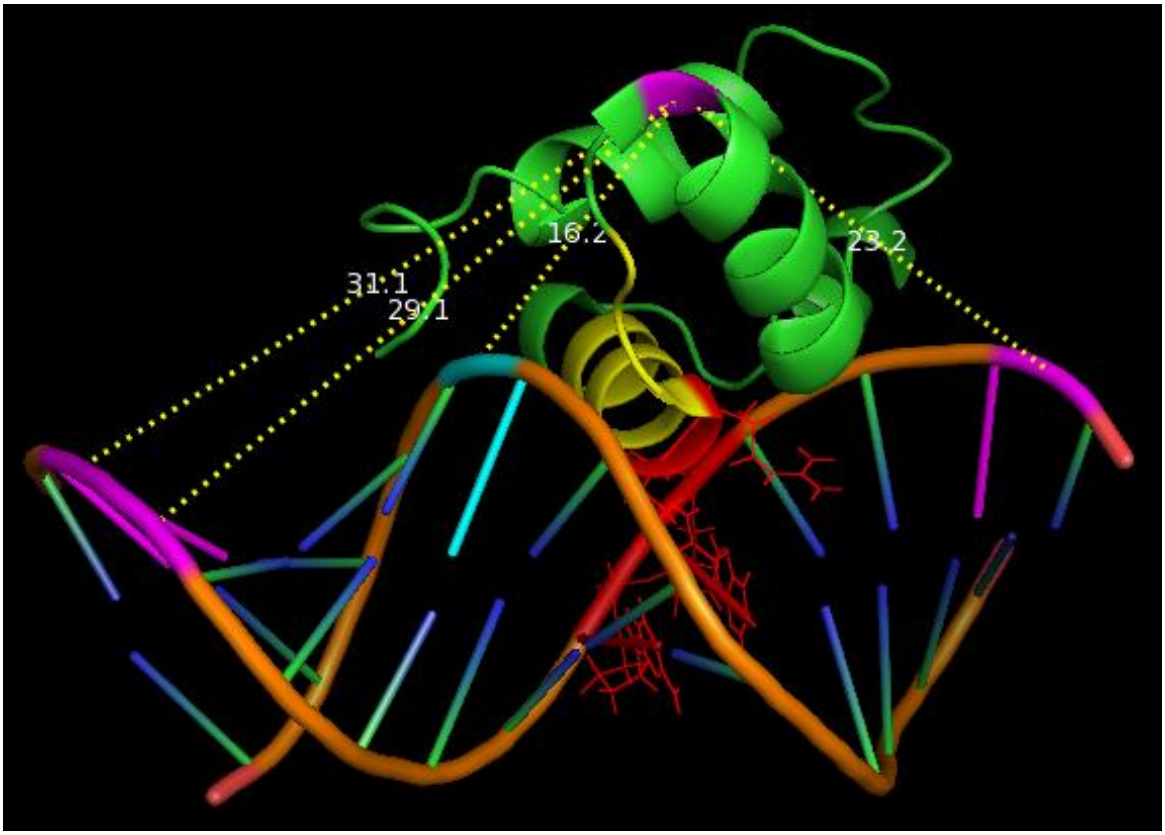

Figure 3.19. PyMol illustration of the known σ^{54}-glnA -24 site to estimate the distances between fluorophores in Angstroms. Purple represents estimated sites for placing either the donor or acceptor. On the protein, purple shows the estimated area of FITC, red shows Arg378 and Arg379 key to DNA binding, yellow shows the RpoN box, and green shows the nearest domains of σ^{54}. On the DNA, red shows the two guanines key to binding, purple shows possible areas for FRET, and the other colours are DNA base pairs within the glnA sequence.

By using a nanoparticle-based assay, we were able to confirm the specificity of the stapled peptides relative to its promoter region. The DNA sequence of 30 base pairs in length was bound to a solid phase with the following sequence: 5'-H2N-CGCC TTTAAAAGTT GG CACAGCy3 TTTC GGCG-3'. FITC-tagged peptide was added to the AuNP-glnA conjugates, with FRET only observed upon the specific binding of the DNA and peptide.

By using fluorescence lifetime imaging microscopy (FLIM) with FRET, we determined molecular binding through the assay designed in **Fig. 3.17**. FLIM-FRET microscopy has been widely used to determine binding pairs at a highly sensitive single-

molecule level.[32,37] To our knowledge, this method has not been applied to identify protein-DNA binding through nanoparticle-based methods.

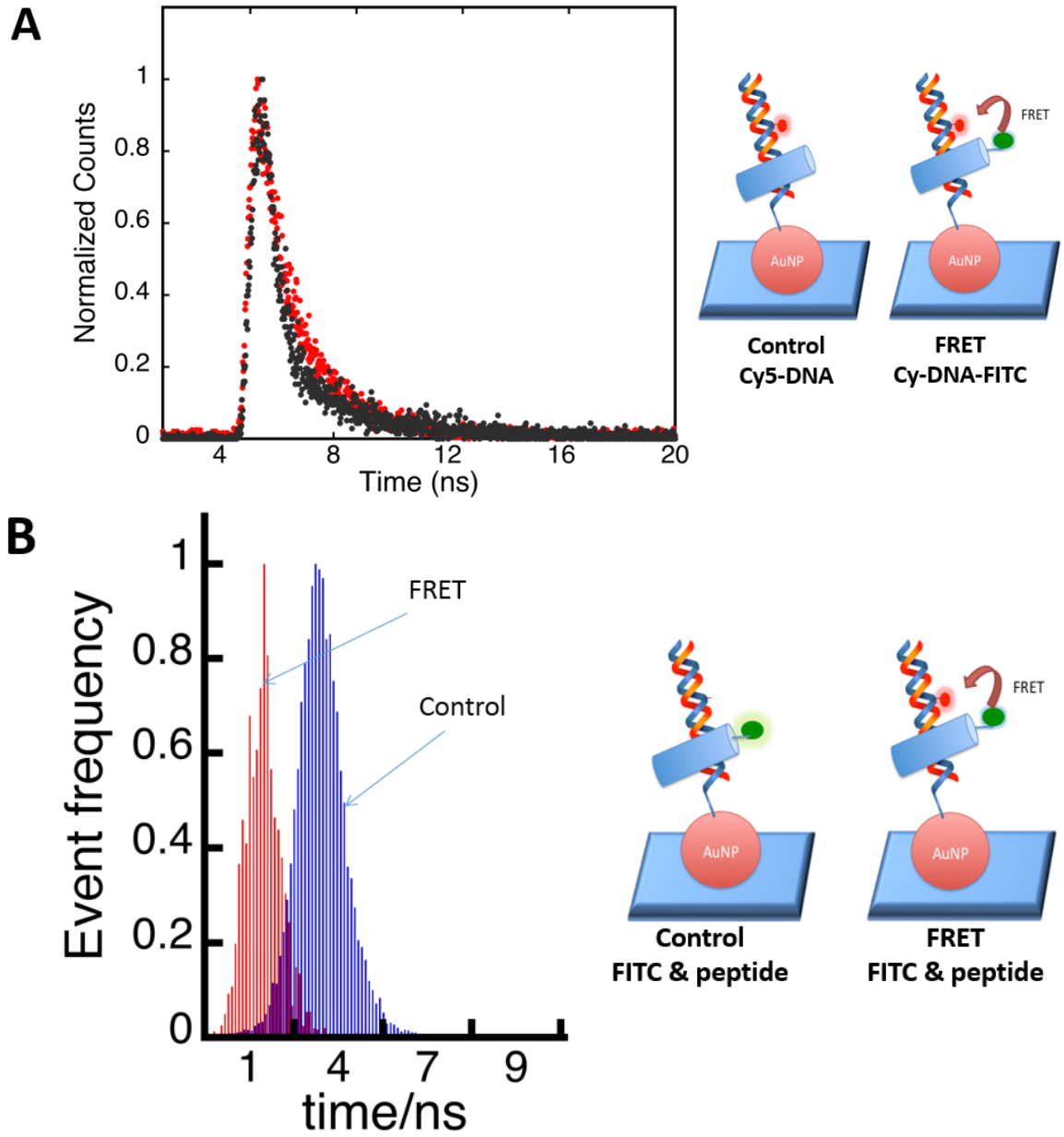

Figure 3.20. Fluorescence lifetime imaging microscopy of AuNP functionalized with DNA and incubated with 10 nM FITC-tagged σ^{54}-2 stapled peptide. **A)** Evaluation of Cy5 DNA lifetime with both FITC and non-FITC tagged peptides (690/700 bp). Red represents the lifetime of Cy5 without peptide (τ = 1.41 ns) excited at 640 nm, gray represents the lifetime of Cy5 with FITC-tagged peptide exhibiting FRET (τ = 1.33 ns) excited at 480 nm (n = 3). **B)** Evaluation of FITC peptide lifetime with AuNPs functionalized with DNA with or without Cy5 excited at 480 nm (525/50 bp). Blue represents the peptide binding to DNA without Cy5, red represents peptide binding to DNA with Cy5 exhibiting FRET (n = 3).

In **Fig. 3.20**, a signal is detected with the 488 nm excitation, 650 cut-off filter, indicating that FRET occurs due to the presence of a Cy5 signal from excitation from a high energy photon outside of its absorption range. The maxima of both FITC-tagged and non-FITC-tagged peptides are aligned in **Fig. 3.20A**. This verifies that the difference in conditions, FITC vs. acetylated peptide, has no significant effects on the lifetime of the Cy5 emission photon as their chemical environments will be similar and a profile can be established for the binding interaction. Furthermore, as the FRET experiment was excited within only FITC's absorption, it is clear that FRET is occurring as a signal was detected that matched the profile of Cy5 excitation upon binding without peptide. This presence of FRET provides a strong indication that the peptides are binding selectively to the -24 binding site at nanomolar concentrations. From this experiment, the DNA-Cy5 lifetime appears uniform in both conditions despite the switch between FITC and acetylation.

However, the presence of Cy5 only examines one fluorophore. The FITC fluorophore must be examined to determine the loss in energy of the peptide. In **Fig. 3.20B**, the lifetime of FITC has decreased. In the control, FITC's lifetime under similar chemical environment is approximately 3.4 ns whereas the FRET experiment displays a lifetime of approximately 1.3 ns. As the lifetime maximum of FITC alone has decreased, this is attributed to the non-radiative energy transfer of the FITC photon's energy by Cy5 due to its proximity. By combining the lifetime information from both fluorophores, it is clear that the FLIM experiment is successful and the FRET phenomenon observed between both fluorophores is due to the specific binding of the peptide to the DNA.

3.2.4 Phenotypic Characterization

2.2.4.1 Motility Assay

To further understand the function of the σ^{54}-modeled stapled α-helical peptides, pathogenic functions of bacteria were examined to monitor the downregulatory effects of peptide treatment. As σ^{54} is a known contributor to the regulation of bacterial motility, the motility of the bacteria was assessed. To begin, as σ^{54} is highly involved with virulence, various factors must be examined. One key factor is motility. Motility has been linked to virulence due to its links to biofilm formation,[38] delivering virulence factors,[39] bacterial adhesion,[40] and cell invasion.[41,42] As the peptides are designed to inhibit virulent activity, motility inhibition was necessary to assess.

A classical motility assay was used to determine the bacteria's ability to travel through soft agar mediuma.[43] In **Fig. 3.21**, the knockout flagella MC4100 *E. coli* strain displays a phenotype lacking significant growth away from the site of inoculation. The peptides will inhibit the swimming ability of the bacteria when a smaller diameter is observed.

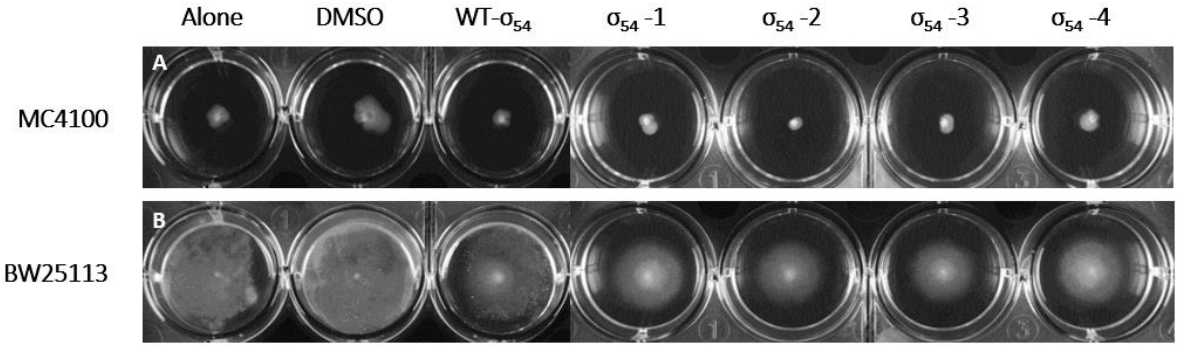

Figure 3.21. Motility assay conducted with soft LB agar with peptide concentrations of 4 μM. *E. coli* cells were incubated with various media mixed with peptide for 18h at 37°C. MC4100 cells display the knockout phenotype and BW25113 cells are used to determine motility (n = 3).

In BW25113 cells, all peptides show a degree of inhibition relative to both the vehicle and the unstapled wild-type peptide. However, it is shown that the peptides do not possess the same inhibition of motility compared to a knocked out cell line. Between peptides, σ^{54}-2 and 3 appear to have a slight increase in motility compared to the others. This corresponds with the cell penetration results as the peptide 2 and 3 penetrate more cells than 1 and 4. However, this slight decrease is not necessarily linked with the peptide penetration as other factors like cell death, cell number, and inoculation depth play a role in experimental variability. As the peptide decreases the expression of motility-related genes, the overall ability of the peptides demonstrates a decrease in flagellar mobility of the bacteria.

3.2.4.2 Biofilm Formation

If the stapled peptides are targeting σ^{54} controlled genes, a decrease in motility should be followed by a decrease in biofilm formation. To assess biofilm growth, an adapted biofilm growth experiment was used to observe and quantify biofilm inhibition through crystal violet staining.[44–46] By using these experiments, it is possible to determine a either growth inhibition or delay in biofilm formation relative to a vehicle control. Much like the motility experiment, the peptides are knocking down activity and should not completely inhibit biofilm formation. It is expected that the peptides will delay the growth of biofilm.

M63 was the cell growth medium as it has been shown to produce a highly robust biofilm.[47] DMSO possesses surfactant properties that enable it to inhibit the natural surface tension of water.[48] As a result, it is important to remember that the local concentration of DMSO on the surface of the plate will vary and may affect the uniformity of biofilm formation. Replicates must be taken each time the assay is performed to ensure that the surfactant effects fail to affect the results.

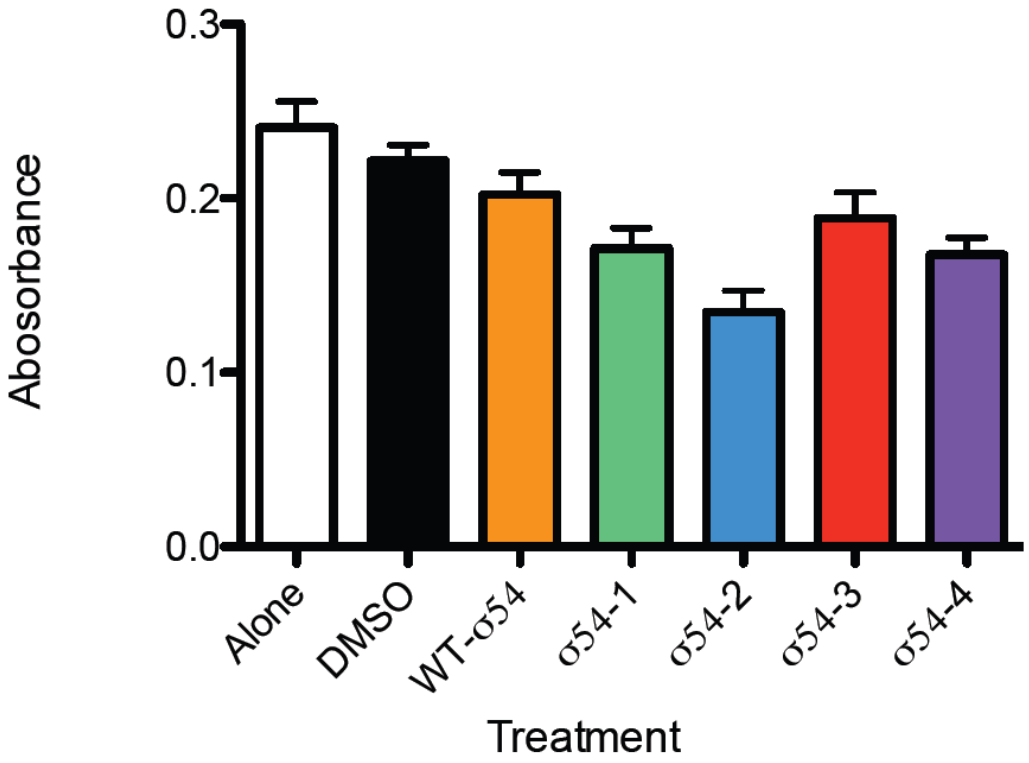

Figure 3.22. Absorbance at 550 nm of retained 1% crystal violet in PA01 biofilms grown 5 hours post-inoculation in 0.4% arginine supplemented M63 medium with 4 μM peptide. One-way ANOVA statistical analysis was conducted with the Dunnett's post-tests to determine significance in all biofilm formation compared to the DMSO vehicle control (Errors bars = SD, n = 3).

As predicted, the amount of biofilm formation (**Fig. 3.22**) is lower in a DMSO solution compared to cells in medium only. With the wild type peptide, further decrease in absorbance relative to both positive controls is observed but it is statistically insignificant (p-value > 0.05). Among all the stapled peptides, there is a modest decrease in biofilm formation (p-value < 0.05) attributed to the stapled peptide inhibiting σ^{54}-regulated transcription with the following ranking: σ^{54}-3 < σ^{54}-1 < σ^{54}-4 < σ^{54}-2. This result is surprising as peptide 3 has shown superior permeability to both peptides 1 and 4. However, as motility appears to display relatively equal phenotypic effects among the four peptides, peptide 2 remains the leading candidate across this study, much like the previous studies. Regardless of the staple's positioning, these peptides inhibit biofilm growth.

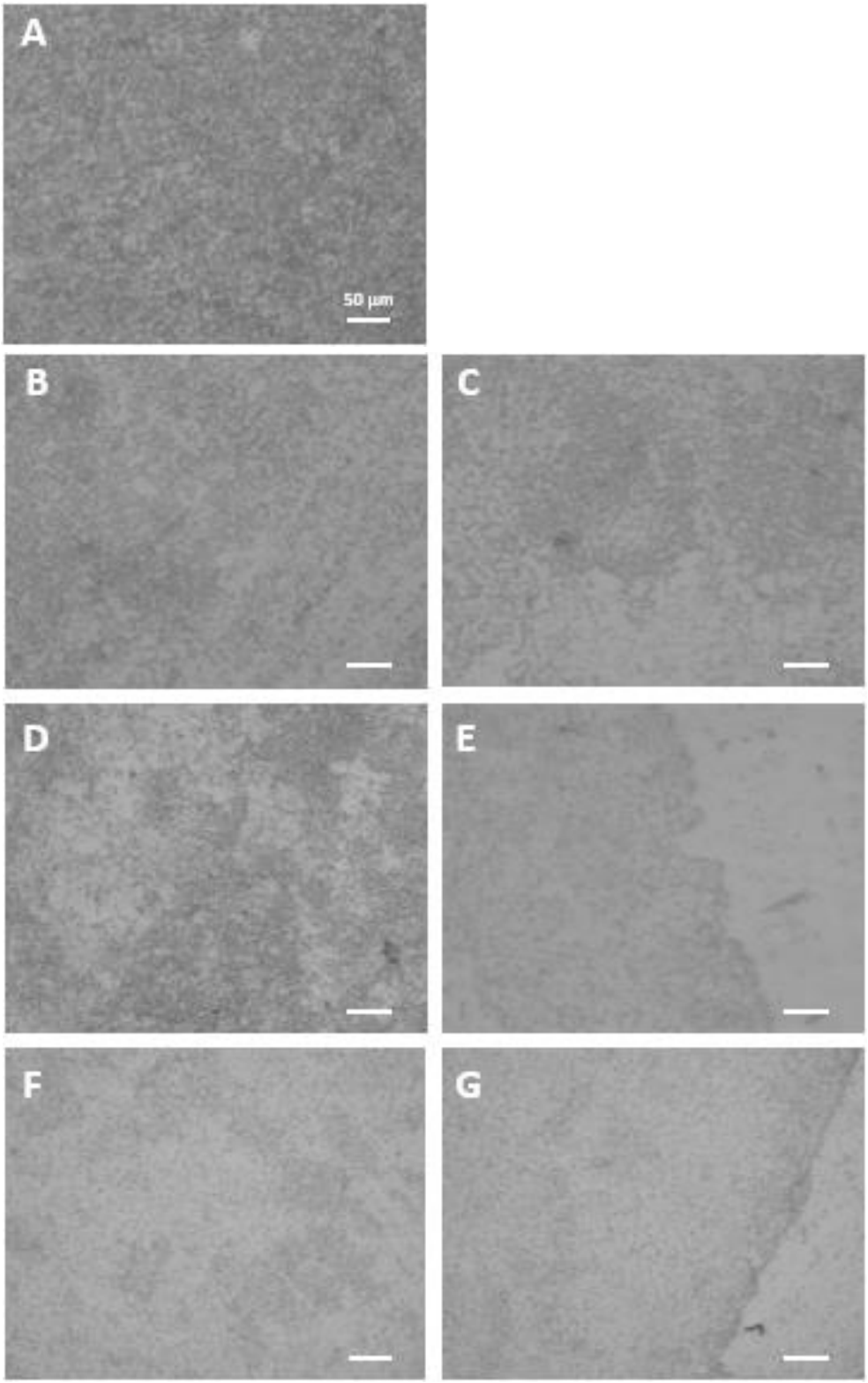

Figure 3.23. Microscopy of crystal violet-stained biofilms of PA01 cells grown 5 hours post-inoculation in 0.4% arginine supplemented M63 medium with 4 µM peptide. The densest area of each biofilm are imaged with **A)** no treatment, **B)** 0.4% DMSO, **C)** WT-σ^{54} unstapled, **D)** σ^{54}-1, **E)** σ^{54}-2, **F)** σ^{54}-3, and **G)** σ^{54}-4, (n = 3).

From the microscopy results in **Fig. 3.23**, the crystal violet absorbance assay is further supported. Both the untreated and DMSO-treated (**Fig. 3.23A-B**) positive controls display highly dense and mature biofilm formation. The unstapled peptide does show patchy areas without biofilm. Among the four stapled peptides, each displays areas lacking biofilm growth as the bacterial cells failed to adhere to the plate due to σ^{54}-inhibited biofilm formation. In particular, peptides 1 and 3, both longer staples, display a patchy profile whereas the shorter staples for peptides 2 and 4 display a general decrease in biofilm formation. To further study this character, further staple-length modified peptides must be synthesized to investigate this phenomenon.

3.2.4.3 Quantitative PCR

As the σ^{54} stapled peptides are designed to inhibit the expression of mRNA, quantitative PCR was used to determine the transcript level of σ^{54}-controlled genes in treated samples.[49] σ^{54}'s involvement in nitrogen assimilation is due to its regulation of the *glnA* gene; this gene encodes a subunit for glutamine synthetase.[50–52] By monitoring this gene in nitrogen-poor conditions, *glnA* expression can be assessed. Samples of gDNA extracted from BW25113 using the Promega Wizard Genomic DNA Purification Kit were used as a positive control in determining qPCR optimization. qPCR makes use of fluorescence-labeled hybridizing probes to quantify cDNA based on replication copies. For the purposes of this experiment, relative quantification was the method used to determine transcription inhibition. When compared to the control samples, a relative inhibition factor can be found.

Primers and DNA concentration were optimized through gradient PCR. The conditions chosen were 50 ng gDNA and 2.5 μM primers. *16S*, ribosomal rRNA,[53] was used as a housekeeping or normalization gene to demonstrate that the peptides specifically inhibit

σ^{54}-mediated transcription. Cells were treated with a similar protocol as the flow cytometry assay and underwent RNA extraction. When converted to cDNA, transcripts were examined with qPCR amplification to determine the proper annealing temperature of each primer set to optimize conditions and minimize PCR inhibition.

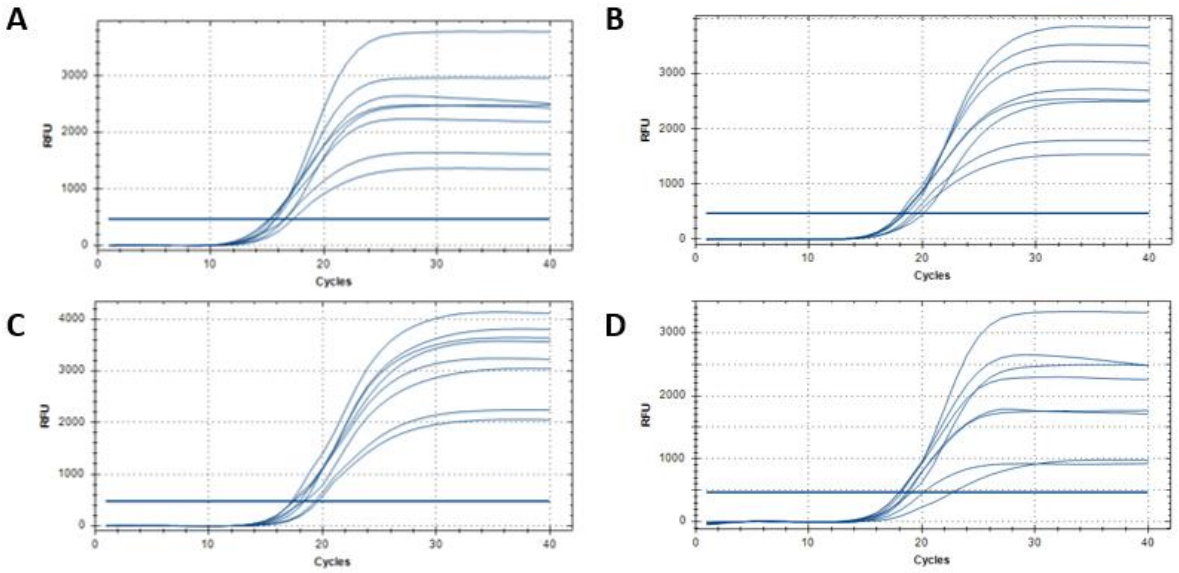

Figure 3.24. BW25113 gDNA amplified qPCR temperature gradient of **A)** *16S*, **B)** *glnA*, **C)** *pspA*, and **D)** *atoD* using SsoFast Evagreen. Each curved line represents a different temperature under examination. The horizontal line represents the threshold used to read the C_q value of each sample without significant background effects (n = 1)

As the amount of template in each sample remains constant, the curve gradients reach similar cycle number (C_q) (**Fig. 3.24**). Based on the above data sets, it was concluded that all the primers demonstrated appreciable amplification from each of the samples at similar melting temperatures at 56°C; this temperature was used as it was consistently among earliest C_q value in the majority of the samples to allow for more reliable dilutions later on.

In general, the accepted limit of qPCR is C_q = 35 due to the possible background amplification after this range. Any detected C_q values from cDNA sample preparations approaching this number may not be of significance. The same annealing temperature can be used with the following calculation:

$$Dilution\ factor = 2^{\frac{Maximum\ accepted\ Cq}{Maximum\ accepted\ Cq\ -\ Optimized\ Cq\ value}} = 2^{\frac{35}{17}} = 2^{2.125} \cong 4.5X$$

Upon application of this dilution factor, standard curves for each primer set were generated relative to the DMSO-treated cDNA samples. This was done to create a standard curve within the vehicle conditions to determine the general amplicon concentration associated with each PCR cycle. Once the cDNA peptide-treated samples have been amplified, it is be possible to determine transcriptional inhibition due to stapled peptide treatment relative to its vehicle controls. With a standard curve based on the control sample, the peptide-treated samples will theoretically possess lower C_q values and thus the relative decrease in expression may be interpolated from the data.

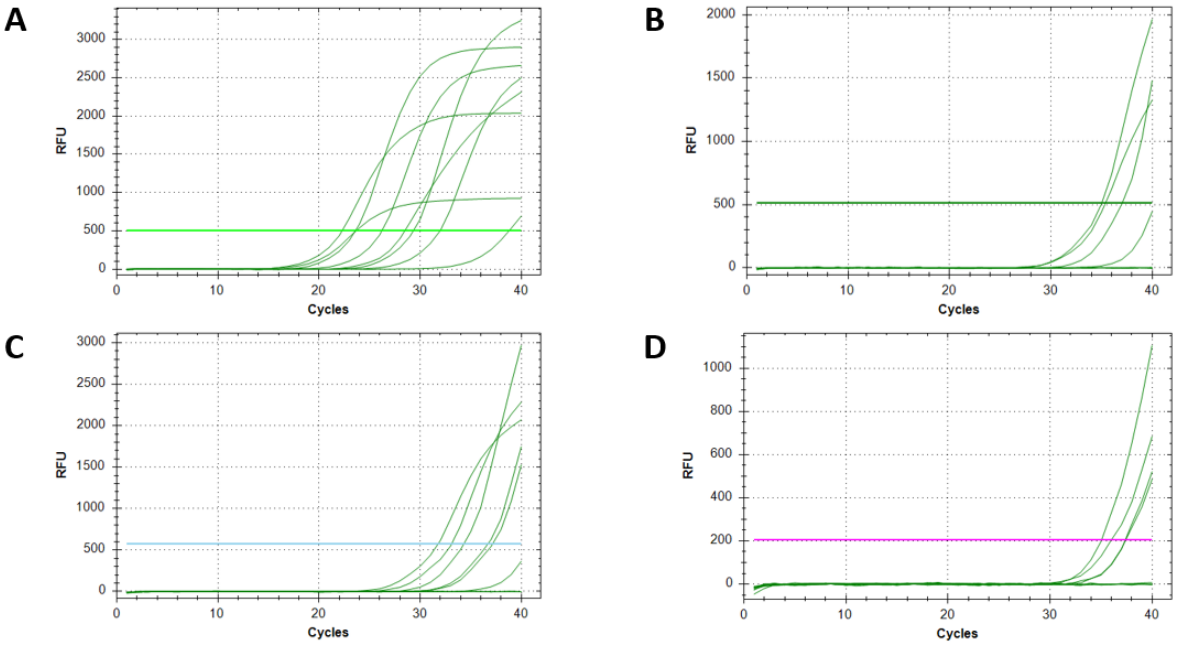

Figure 3.25. Standard curves of DMSO-treated BW25113 cDNA amplified by qPCR of **A)** *16S*, **B)** *glnA*, **C)** *pspA*, and **D)** *atoD* using SsoFast Evagreen. Each curved line represents a 4.5X serial dilution of the treated sample. The horizontal line represents the threshold used to read the C_q value of each sample without significant background effects (n = 3).

When DMSO-treated samples were analyzed with qPCR, it seems that the native ability of DMSO to inhibit bacterial transcription during the growth phase plays a significant

role. From the 16S samples (**Fig. 3.25A**), it seems that there is relatively non-uniform spacing due to pipetting errors. Furthermore, the saturation relative fluorescence unit (RFU) appears to be comparable to gDNA samples. The gene is being expressed in appreciable quantities comparable to **Fig. 3.24A** as the C_q at its highest concentration starts at 21. In **Fig. 3.24B-D**, their expression levels are already quite low. It seems that the number of mRNA transcripts expressed natively in DMSO-treated cells is already significantly decreased due to poor C_q values. By making use of dilutions, it seems that the genes under σ^{54}-regulation may not be detected with expression values close to 35. As a result, qPCR is not sensitive enough to detect the mRNA of *glnA*, *pspA*, or *atoD* due to either a low expression or copy number within vehicle conditions.

3.2.4.4 Digital Droplet PCR

Although qPCR was not sensitive enough to detect transcription levels, another technique is even more sensitive in DNA detection. Droplet digital PCR, a method developed in the last 5 years, makes use of microfluidics and surface chemistry to divide PCR samples into oil droplets surrounded by water.[54] Within each droplet, DNA is isolated and can undergo replication to generate fluorescence. These fully amplified droplets are read by a flow cytometer to determine the PCR positive and negative droplets and analyzed using Poisson statistics to obtain an exact number of DNA copies.[54]

A number of treated samples were evaluated through droplet digital PCR through absolute quantification. As the genes of interest have low copy numbers, this method was chosen as opposed to conventional qPCR due to higher precision, improved reproducibility, and reduced effect of pipetting errors.[55]

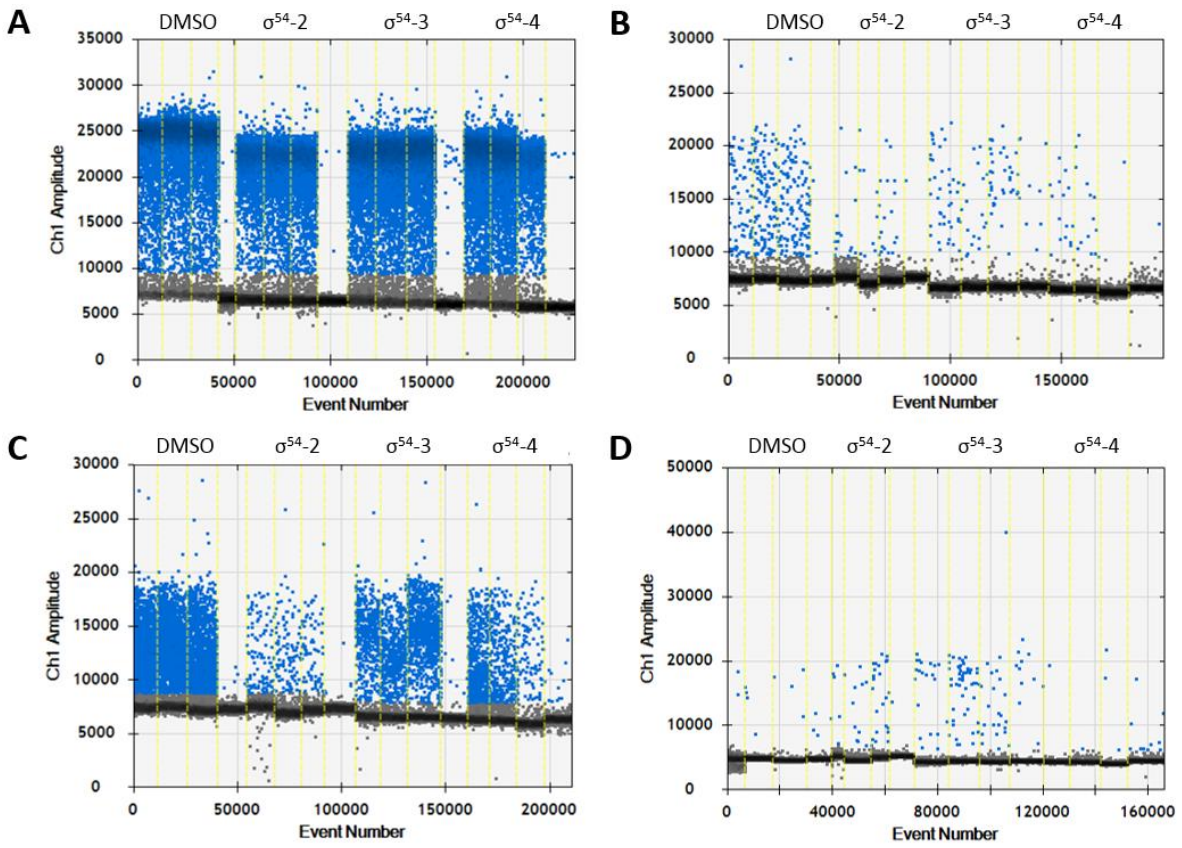

Figure 26. Digital droplet PCR of treated BW25113 cDNA samples with the follow primer sets: **A)** 16S, **B)** glnA, **C)** pspA, and **D)** atoD. Blue dots represent positive droplets, black drops represent negative droplets and yellow lines indicate separate samples (in order, n = 3 for cDNA, n = 1 no reverse transcriptase control).

The majority of droplets are negative, lacking DNA, but the positive droplets are present in appreciable quantities. **Fig. 3.26A** demonstrates that the *16S* cDNA is at 2.4 x 10^5 copies/µL in DMSO, a high amount as ribosomes are highly expressed in cells. However, with peptide treatment, their expression decreases to 4.1 x 10^3, 1.5 x 10^4, and 1.3 x 10^4 copies/µL in σ^{54}-2, σ^{54}-3, and σ^{54}-4 respectively. As seen in **Fig. 3.26B**, *glnA* expression in the DMSO vehicle control is higher than other peptide treatment by approximately 100 times; from 100 to 1 copy/µL. This is an excellent indicator that corroborates with the phenotypic experiments. *PspA* expression has decreased expression as well (**Fig. 3.26C**), ranging from 2 to 15 times with similar copy numbers to glnA. With *atoD* (**Fig. 3.26D**), there appears to

be little to no expression at all in both vehicle and peptide treatments. As a result, it may be that atoD is only expressed in different environmental conditions or it remains unaffected by the peptides.

However, the problem with this data is that the housekeeping gene, *16S*, is downregulated as well to a degree. This may be an artifact based on the experimental conditions or the nature of the peptide. As the peptides were incubated for 90 min with the bacteria, other side effects of the peptide may have occurred. For example, based on the microscopy data, the peptides were shown to cause DNA aggregation. It may be that RNA aggregation was also caused since RNA shares many chemical properties similar to DNA. In general, σ^{54}-2 seems to possess the strongest activity in downregulation of expression.

3.3 Conclusions and Prospects

In summary, RpoN modeled σ^{54} hydrocarbon stapled α-helical peptides have been shown as a viable method of interrogating bacterial systems. We have demonstrated that the peptides preserve their α-helical secondary structure in water due to the staple. The peptides exert a stronger viability-based activity on bacteria as opposed to mammalian cells. FITC-tagged peptides have been shown to penetrate cells through a non-ATP based diffusion mechanism and cause DNA aggregation within the cell. Through further fluorescence-based methods, the peptide was found to bind with a high nanomolar affinity through anisotropy studies and with specificity to the -24 site of glnA through FRET-FLIM-based experiments. Finally, the peptide shows promising biological activity through the examination of σ^{54}-linked processes such as motility and biofilm examination. σ^{54}-2, a peptide with a smaller staple localized around the key arginine residues, has consistently displayed the best characteristics across various experiments and is currently the lead compound of this project.

Although the peptides appear to function as designed, certain experiments were inconclusive. With the EMSA, the peptides were shown to cause eventual displacement of the complex but this finding is compounded by a problem with aggregation. The preliminary anisotropy experiments were performed to bypass this problem. Further studies using isothermal titration calorimetry (ITC) or microscale thermophoresis (MST) could be used to find the dissociation constants by other temperature-based methods. Like anisotropy, the unbound and bound states are separate and the midpoint between both is the K_D. However, different properties will be measured. ITC examines temperature changes with molecular interactions and MST examines hydration shell properties and movement across temperature gradients.

Furthermore, experiments examining the mRNA transcript proved difficult. The current hypothesis is due to the peptide's natural ability to cause DNA aggregation, and thus RNA aggregation. Throughout the experiments, the peptide may artificially sequester the mRNA transcripts alongside other type of DNA. Based on this hypothesis, to properly assess the effects of the peptide on mRNA transcription, the peptide must be removed from solution somehow. Dilutions coupled with affinity-based chromatography steps may be done to separate the peptide from its aggregate and from a lysis. Other chemical treatments such as surfactants may be tested to dislodge the peptides from the aggregates.

At this time, there remains a number of items to refine. With regards to further work, the bacteria may be treated in a real-time fashion to discover the specific method of entry of the peptides into bacteria to support the mechanism of entry. The biofilms work must be further examined with microscopy for penetration post-formation, as is commonly the case in a clinical setting. Further studies of the phenotypic effects such as downstream protein expression, and further mRNA analysis is necessary. Finally, as bacteria have not been studied with this molecule class, scrambled peptide sequences must be analyzed to ensure that the effects are not simply caused by the presence of the class of molecules.

Through these studies, this class of molecules holds untapped potential in developing new tools and drugs that target previously untargeted biological targets. Furthermore, these peptides could be used as carriers to allow antibiotics with penetration issues to cross Gram negative pathogens. As many stapled peptides are at the forefront of the next generation of drugs, there remains a whole bacterial proteome to explore.

3.4 References

1. Casaz, P. *et al.* Systematic analysis of sigma54 N-terminal sequences identifies regions involved in positive and negative regulation of transcription. *J. Mol. Biol.* **292,** 229–239 (1999).

2. Oguiza, J. A. *et al.* Involvement of the sigmaN DNA-binding domain in open complex formation. *Mol. Microbiol.* **33,** 873–885 (1999).

3. Buck, M. & Cannon, W. Specific binding of the transcription factor sigma-54 to promoter DNA. *Nature* **358,** 422–424 (1992).

4. Barrios, H. *et al.* Compilation and analysis of σ54-dependent promoter sequences. *Nucleic Acids Res.* **27,** 4305–4313 (1999).

5. Wang, L. & Gralla, J. D. Multiple in vivo roles for the -12-region elements of sigma 54 promoters. *J. Bacteriol.* **180,** 5626–5631 (1998).

6. Kawamoto, S. A. *et al.* Design of triazole-stapled BCL9 α-helical peptides to target the β-catenin/B-cell CLL/lymphoma 9 (BCL9) protein-protein interaction. *J. Med. Chem.* **55,** 1137–1146 (2012).

7. Wong, C. *et al.* The Domain Structure of σ54 as Determined by Analysis of a Set of Deletion Mutants. *J. Mol. Biol.* **236,** 81–90 (1994).

8. Doucleff, M. *et al.* The C-terminal RpoN domain of σ54 forms an unpredicted helix-turn-helix motif similar to domains of σ70. *J. Biol. Chem.* **280,** 41530–41536 (2005).

9. Doucleff, M. *et al.* Structural Basis of DNA Recognition by the Alternative Sigma-factor, σ54. *J. Mol. Biol.* **369,** 1070–1078 (2007).

10. Wang, L. & Gralla, J. D. Roles for the C-terminal Region of Sigma 54 in Transcriptional Silencing and DNA Binding. *J. Biol. Chem.* **276,** 8979–8986 (2001).

11. Brown, C. J. *et al.* Stapled peptides with improved potency and specificity that activate p53. *ACS Chem. Biol.* **8,** 506–512 (2013).

12. Kim, Y. W. & Verdine, G. L. Stereochemical effects of all-hydrocarbon tethers in i,i+4 stapled peptides. *Bioorganic Med. Chem. Lett.* **19,** 2533–2536 (2009).

13. Greenfield, N. & Fasman, G. D. Computed circular dichroism spectra for the evaluation of protein conformation. *Biochemistry* **8,** 4108–4116 (1969).

14. Greenfield, N. J. Using circular dichroism spectra to estimate protein secondary structure. *Nat. Protoc.* **1,** 2876–2890 (2009).

15. Cockerill, F. R. *et al. Methods for Dilution Antimicrobial Susceptibility Tests for Bacteria That Grow Aerobically ; Approved Standard — Ninth Edition*. **32,** (2012).

16. Mosmann, T. Rapid colorimetric assay for cellular growth and survival: application to proliferation and cytotoxicity assays. *J. Immunol. Methods* **65,** 55–63 (1983).

17. Alley, M. C. *et al.* Feasibility of Drug Screening with Panels of Human Tumor Cell Lines Using a Microculture Tetrazolium Assay. *Cancer Res.* **48,** 589–601 (1988).

18. Scudiero, D. A. *et al.* Evaluation of a Soluble Tetrazolium / Formazan Assay for Cell Growth and Drug Sensitivity in Culture Using Human and Other Tumor Cell Lines. *Cancer Res.* **48,** 4827–4833 (1988).

19. Berridge, M. V. & Tan, A. S. Characterization of the cellular reduction of 3-(4,5-dimethylthiazol-2-yl)-2,5-diphenyltetrazolium bromide (MTT): subcellular localization, substrate dependence, and involvement of mitochondrial electron transport in MTT reduction. *Arch. Biochem. Biophys.* **303,** 474–482 (1993).

20. Noumi, T. *et al.* Mode of inhibition of sodium azide on H+-ATPase of Escherichia coli. *FEBS Lett.* **213,** 381–384 (1987).

21. Eswaramoorthy, P. *et al.* Cellular architecture mediates DivIVA ultrastructure and regulates min activity in Bacillus subtilis. *MBio* **2,** 1–9 (2011).

22. Garner, M. M. & Revzin, A. A gel electrophoresis method for quantifying the binding of proteins to specific DNA regions: application to components of the Escherichia coli lactose operon regulatory system. *Nucleic Acids Res.* **9,** 3047–3060 (1981).

23. Fried, M. G. Measurement of protein-DNA interaction parameters by electrophoresis mobility shift assay. *Electrophoresis* **10,** 366–376 (1989).

24. Armon-Omer, A. *et al.* Correlation Between Shiftide Activity and HIV-1 Integrase Inhibition by a Peptide Selected from a Combinatorial Library. *J. Mol. Biol.* **376,** 971–982 (2008).

25. Drewry, J. A. *et al.* Coordination complex SH2 domain proteomimetics: an alternative approach to disrupting oncogenic protein-protein interactions. *Chem. Commun. (Camb).* **46,** 892–894 (2010).

26. Lakowicz, J. R. *et al.* Enhanced resolution of fluorescence anisotropy decays by simultaneous analysis of progressively quenched samples. Applications to anisotropic rotations and to protein dynamics. *Biophys. J.* **51,** 755–768 (1987).

27. Baeissa, A. *et al.* DNA-functionalized monolithic hydrogels and gold nanoparticles for colorimetric DNA detection. *ACS Appl. Mater. Interfaces* **2,** 3594–3600 (2010).

28. Cheng, Y. *et al.* Fluorescence near gold nanoparticles for DNA sensing. *Anal. Chem.* **83,** 1307–1314 (2011).

29. Cremazy, F. G. E. *et al.* Imaging in situ protein-DNA interactions in the cell nucleus using FRET-FLIM. *Exp. Cell Res.* **309,** 390–396 (2005).

30. Wouters, F. S. *et al.* Imaging biochemistry inside cells. *Trends Cell Biol.* **11,** 203–211 (2001).

31. Simoncelli, S. *et al.* Thermoplasmonic ssDNA Dynamic Release from Gold Nanoparticles Examined with Advanced Fluorescence Microscopy. *J. Phys. Chem. Lett.* **6,** 1499–1503 (2015).

32. Llères, D. *et al. Detecting protein-protein interactions in vivo with FRET using multiphoton fluorescence lifetime imaging microscopy (FLIM). Current protocols in cytometry* **Chapter 12,** (2007).

33. Jares-Erijman, E. A. & Jovin, T. M. FRET imaging. *Nat. Biotechnol.* **21,** 1387–1395 (2003).

34. Selvin, P. R. The renaissance of fluorescence resonance energy transfer. *Nat. Struct. Biol.* **7,** 730–734 (2000).

35. Schuler, B. *et al.* Probing the free-energy surface for protein folding with single-molecule fluorescence spectroscopy. *Nature* **419,** 743–747 (2002).

36. Edelhoch, H. *et al.* Fluorescence studies with tryptophyl peptides. *Biochemistry* **6,** 547–559 (1967).

37. George Abraham, B. *et al.* Fluorescent Protein Based FRET Pairs with Improved Dynamic Range for Fluorescence Lifetime Measurements. *PLoS One* **10,** e0134436 (2015).

38. Pratt, L. A. & Kolter, R. Genetic analysis of Escherichia coli biofilm formation: roles of flagella, motility, chemotaxis and type I pili. *Mol. Microbiol.* **30,** 285–293 (1998).

39. Tosi, T. *et al.* Structural basis of eukaryotic cell targeting by type III secretion system (T3SS) effectors. *Res. Microbiol.* **164,** 605–619 (2013).

40. Duan, Q. *et al.* Flagella from F18+ Escherichia coli play a role in adhesion to pig epithelial cell lines. *Microb. Pathog.* **55,** 32–38 (2013).

41. Henchey, L. K. *et al.* Contemporary strategies for the stabilization of peptides in the α-helical conformation. *Curr. Opin. Chem. Biol.* **12,** 692–697 (2008).

42. Parthasarathy, G. *et al.* Flagella promote Escherichia coli K1 association with and invasion of human brain microvascular endothelial cells. *Infect. Immun.* **75,** 2937–2945 (2007).

43. Lane, M. C. *et al.* Role of Motility in the Colonization of Uropathogenic Escherichia coli in the Urinary Tract. *Infect. Immun.* **73,** 7644–7656 (2005).

44. O'Toole, G. A. Microtiter dish biofilm formation assay. *J. Vis. Exp.* e2437 (2011). doi:10.3791/2437

45. Merritt, J. H. *et al.* Growing and analyzing static biofilms. *Curr. Protoc. Microbiol.* 1–18 (2011). doi:10.1002/9780471729259.mc01b01s22

46. Cady, N. C. *et al.* Inhibition of biofilm formation, quorum sensing and infection in pseudomonas aeruginosa by natural products-inspired organosulfur compounds. *PLoS One* **7,** (2012).

47. Mah, T. *et al.* A genetic basis for Pseudomonas aeruginosa biofilm antibiotic resistance. *Nature* **426,** 306–310 (2003).

48. Kligman, A. M. Topical Pharmacology and Toxicology of Dimethyl Sulfoxide. 1. *J. Am. Med. Assoc.* **193,** 796–804 (1965).

49. Becker-André, M. & Hahlbrock, K. Absolute mRNA quantification using the polymerase chain reaction (PCR). A novel approach by a PCR aided transcript titration assay (PATTY). *Nucleic Acids Res.* **17,** 9437–9446 (1989).

50. Reitzer, L. J. & Magasanik, B. Transcription of glnA in E. coli is stimulated by activator bound to sites far from the promoter. *Cell* **45,** 785–792 (1986).

51. Reitzer, L. J. *et al.* Mutations that create new promoters suppress the sigma 54 dependence of glnA transcription in Escherichia coli. *J. Bacteriol.* **169,** 4279–4284 (1987).

52. Da Silva Neto, J. F. *et al.* Global gene expression under nitrogen starvation in Xylella fastidiosa: contribution of the σ54 regulon. *BMC Microbiol.* **10,** 231 (2010).

53. Brosius, J. *et al.* Complete nucleotide sequence of a 16S ribosomal RNA gene from Escherichia coli. *Proc. Natl. Acad. Sci. U. S. A.* **75,** 4801–4805 (1978).

54. Hindson, B. J. *et al.* High-throughput droplet digital PCR system for absolute quantitation of DNA copy number. *Anal. Chem.* **83,** 8604–8610 (2011).

55. Hindson, C. M. *et al.* Absolute quantification by droplet digital PCR versus analog real-time PCR. *Nat. Methods* **10,** 1003–5 (2013).

56. Lakowicz, J. R. *Principles of Fluorescence Spectroscopy Principles of Fluorescence Spectroscopy*. (2006).

57. Gadagkar, S. R. & Call, G. B. Computational tools for fitting the Hill equation to dose-response curves. *J. Pharmacol. Toxicol. Methods* **71,** 68–76 (2015).

58. Arslan, G. *et al.* Surface Modification of Glass Beads with an Aminosilane Monolayer. *Turk. J. Chem.* **30,** 203–210 (2006).

3.5 Experimental

3.5.1 Solid-Phase Peptide Synthesis

All amino acids were Fmoc protected at the N-terminus for C to N peptide synthesis. To begin, the TETRAS was purged with three 50 mL washes of NMP. To make 3.0 x 10^{-5} moles of peptide, 103 mg of Rink amide resin (resin substitution = 0.29 mmol/g) were weighed and loaded into wells. Amino acid solutions (0.3 M) were made on a 10X scale to ensure near perfect coupling. Terminal alkene amino acids were dispensed on a 5X scale. The two crosslinking amino acids used were the Fmoc-S5-OH (Fmoc-(S)-2-(4'-pentenyl)Ala-OH) and Fmoc-R8-OH (Fmoc-(R)-2-(7-octenyl)Ala-OH). HCTU (0.3 M) was used as the peptide coupling reagent (0.123 g per reaction). DIPEA (0.3 M) was used to activate the C-terminal ends of the amino acids. All reactions were performed at room temperature as the TETRAS lacked a temperature control chamber. As a result, all the reactions had extended reaction times to fully react with the resin.

When adding one amino acid to the resin, the usual procedure is to couple, wash, deprotect, wash, and repeat with each monomer addition. To couple, 1 mL of amino acid solution (10X), 0.99 mL HCTU, and 2 mL DIPEA solution were mixed for 60 minutes. For all washes, 3 mL DCE was used to wash the resin 3 times for 3 minutes. For the Fmoc deprotection step, 3 mL of 25% piperidine in NMP was mixed for 2 minutes, then purged and repeated for 20 minutes. In the case of the unnatural crosslinking amino acid, the deprotection step was repeated an extra cycle to ensure that the protecting group was gone due to the amino acid's lowered reactivity. For short staples, two S5 amino acids were used. For long staples, the S5 amino acid was added first, followed by the R8 amino acid. Crosslinkers were coupled at 5X couplings with half the normal reagents. However, the

coupling was performed twice so the overall coupling amount is the same as normal amino acids. For the amino acids loaded onto crosslinker amino acids, the coupling time was doubled to 120 minutes due to the crosslinker's lower reactivity.

To form the ring closing cyclization or "stapled" portion of the peptides, the resin loaded with peptide was swelled for 15 minutes in 3 mL NMP. Afterwards, the resin was washed with DCE. 3 mL of Grubbs I catalyst (5 mg/mL) was used to catalyze the olefin metathesis and reacted for 6 hours. The six hour reaction was repeated twice for a total of 18 hours. Once metathesized, the resin was washed four times with DCE for 3 minutes (4 mL). The compounds either remained on resin without deprotection or were capped with either acetyl groups or FITC-functionalized amino acids. To preserve the peptides, the resin was washed four times with 4 mL DCE for 3 minutes and shrunk four times with 3 mL of methanol for 5 minutes per wash.

For acetylation, the resin was swelled for 15 minutes with NMP. Fmoc deprotection was done with 25% piperidine in NMP twice: 3 mL for 2 minutes and 3 mL for 20 minutes. After washing with NMP, 1mL of 100% acetic anhydride, 0.5 mL DIPEA, and 1.5 mL NMP were mixed and added to the resin for 60 minutes. Once completed, the resin with loaded peptide was purged, washed, and shrunk with the methanol wash.

For fluorescein capping, the resin was swelled for 15 minutes with NMP. The resin was mixed with of 0.2 mL DIPEA and 2.8 mL FITC (10 mg/mL) for 12 hours. After purging the solution, the resin loaded with FITC-tagged peptide was washed with DMF, DCM, and shrunk with methanol for storage.

Peptides were fully deprotected and cleaved from the resin with a mixture of TFA : TIPS : H_2O (19.0 : 0.5 : 0.5). This TFA cleavage cocktail was added to the resin and stirred for 3 hours at room temperature. Afterwards, a 1:1 mixture of MTBE:hexanes was added to precipitate the peptides as they are polar. Once completed, the peptides were spun down at 4°C for 14 000 rpm for 15 minutes. After pelleting the peptides, a mixture of 1:1 acetonitrile:water was used to solubilize the peptides. Stapled peptides were purified by HPLC/MS and then quantified by both mass and UV spectroscopy. All collected fractions were analyzed by mass spectrometry to determine the presence of each peptide. Once a fraction was deemed to have the peptide, the fractions were pooled together, aliquoted, lyophilized, and stored at -20°C.

3.5.2 Minimum Inhibitory Concentration

From a frozen stock of cells, a plate of BW25113 *E. coli* (Keio collection) cells was streaked on LB-agar medium and grown overnight at 37°C for 18 hours. A seed culture was taken from the plate and grown overnight in Müeller-Hinton Broth (MHB). Cells were diluted to $OD_{600} \approx 0.1$ with MHB as this will concentrate the *E. coli* to 1 x 10^8 cells/mL to allow cells to regrow into log phase. Cells were incubated at 37°C, shaking for 200 rpm, for 40 minutes (2 doubling times) to allow cells to reach log phase ($OD_{600} \approx 0.4$-0.6). Cells were again diluted to $OD_{600} \approx 0.1$ with MHB. Beginning at a concentration of 1024 μg/mL, a 96 well plate was prepared. Solutions were diluted by a factor of 2 with a constant volume of vehicle. Once fully diluted to 2 μg/mL, 2.5 x 10^5 cells were added. After sealing the plate with parafilm, cells were incubated for 18h while shaking at 50 rpm for 37°C. Visual imaging and plate reader assays were used to determine the MIC of each peptides with $OD_{600} \approx 0.04$ as a background value.

3.5.3 Cytotoxicity

Prior to conducting the actual assay, the cells used to measure compound toxicity must be plated. WS1 cells were grown and treated with 0.5% EDTA-Trypsin and pelleted at 1 400 RPM for 3 minutes. Cells were resuspended in an appropriate amount of medium and counted using a haemocytometer and split to achieve the correct concentration. Cells were aliquoted into each well of a Corning white, opaque 96 well plate so that the number of cells is approximately 15 000. Each well was topped up to a final volume of 100 μL of medium and incubated at 37°C overnight to allow cells to adhere to the plate. Stock solutions of each compound under investigation were prepared in Opti-MEM at 4°C. Serial dilutions were prepared in a 1:1 ratio. The medium was removed from the 96 well plate and replaced with the Opti-MEM-DMSO-peptide mixture. Cells were incubated at 37°C for 24 hours.

The CellTiter-Glo kit was used to analyze cytotoxicity. The kit's reagents were mixed and protected from light as per the manufacturer's instructions. This solution was diluted 4x with sterile PBS and 100 μL was added to all wells. The luminescence was read on a plate reader at 560 nm to quantify the ATP present in cells.

3.5.4 Flow Cytometry

Overall, the final protocol for the flow cytometry work was as follows. From a streaked out plate, BW25113 and PA01 cells were seeded and grown overnight. The following day, cells were diluted to OD ≈ 0.1 and grown in LB medium for approximately 40 min to enter the log phase of growth. 1 x 10^8 cells were used in each treated sample. Cells were centrifuged at 13 000 g for 60s at 25°C and washed twice and resuspended in 500 μL of PBS. Stapled peptides were incubated with the bacteria at 37°C for 90 min to a final

concentration of 4 μM. After washing once with PBS like before, the cells were left as pellets and placed on ice at 4°C for 30 min. The bacteria were resuspended with PBS and 0.4% (w/v) Trypan Blue to quench extracellular fluorescence. Finally, cells were washed and resuspended in 500 μL to be placed within the flow cytometer. To determine the mode of transport within the cell, 10 mM sodium azide was used to inactivate ATPases used for transporting hydrogen ions.[20] The following voltages were used on the flow cytometer to determine cell population localization: side scatter at 253 ADC, forward scatter at 213 ADC, and FL1 at 550 ADC.

3.5.5 Confocal Microscopy

The microscopy protocol corresponds to the majority of the flow cytometry protocol. Cells from an overnight seed culture were diluted and grown until log phase and 1 x 10^6 cells were used for each sample. After resuspending in PBS and washing for 2x, cells were incubated with peptide for 30 minutes at 37°C for the peptide to enter the cells. Cells were then washed with PBS and pelleted and concentrated 10X. The bacteria were stained with FM4-64 (1μg/mL) and DAPI (2μg/mL) to visualize both the cell membrane and double stranded DNA respectively. On a glass-bottom culture dish, a 1% agarose pad made from distilled water was used to flatten the bacteria into a monolayer of cells. Cells were visualized on non-polylysine coated slides on an environmental control chamber confocal microscope at 100X objective. Images were captured on a DeltaVision Core microscope system (Applied Precision) equipped with a Photometrics CoolSnap HQ2 camera and environmental chamber. The data was analyzed using SoftWorx.

3.5.6 Electrophoretic shift mobility assay

In the initial studies, oligomers were annealed at 100°C for 3 minutes, followed by a slow cool to room temperature for 30 minutes. Once completed, the following concentrations were used to evaluate the binding complex (diluted from 10X solutions): 1X binding buffer (10 mM Tris, 50 mM KCl, 1 mM DTT; pH 7.5); Poly (dI·dC) 0.1 μg/μL in 1 mM Tris, 0.1 mM EDTA, pH 7.5; 2.5 mM DTT/0.25% Tween 20; 2.5 nM $IRDye_{700}$ oligomers; and a concentration range of 0-20 μM acetylated stapled peptide. The reaction was allowed to proceed for 30 minutes at ambient temperature. Once bound, orange loading dye was added to all samples and separated by electrophoresis through an 8% TBE gel at 10 V/cm for 30 minutes in TBE buffer, a non-denaturing buffer. Gels were imaged on a LI-COR Odyssey Infrared Imaging System.

3.5.7 Anisotropy

All the steady state fluorescence experiments were conducted at 25 °C and measured using FilterMax F5 multi-mode multiplate reader and Multi-mode analysis software (Molecular Devices, Sunnyvale, CA). A 5 nM constant concentration of FITC-tagged σ^{54} stapled α-helical peptide was incubated with varying concentrations of unlabeled DNA (0 – 50 nM) in a MicroWell 96-well optical-bottom black plate for cell cultures (Thermo Scientific, USA), for 5 hours. Then the samples were excited at 485 nm, and the fluorescence polarization was measured with an emission filter 535 nm. The anisotropy (r) of the FITC-peptide was computed based on the equation defined below,[56] where I_{VV} and I_{VH} are the intensities of the fluorescence signals with parallel and perpendicular polarization respectively and the G is the G factor of the instrument.

$$r = \frac{I_{VV} - G \times I_{VH}}{I_{VV} + 2 \times G \times I_{VH}}$$

Once the data points have been determined, the data was modeled against a Hill plot. This linear approximation of the data is based on the equation defined below,[57] where a is the Y value at the bottom plateau, b is the Y value at the top plateau, logEC50 is the X value when the response is at the inflection point of the curve, and the c describes the Hill coefficient which is the slope of the curve.

$$Y = a + \frac{b - a}{1 + 10^{(logEC50 - X)\,c}}$$

3.5.8 Fluorescence Lifetime Imaging Microscopy

3.5.8.1 Gold Nanoparticle & functionalization of glass slips

Using the Turkevich method, gold nanoparticles were synthesized by combining chloroauric acid ($HAuCl_4$) and sodium citrate ($Na_3C_6H_5O_4$) in ddH_2O. Briefly, 95 mL of 25 mM tetrachloroauric acid and 5 mL of 1.0% w/v trisodium citrate were first heated. 5 mL of the heated trisodium citrate was added to the tetrachloroauric acid solution and left to boil (100°C) for 30 more minutes upon the addition. The resulting mixture changed its colour from clear, grey, light pink, red and finally to wine red.

3.5.8.2 AuNP functionalization of coverslip

Glass slips (24 x 40 x 0.15 mm) were treated for 1 hour in piranha solution (3:1 concentrated H_2SO_4:H_2O_2). After the piranha treatment the glass slips were removed from the solution, followed by a rinsing with tap water, distilled water and ultrapure Milli-Q water for 10 minutes intervals and drying under a stream of nitrogen. The freshly cleansed glass

slips were immersed in 4.0% (v/v) APTES in anhydrous toluene for 50 minutes under agitation. Afterwards the glass slips were removed from the solution, followed by a sequence of 2 washes with acetone and 18.2 MΩ deionized water in order to remove any physiosorbed APTES molecules. Note that it is very important to remove the excess of APTES from the silanized glass slips to prevent AuNP aggregation.[58]

1300 μL of freshly prepared AuNP solution was deposited on to the surface of the silanized glass slips for 30 minutes. Afterwards the excess solution was removed and the glass slips were rinsed thoroughly with 18.2 MΩ deionized water in order to remove any unattached AuNPs.

3.5.8.3 AuNP DNA functionalization

A 1.0 mM solution of lipoic acid was firstly sonicated for 45 min using a Bransonic B1510 sonicator and subsequently deposited on to the surface of the AuNP covered silanized glass slips over 2 h (25.0 ± 0.5° C, dark). In order to remove any unattached and physiosorbed lipoic acid molecules, the excess was removed and rinsed thoroughly with 18.2 MΩ deionized water.

Aminated dsDNA constructs were reacted with lipoic acid-AuNP conjugates directly through the specific amide attachment with the help of amide specific activating agents. A solution mixture containing 10.0 nM dsDNA, 0.020 M EDC, 0.015 M sulfo-NHS, 0.100 M MES buffer and 1.00 M NaCl was prepared and deposited onto the surface of the lipoic acid functionalized AuNP covered glass slip. The samples were then incubated in a humidity chamber for 3.5 h (4.0 ± 0.5° C, dark). The excess solution was removed and the glass slips were rinsed thoroughly with 18.2 MΩ deionized water in order to remove any unattached and physiosorbed dsDNA constructs.

3.5.8.4 Peptide complex treatment

1 mL of 10 nM peptide unstapled, 1, 2, 3, and 4 was incubated on the AuNP-DNA conjugate functionalized coverslip in a humidity chamber for 3.5 h (4.0 ± 0.5° C, dark). The excess solution was removed and the glass slips were rinsed thoroughly with 18.2 MΩ deionized water.

3.5.8.5 Fluorescence lifetime imaging of AuNPs bound with peptide

The specific interactions between the DNA wild type (DNA_{WT})and knockout (DNA_{KO}) and the peptides (unstapled, 1, 2, 3, and 4) were determined using a PicoQuant MicroTime200 Fluorescence Lifetime Imaging Microscope system equipped with a frequency doubled picosecond pulsed laser (485 nm, 100 ps, 40 MHz, LDH-D-C-485, PicoQuant). The AuNP functionalized coverslip containing the immobilized DNA_{WT}-peptide complex and the DNA_{KO}-peptide complex was placed onto an oil immersion TIRF objective (100X, NA 1.45, Olympus, PLAPO). A 485 nm laser was used as the irradiation source, where a beam splitter (500dcxr, Chroma) was used to reflect the excitation light onto the objective. The epifluorescence signal was passed through a 525/50 nm band pass filter (Chroma). The fluorescence intensity images and lifetime traces were recorded using a single-photon counting module (τ-SPAD-100, PicoQuant) and Time Correlated Single Photon Counting Module (TSCPC), and processed using SymPhoTime program (PicoQuant). The fluorescence emission spectra were recorded using a spectrograph (Shamrock 163, Andor) and processed using the Andor Solis program.

3.5.9 Motility Assay

In 12 well plates, M9 medium in 1% (m/v) tryptone was used to make soft agar plates (0.25% m/v) with 5% glucose. Plates were left at room temperature over night to solidify. Samples of both BW25113 and MC4100 were grown in LB medium overnight at 37°C at 200 rpm. Once grown, cells were diluted to $OD_{600} \approx 1.0$. Then the plates were inoculated with the appropriate cell line with an inoculating needle. Care was taken in order to not touch the bottom of the plates to prevent movement underneath the medium. Plates were incubated at 30°C to observe different levels of motility growth. Images were taken using an Alpha Innotech AlphaImager Gel Imaging System.

3.5.10 Biofilm Growth Inhibition Assay

P. aeruginosa PA01 cells were grown in LB for 18 hours at 37°C with rotary shaking at 200 rpm. Cell growth was restarted in M63 medium supplemented with 0.4% arginine and 1 mM $MgSO_4$ to reach $OD_{600} = 0.5$ (4.0×10^8 cells/mL). 12-well plates were prepared either with coverslips for imaging or without coverslips for crystal violet assessment. 500 µL of M63 medium was supplemented with 4 µM stapled peptide where appropriate and mixed by shaking. Once completed, plates were placed at approximately 35° to allow slanted growth and biofilm monolayer formation. 2.0×10^6 cells were inoculated into each plate and incubated at 37°C for 5 hours (time was optimized in a range of 4 to 24 hours, data not shown). The supernatant and any planktonic cells were aspirated and the biofilm was washed twice with PBS. 625 µL of 0.1% crystal violet was added in each well. Plates were incubated at room temperature for 10-15 min. The crystal-violet mixtures was carefully aspirated and plates were washed twice with distilled water. Plates were dried for 1 hour and PA01 biofilms were formed at the air-liquid interface.

To quantify the monolayer of the biofilm formation, 625 µL of 30% acetic acid in water was added to each well. Plates were incubated for 10-15 min to extract the crystal violet from the biofilms. The stain was transferred to a new flat bottom 12 well plate. On a plate reader at 550 nm, the absorbance of each well was read.

To image the biofilms, the coverslips were removed from the 12-well plate and mounted using 50% glycerol in water on cover slides. Biofilm images were taken using a Zeiss Axiophot light microscope for phase contrast purposes on the 20X objective. Image acquisition was controlled with MetaView software.

3.5.11 General PCR conditions

The reaction mixture consisted of 11.65 µL sterile dH_2O, 5 µL 5X Buffer 4, 2 µL $MgSO_4$, 1 µL DMSO, 0.5 µL 10 mM dNTPs, 0.1 µL BSA, 1 µL 50 µM primer (F), 1 µL 50 µM primer (R), 0.25 µL Taq Polymerase, and 1 µL of the cDNA prepared. Thermocycler conditions were as follows: 1 cycle 95°C for 90 s; 30 cycles of 95°C 60 s, 53°C for 30 s, 72°C for 45 s; 1 cycle of 72°C for 300 s, then held at 10°C. To load on a 1% agarose gel, 5 µL 5X green buffer were added to each sample prior to loading on gels run at 100 V for 60 minutes. Gels were imaged using an Alpha Innotech AlphaImager Gel Imaging System.

3.5.12 RNA Extraction and cDNA Synthesis

Water was mixed with 0.1 v/v DEPC for 18 hours at room temperature to inactivate any trace RNases from the water. The mixture was autoclaved to decompose DEPC into carbon dioxide and ethanol and to prevent further protein inactivation for the water's future uses. BW25113 cells were grown overnight in LB medium at 37°C at 200 rpm. Cells were then diluted and regrown up until log phase at $OD_{600} \approx 0.5$. 1 x 10^8 cells/mL were isolated

and washed twice with TE buffer mixed in DEPC-treated water. Cells were centrifuged at 13 000 rpm for 60 s at room temperature. Stapled peptides (4 μM) were added to each sample as necessary and incubated at 37°C for 90 minutes. Again, cells were centrifuged at 13 000 rpm for 60 s at room temperature and washed once with TE buffer. Pellets were incubated at 4°C for 30 minutes.

Promega's SV Total RNA Isolation System was used to isolate RNA from the cells. Samples were examined through nanodrop to assess the purity. The RNA was either stored at -80°C or used immediately for cDNA synthesis. Bio-Rad's iScript cDNA Synthesis Kit was used to convert RNA to cDNA with M-MLV Reverse Transcriptase. The following cycling procedure was used to synthesize the cDNA: 25°C for 5 minutes, 42°C for 30 minutes, and 85°C for 5 minutes to heat inactivate the reverse transcriptase, and a 4°C cooldown. The resulting cDNA was amplified using primers of interest to determine the presence and purity of the cDNA from negative controls to ensure that genomic DNA is no longer present in the sample. Thermocycler conditions were as follows: 1 cycle 95°C for 90 s; 30 cycles of 95°C 60 s, 56°C for 30 s, 72°C for 45 s; 1 cycle of 72°C for 300 s, then held at 4°C. Samples were stored at -20°C for further use.

3.5.13 Relative quantitative PCR

To prepare the qPCR experiment, cDNA dilutions were made in TE buffer (10 mM Tris, 0.1 mM EDTA), pH = 8. For every 8 reactions, the following mixture was necessary for a gradient PCR temperature assessment: 84 μL 2X SsoFast EvaGreen Supermix (dNTPs, Sso7d fusion polymerase, $MgCl_2$, EvaGreen dye, stabilizers), 1.7 μL 10 μM Primer F (50 μM), 1.7 μL 10 μM Primer R (50 μM), 8.4 DNA template, and 72.2 μL water with 20 μL being the final reaction volume. Thermocycler conditions were as follows: 1 cycle 98°C for

180 s; 40 cycles of 95°C 10 s, 52-62°C for 60 s, 72°C for 30 s; 1 cycle of 65°C for 5 s, then a gradual increase to 95°C at a rate of 0.5°C per 5 s, followed by a plate read. PCRs were conducted on Bio-Rad's CFX96 Touch Real-Time PCR Detection System and data was analyzed on the Bio-Rad CFX Manager software.

3.5.14 Digital Droplet PCR

For the digital droplet PCR experiments, much like the qPCR experiments, cDNA dilutions were made in TE buffer. The cDNA template for 16S experiments was diluted 1:9 based on qPCR data. All other primers were analyzed straight from the cDNA samples. A master mix was made with the following volumes per reaction: 3.0 µL cDNA, 0.4 µL forward primer (stock of 10 µM), 0.4 µL reverse primer (stock of 10 µM), 11 µL 2x QX200 ddPCR EvaGreen Supermix, and 7.12 µL water. To create the droplets, 20 µL of reaction mixture and 65 µL of oil were used. Droplets were made using Bio-Rad's QX200 Droplet Generator at 1000 droplets/µL. 40 µL of droplets were transferred to a PCR plate and underwent the following PCR cycle on the QX200 Droplet Digital PCR System: 1 cycle 95°C 300 s, 40 cycles of 95°C 30 s and 56°C 60 s at 2°C/s ramp, and 4°C for 300 s, 90°C for 300 s, and 4°C hold. Data was analyzed using Bio-Rad's QuantaSoft software.

Appendix A: Oligomer Sequences

A.1 DNA sequences for nanoparticle DNA-functionalization

Table 2. glnA -24 sequences designed for AuNP functionalization and FLIM

Name	Sequence (5'→3')
GG-24 Cy5 Template	5AmMC6-CGCCTTTAAAAGTTGGCACAG-Cy5-TTTCGGCG
GG-24 Cy5 Complement	CGCCGAAATCTGTGCCAACTTTTAAAGGCG
GG-24 Cold Template	5AmMC6-CGCCTTTAAAAGTTGGCACAGATTTCGGCG
GG-24 Cold Complement	CGCCGAAATCTGTGCCAACTTTTAAAGGCG
AA-24 Cy5 Template	5AmMC6-CGCCTTTAAAAGTTAACACAG-Cy5-TTTCGGCG
AA-24 Cy5 Complement	CGCCGAAATCTGTGTTAACTTTTAAAGGCG
AA-24 Cold Template	5AmMC6-CGCCTTTAAAAGTTAACACAGATTTCGGCG
AA-24 Cold Complement	CGCCGAAATCTGTGTTAACTTTTAAAGGCG

A.2 Primer sequences for PCR transcriptional detection

Table 3. BLAST designed inserts less than 500 base pairs in length for qPCR & ddPCR analysis

Name	Size	Sequence (5'→3')	Tm (°C)
16S Forward	493 of 1541	TGATACTGGCAAGCTTGAGT	56.84
16S Reverse		TGGCAACAAAGGATAAGGGT	57.01
glnAp2 Forward	475 of 1410	CAAAATGTTTGACGGCTCCT	56.91
glnAp2 Reverse		CAGACCCATCTGTTCCATCA	56.91
pspA Forward	466 of 669	TCGTGAATGCCAACATCAAC	57.01
pspA Reverse		ATTGCTTCATCCAGTTTGCC	56.96
atoD Forward	459 of 663	GTGGGCGGATTTATGGGGAT	59.89
atoD Reverse		CGGGCGCTAAGTTGATAGGT	59.90

Chapter 4

FtsZ-based Stapled α-helical Peptides as a Possible Antibiotic Therapeutic

4.1 Introduction

In this chapter, we discuss the design, synthesis, and preliminary testing of a stapled peptide inhibiting the binding domain of FtsZ in the efforts to develop a stapled peptide acting directly as an antibiotic. Many PPIs within the bacterial divisome have not been successfully targeted due to their complex interactions. The ZipA-FtsZ binding interface severs to anchor the Z-ring; interruption of this contractile ring will inhibit cytokinesis.

4.1.1 FtsZ-ZipA Binding Complex

The first crystal structures of the FtsZ protein elucidated were those of *Methanococcus jannaschii*.[1] Further binding studies in *E. coli* have demonstrated the importance of the C-terminus in FtsZ.[2,3] Most FtsZ homologs have two main activity regions. The N-terminal globular region of 320 residues is divided into two domains: one for GTPase activity bound with GDP, demonstrated through studies demonstrating GTP-to-GDP conversion,[4] and the other for the longitudinal assembly of 30-50 FtsZ units assembled in long stacks called protofilaments, demonstrated through cryoelectron microscope studies.[5] Protofilaments assemble at the divisome together to form the Z-ring.[5] To catalyze each addition, two monomers of FtsZ-GTP orient themselves in which one catalyzes the GTP hydrolysis of the other into GDP and unreleased inorganic phosphate.[6] Once hydrolyzed, the two monomers are connected to form a dimer-GTP complex, ready for both catalysis and further polymerization.[6]

Mosyak *et. al* have taken great strides to characterizing the ZipA-FtsZ binding complex through both x-ray crystallography and alanine mutation studies from *E. coli* homologs. The C-terminal end, a domain containing a highly conserved set of 17 terminal

amino acids, has been studied in the context of ZipA (*PDB*: 1F47). When bound to ZipA/M185 (ZipA residues 185-328), it adopts a β-sheet (^{367}KEP**DYL**D^{373}) followed by an α-helix (^{374}**I**PA**FL**RK**Q**AD^{383}), with bolded letters indicating important binding residues.[2] The hydrophobic surface of ZipA contacts include both hydrophobic and hydrogen bonding between the backbones of the molecules. FtsZ's β-sheet connections include Asp370, Tyr371, and Leu372.[2] Interactions crucial to the α-helix binding with ZipA include Ile374, Phe377, and Leu378, with Gln381 binding to a lesser degree.[2] These contacts are distributed over six separate domains of ZipA and FtsZ forms no other bonding interactions aside from the C-terminal tail.[2] One main intrahelical hydrogen bond formed is between Pro369 and Tyr 371. Alanine mutational studies demonstrated similar binding results with surface plasmon resonance-based assay in which ZipA.[2] On a biosensor chip, ZipA was covalently immobilized through amine coupling chemistry. The FtsZ peptide variants were injected over the chip and the binding between both proteins resulted in a change in the SPR signal.[2]

4.1.2 Functional design of FtsZ stapled peptides

Our goal was to design an FtsZ-based stapled α-helical peptides that would act as an antibiotic by disrupting the protein-protein interaction between the FtsZ-composed Z-ring and ZipA (**Figure 4.1**). This binding region is associated with the C-terminus of FtsZ and is required for membrane constriction and cell division. As the binding of the concentric ring is inhibited, the peptides are expected to prevent cell division and cause longer cells that will ultimately die from a lack of sustainable resources. Hypothetically, the peptides should act in a bacteriostatic manner at the beginning, followed by bactericidal action later on. Cell death does present resistance problems as it will apply a strong evolutionary pressure comparable to current antibiotics. The value in introducing a stapled peptide variant is due

to its enhanced drug characteristics. The hydrocarbon staple will prevent native enzymes from degrading these peptides easily while enabling near permanent α-helicity. Furthermore, since this is a new mechanisms for antibiotic activity no known genes in the current resistome will aid in development of resistance. It is therefore expected that these compounds will function well against multidrug resistant bacteria.

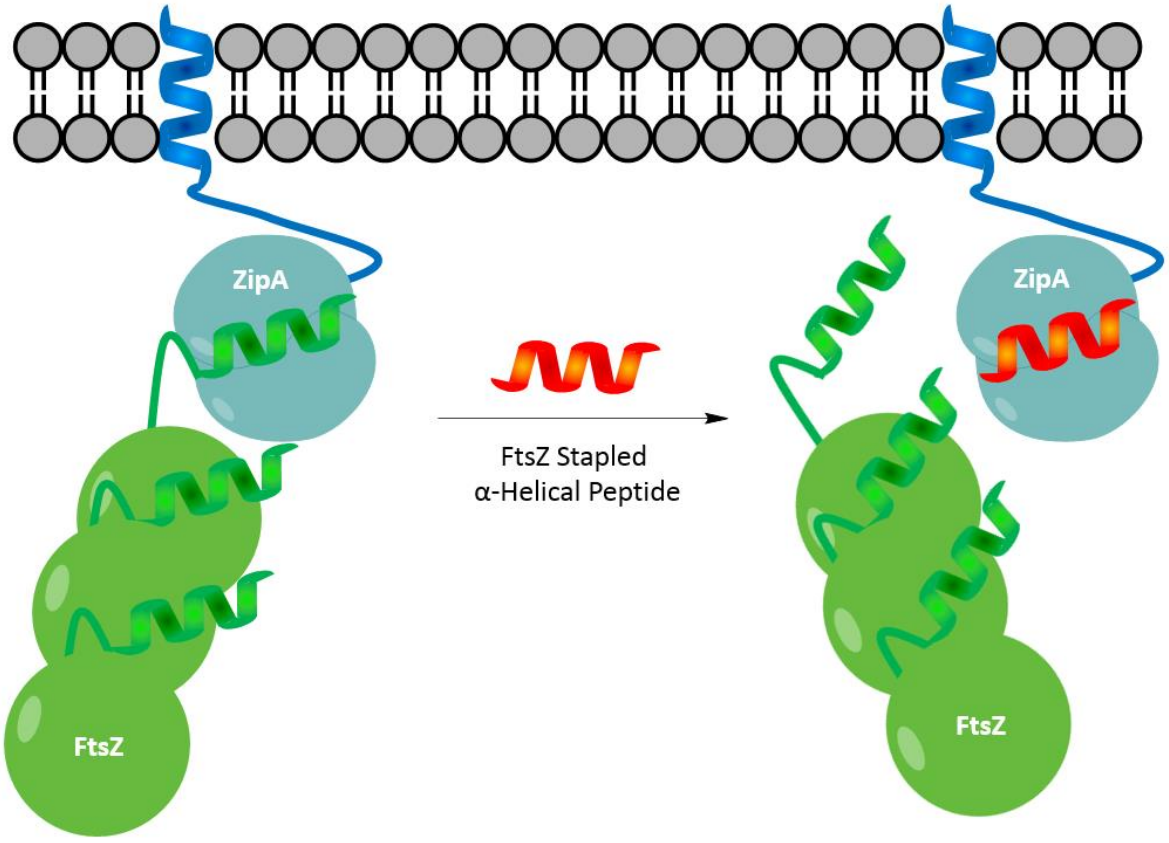

Figure 4.1. Schematic of FtsZ stapled α-helical peptide as it interrupts FtsZ polymerized Z-ring membrane attachment to ZipA.

4.2 Results and Discussion

4.2.1 First generation of FtsZ stapled peptides

4.2.1.1 Original peptide design and conceptualization

The terminal region of the FtsZ C-terminus was identified as a sequence of interest to mimic with a stapled peptide. From a structural standpoint, this type of target had not been previously explored as this region is a β-strand followed by an α-helix separated by a proline. The vast majority of stapled peptides are a single secondary structure element. In this case the proline separates the two secondary structure elements and directs the orientation of the helix relative to the β-strand. Investigation of this motif thus presented an exciting opportunity to expand the current stapled peptides toolbox.

```
N. gonorrhoeae IRTNRGIRTMNLTAADFDNQSVLDDFEIPAILRRQHNSDK
A. baumannii   INKRQNAENDVNNAPSSTPR--SSPMSIQDYLKNQQRK--
P. aeruginosa  VMRNQSHGSAATA-AKLNPQDDLDYLDIPAFLRRQAD---
P. mirabilis   VEESKPAAKAVNE-QSTQANKEPDYLDIPAFLRKQAD---
E. coli        TQEQKPVAKVVND-NAPQTAKEPDYLDIPAFLRKQAD---
K. pneumoniae  TQEQKPAAKVVND-NTPQTAKEPDYLDIPAFLRKQAD---
E. aerogenes   TQEQKPVAKVVND-NTPQTAKEPDYLDIPAFLRKQAD---
                   :    .             . :.*   *:.*
```

Figure 4.2. Sequence alignment of the C-terminal motif of FtsZ in a select number of bacteria. Both binding sites are conserved throughout multiple species of Gram negative bacteria. Blank spaces represent low levels of homology, periods represent partially homologous regions, colons represent highly homologous regions, and asterisks represent amino acids of consensus sequences. The green box depicts the sequence domain in which the peptide will imitate FtsZ's C-terminus. Sequences were generated from ClustalOmega.

Although some clinically relevant pathogens such as *Acinetobacter baumannii* lack a similar region to FtsZ, most Gram negative pathogens possess a highly homologous C-terminus (**Figure 4.2**). Stapled peptides based on this conserved sequence should thus be able to exert fairly broad spectrum antibiotic activity. Examination of the sequence shows that isoleucine, leucine, and glutamine are highly homologous across many key pathogens,

with the arginine and lysine areas being retained for positive charge interactions. As the identified sequence homolog has been studied in *E.* coli, the peptides sequences generated will be modeled according to this organism's FtsZ sequence.

Identification of the placement site for staples is a key consideration in development of stapled peptides. The region highlighted in **Fig. 4.2** would adopt a β-strand structure for the residues DYLDI and an α-helix for the remaining residues (i.e. PAFLRKQAD). Replacing the Pro residue with a staple was cautiously considered as its effects are unpredictable; this may lead to a change in the predicted N-terminal structure and these residues should be considered as a potential for α-helical character. Based on the helical wheel diagram of the C-terminal residues we identified 4 sites for staple incorporation and designed 4 stapled α-helical peptide mimics of FtsZ (**Figure 4.3**).

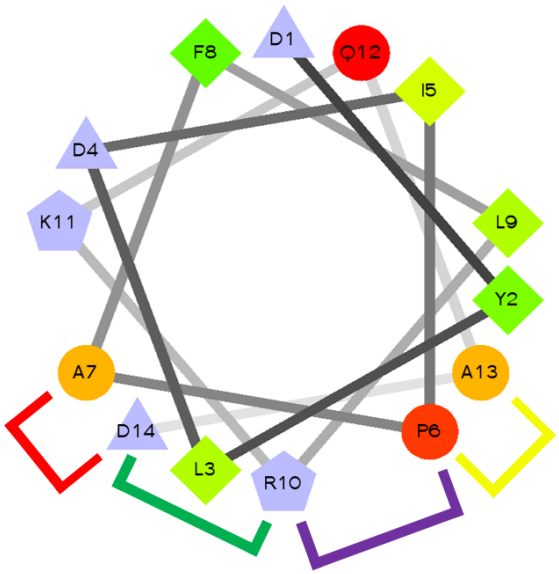

Figure 4.3. Helical wheel diagram of the FtsZ C-terminal α-helix with hypothetical staples placed within the wheel. The amino acid sequence corresponds to the protein sequence DYDLIPAFLRKQAD. Hydrophilic residues are circles whereas hydrophobic ones are diamonds. Potentially negatively charge amino acids are triangular and positively charge ones are pentagons. Charged residues are in blue, hydrophobic residues in green, moderately hydrophilic residues in yellow and strongly hydrophilic residues are in orange. The Red staple represents the staple for C-long, green for C-short, yellow for P-long, and purple for P-short. Helical wheel was generated by wheel.pl.

Due to the short nature of this α-helical domain of this sequence (8 amino acids in length), few choices are available for the peptide in both *i*, *i*+4 and *i*, *i*+7 combinations. However, based on previous binding studies and related x-ray structure, it is possible to set binding positions between either α-helix ends by replacing the proline and the corresponding terminal aspartic acid. As the only other peptide successfully tested in bacteria is the σ^{54} peptide, a variety of peptide analogs were synthesized to further investigate the effects of stapled peptides in bacteria.

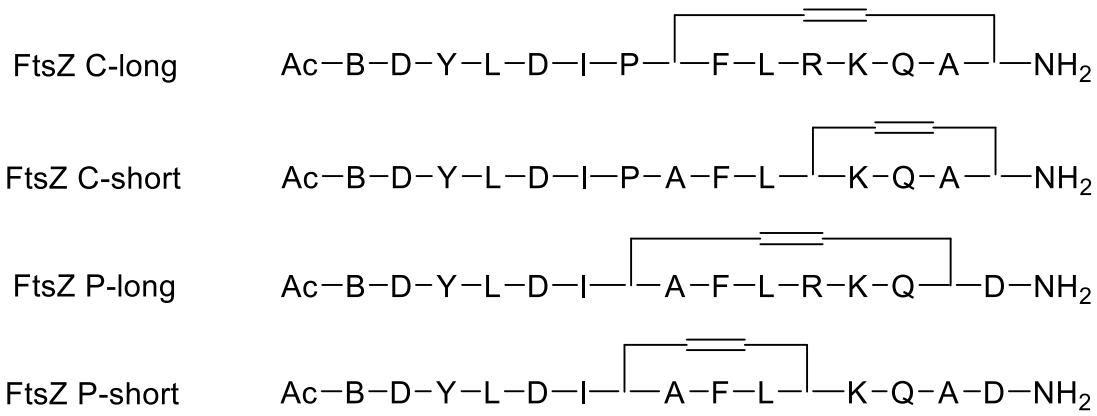

Figure 4.4. Acetyl-capped chemically synthesized FtsZ C-terminus stapled α-helical peptide analogs designed with varying staple length. B represents a β-alanine spacer and the staple-like structure represents the locations of each staple within the peptides.

4.2.1.2 Peptide chemical synthesis

All FtsZ stapled peptides were synthesize in the Bernal lab at the NIH using a TETRAS peptide synthesizer from Advanced ChemTech. The procedure use was the same as that of the SPPS method developed for the σ^{54} peptides. In brief, Rink amide resin was used to grow the peptides in the C to N direction. This direction was specifically used to allow the N-terminus of the peptides to be grown with Fmoc protecting groups and selectively functionalized at the terminal position. As the amino acid R groups lacked Fmoc in their protecting groups, this would confer specific functionalization at the terminal

position once cleaved while allowing the rest of the peptide to remain protected. The general principles of SPPS are to repeat the cycles of wash-couple-wash-deprotection. (Refer to **Fig. 3.5** for synthetic scheme). By adding HCTU and DIPEA to increase the coupling reactivity, each monomer was added sequentially until fully grown. Depending on the purpose of the peptide, it was capped either using acetic anhydride or with fluorescein and cleaved from the resin using standard TFA-mediated cleavage. The crude peptide was purified by HPLC and characterized by high-resolution mass spectrometry. The final mass was taken and the peptides were analyzed by nanodrop to ensure purity. In all cases, peptides of greater than 95% purity were obtained.

4.2.1.3 Minimum Inhibitory Concentration & Flow Cytometry

These peptides were designed to inhibit the replication of Gram negative bacteria. It is necessary to determine whether cells exhibit bacteriostatic characteristics at appreciable concentrations. To assess the peptide's antimicrobial activity, we used a modified version of the broth microdilution method of clinical MIC assay from the National Committee for Clinical Laboratory Standards.[7]

Table 4: MIC Results of First Generation of FtsZ stapled peptides in BW25113 *E. coli* using the Microdilution Method (n = 3)

Peptide	MIC (μg/mL)
Wild-type	>512
P-short	>512
C-long	>512
P-long	>512

Based on this data set, the peptides show no antimicrobial activity. Although this does not show promise as an antimicrobial agent at this time, the lack of activity may be

attributed to two separate factors. The peptide may not have activity based on design, meaning that the hypothesis is flawed in such a way that the peptide does not selectively bind to the target or the target is not an appropriate antibiotic target. However, another reason could be that the peptides lack cell penetration ability due to the nature of the molecule's polarity or other penetration-linked characteristics. Based on the MIC values, it is impossible to derive the exact cause of the lack of activity.

As with the RpoN designed σ^{54} peptides, flow cytometry was used to evaluate the ability of the peptides to penetrate bacterial cells. Flow cytometry data for the first generation of FtsZ stapled peptide analogs displayed little to no increase in fluorescence signal indicating that the peptides did not cross the bacterial membrane (data not shown). Currently, the working hypothesis is that the peptides cannot penetrate cells due to their inherent negative charge at physiological pH.

4.2.2 Second generation of FtsZ stapled peptides

4.2.2.1 Peptide sequences

To remedy this situation of impenetrability, a second generation of peptides was synthesized to determine the cause of the lack of peptide uptake. To improve membrane permeability, the negatively charged amino acids were replaced with polar neutral amino acids (**Fig. 4**) to decrease the effects of repulsion between the peptides and cell membranes.[8] As such work has successfully resulted in peptides retaining activity in previous examples of antimicrobial peptides, it was the first course of action to take. These peptides were synthesised, purified, and characterized following similar protocols to the first generation FtsZ stapled peptides.

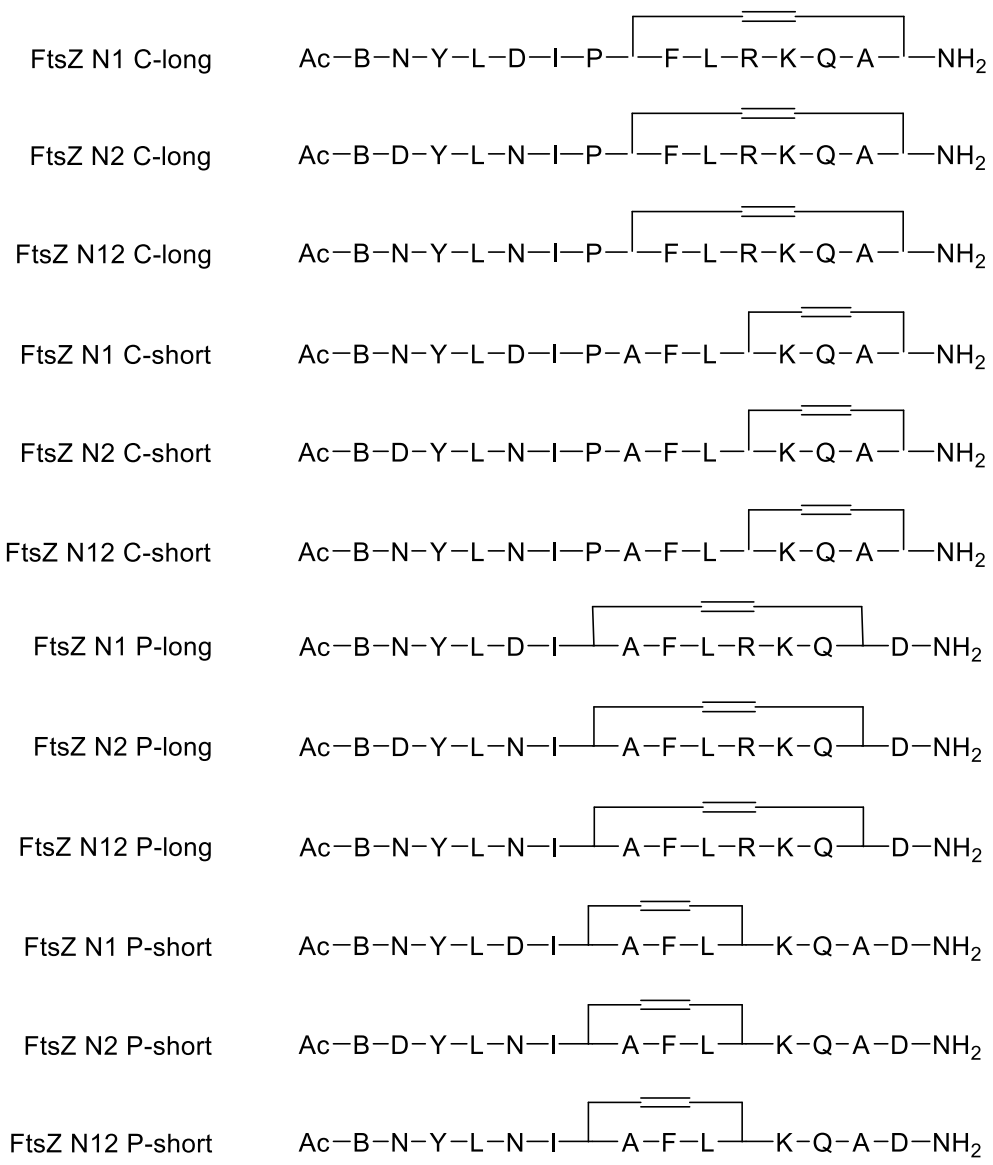

Figure 4.5. Second generation acetylated sequences of FtsZ stapled α-helical peptides designed with a lower negative charge through aspartic acid to asparagine substitution. B represents a β-alanine spacer and the staple-like structure represents the location of each stapled with each peptide.

4.2.2.2 Minimum Inhibitory Concentration Analysis

The peptides were tested for antimicrobial properties again through the clinical minimal inhibitory concentration (MIC) assay from the National Committee for Clinical Laboratory Standards.[7] The protocol used was the same one as described for previous experiments.

Table 5: MIC Results of Second Generation of FtsZ stapled peptides in BW25113 *E. coli* using the Microdilution Method (n = 3)

Peptide	MIC (µg/mL)
N1 P-short	>512
N1 C-long	>512
N1 P-long	>512
N2 P-short	>512
N2 C-long	>512
N2 P-long	>512
N12 P-short	>512
N12 C-long	>512
N12 P-long	>512

Again, the peptides showed no antimicrobial activity. This leads to a similar problem as before; the peptides may lack activity or lack cell penetration. This question can be most easily answered with flow cytometry.

4.2.2.3 Flow cytometry

By making use of FITC-tagged peptides, the events collected from the flow cytometry data would indicate whether an event has green fluorescence compared to cells without green fluorescence. By making use of its individual event detection, it is possible to determine the percentage of cells that take up the peptide. Each peptide under investigation through flow cytometry was tagged with FITC, whose excitation is 488 nm and emission is 525 ± 20 nm. All the work discussed was done on a Beckman Coulter Gallios Flow Cytometer. This experiment used the same parameters as that previous experiments with the σ^{54} peptide used in order to examine the cell profiles. The gates were used to assess permeability (cell plots not shown).

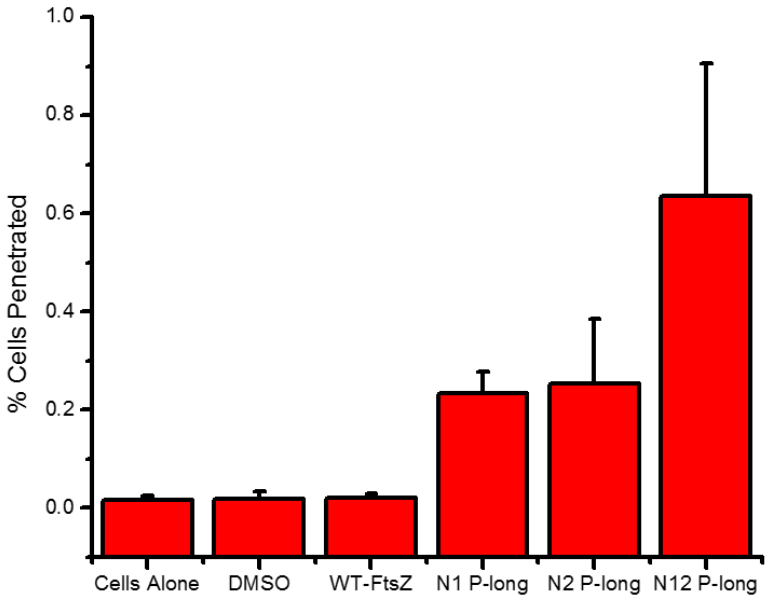

Figure 4.6. Flow cytometry histogram analysis of BW25113 cells treated with 4 μM FITC-tagged FtsZ peptide analogs in 0.4% DMSO (n = 3, error bars = SD). Two-way ANOVA statistical analysis was conducted with the Bonferroni post-tests to determine significance in all peptide penetration compared to the DMSO vehicle control.

Based on the data, it appears that the peptides fail to enter cells. The doubled aspartic acid-to-asparagine peptide seems to penetrate cells more easily due to the lack of the second negative charge. However, the peptides penetrate less than 1% of the total population and therefore the overall utility of the data is statistically insignificant (p-value > 0.05) relative to the vehicle control.

The double knockout seems more promising and thus charge may play a role in the penetration ability of the peptides. Further efforts to increasing the positive charge of the peptides should be investigated. A third generation of peptides with various placements of positive charge either replacing non-binding amino acids or as terminal additions to either the N or C ends of the peptides may be investigated.

4.3 Conclusions and Prospects

To validate the viability of interrupting the FtsZ-ZipA complex, a stapled peptide with penetration ability must be designed and tested. One proven method of increasing cell permeability in Gram negative pathogens is through the use of siderophore-conjugated antibiotics.[9] These iron chelators are used by bacteria to transport iron through the bacterial cell membrane in iron-poor environments such as during human infection.[10]

Further studies in circular dichroism should be conducted to determine the peptide's α-helix and β-sheet content. It may be that the secondary structure is not adopting the α-helical configuration with the addition of the staples. It appears that the FtsZ peptides cannot access bacteria through diffusion. At this time, due to the peptide's negative charge, the cell membranes could be repelling the peptides and a positive charge may be needed.

Once the peptide has demonstrated permeability via flow cytometry and microscopy, mammalian cytotoxicity can be evaluated through a similar assay to **3.5.3**. If the peptide demonstrates low mammalian toxicity, the GTPase activity of the cell could be measured to determine if the peptides are inhibiting the Z-ring's contractile activity. Further studies in the binding affinity of each peptide may be examined to understand more about the specificity of stapled peptides in bacterial models.

4.4 References

1. Löwe, J. & Amos, L. A. Crystal structure of the bacterial cell-division protein FtsZ. *Nature* **391,** 203–206 (1998).

2. Mosyak, L. *et al.* The bacterial cell-division protein ZipA and its interaction with an FtsZ fragment revealed by X-ray crystallography. *EMBO J.* **19,** 3179–3191 (2000).

3. Nogales, E. *et al.* Structure of αβ tubulin dimer by electron crystallography. *Nature* **391,** 199–203 (1996).

4. De Boer, P. *et al.* The essential bacterial cell-division protein FtsZ is a GTPase. *Nature* **359,** 254–256 (1992).

5. Huecas, S. *et al.* Energetics and geometry of FtsZ polymers: nucleated self-assembly of single protofilaments. *Biophys. J.* **94,** 1796–1806 (2008).

6. Scheffers, D. J. & Driessen, A. J. The polymerization mechanism of the bacterial cell division protein FtsZ. *FEBS Lett.* **506,** 6–10 (2001).

7. Cockerill, F. R. *et al. Methods for Dilution Antimicrobial Susceptibility Tests for Bacteria That Grow Aerobically ; Approved Standard — Ninth Edition.* **32,** (2012).

8. Bernal, F. *et al.* Reactivation of the p53 tumor suppressor pathway by a stapled p53 peptide. *J. Am. Chem. Soc.* **129,** 2456–2457 (2007).

9. Ji, C. *et al.* Iron transport-mediated drug delivery: Practical syntheses and in vitro antibacterial studies of tris-catecholate siderophore-aminopenicillin conjugates reveals selectively potent antipseudomonal activity. *J. Am. Chem. Soc.* **134,** 9898–9901 (2012).

10. Hider, R. C. & Kong, X. Chemistry and biology of siderophores. *Nat. Prod. Rep.* **27,** 637–657 (2010).

4.5 Experimental

4.5.1 Solid-Phase Peptide Synthesis

All amino acids were Fmoc protected at the N-terminus for C to N peptide synthesis. To begin, the TETRAS was purged with three 50 mL washes of NMP. To make 3.0 x 10^{-5} moles of peptide, 103 mg of Rink amide resin (resin substitution = 0.29 mmol/g) were weighed and loaded into wells. Amino acid solutions (0.3 M) were made on a 10X scale to ensure near perfect coupling. Terminal alkene amino acids were dispensed on a 5X scale. The two crosslinking amino acids used were the Fmoc-S5-OH (Fmoc-(S)-2-(4'-pentenyl)Ala-OH) and Fmoc-R8-OH (Fmoc-(R)-2-(7-octenyl)Ala-OH). HCTU (0.3 M) was used as the peptide coupling reagent (0.123 g per reaction). DIPEA (0.3 M) was used to activate the C-terminal ends of the amino acids. All reactions were performed at room temperature as the TETRAS lacked a temperature control chamber. As a result, all the reactions had extended reaction times to fully react with the resin.

When adding one amino acid to the resin, the usual procedure is to couple, wash, deprotect, wash, and repeat with each monomer addition. To couple, 1 mL of amino acid solution (10X), 0.99 mL HCTU, and 2 mL DIPEA solution were mixed for 60 minutes. For all washes, 3 mL DCE was used to wash the resin 3 times for 3 minutes. For the Fmoc deprotection step, 3 mL of 25% piperidine in NMP was mixed for 2 minutes, then purged and repeated for 20 minutes. In the case of the unnatural crosslinking amino acid, the deprotection step was repeated an extra cycle to ensure that the protecting group was gone due to the amino acid's lowered reactivity. For short staples, two S5 amino acids were used. For long staples, the S5 amino acid was added first, followed by the R8 amino acid. Crosslinkers were coupled at 5X couplings with half the normal reagents. However, the

coupling was performed twice so the overall coupling amount is the same as normal amino acids. For the amino acids loaded onto crosslinker amino acids, the coupling time was doubled to 120 minutes due to the crosslinker's lower reactivity.

To form the ring closing cyclization or "stapled" portion of the peptides, the resin loaded with peptide was swelled for 15 minutes in 3 mL NMP. Afterwards, the resin was washed with DCE. 3 mL of Grubbs I catalyst (5 mg/mL) was used to catalyze the olefin metathesis and reacted for 6 hours. The six hour reaction was repeated twice for a total of 18 hours. Once metathesized, the resin was washed four times with DCE for 3 minutes (4 mL). The compounds either remained on resin without deprotection or were capped with either acetyl groups or FITC-functionalized amino acids. To preserve the peptides, the resin was washed four times with 4 mL DCE for 3 minutes and shrunk four times with 3 mL of methanol for 5 minutes per wash.

For acetylation, the resin was swelled for 15 minutes with NMP. Fmoc deprotection was done with 25% piperidine in NMP twice: 3 mL for 2 minutes and 3 mL for 20 minutes. After washing with NMP, 1mL of 100% acetic anhydride, 0.5 mL DIPEA, and 1.5 mL NMP were mixed and added to the resin for 60 minutes. Once completed, the resin with loaded peptide was purged, washed, and shrunk with the methanol wash.

For fluorescein capping, the resin was swelled for 15 minutes with NMP. The resin was mixed with of 0.2 mL DIPEA and 2.8 mL FITC (10 mg/mL) for 12 hours. After purging the solution, the resin loaded with FITC-tagged peptide was washed with DMF, DCM, and shrunk with methanol for storage.

Peptides were fully deprotected and cleaved from the resin with a mixture of TFA : TIPS : H_2O (19.0 : 0.5 : 0.5). This TFA cleavage cocktail was added to the resin and stirred for 3 hours at room temperature. Afterwards, a 1:1 mixture of MTBE:hexanes was added to precipitate the peptides as they are polar. Once completed, the peptides were spun down at 4°C for 14 000 rpm for 15 minutes. After pelleting the peptides, a mixture of 1:1 acetonitrile:water was used to solubilize the peptides. Stapled peptides were purified by HPLC/MS and then quantified by both mass and UV spectroscopy. All collected fractions were analyzed by mass spectrometry to determine the presence of each peptide. Once a fraction was deemed to have the peptide, the fractions were pooled together, aliquoted, lyophilized, and stored at -20°C.

4.5.2 Minimum Inhibitory Concentration

From a frozen stock of cells, a plate of BW25113 *E. coli* (Keio collection) cells was streaked on LB-agar medium and grown overnight at 37°C for 18 hours. A seed culture was taken from the plate and grown overnight in Müeller-Hinton Broth (MHB). Cells were diluted to $OD_{600} \approx 0.1$ with MHB as this will concentrate the *E. coli* to 1 x 10^8 cells/mL to allow cells to regrow into log phase. Cells were incubated at 37°C, shaking for 200 rpm, for 40 minutes (2 doubling times) to allow cells to reach log phase ($OD_{600} \approx 0.4$-0.6). Cells were again diluted to $OD_{600} \approx 0.1$ with MHB. Beginning at a concentration of 1024 μg/mL, a 96 well plate was prepared. Solutions were diluted by a factor of 2 with a constant volume of vehicle. Once fully diluted to 2 μg/mL, 2.5 x 10^5 cells were added. After sealing the plate with parafilm, cells were incubated for 18h while shaking at 50 rpm for 37°C. Visual imaging and plate reader assays were used to determine the MIC of each peptides with $OD_{600} \approx 0.04$ as a background value.

4.5.3 Flow Cytometry

Please note that this protocol differs slightly from the one used for σ^{54} stapled α-helical peptide studies. From a streaked out plate, BW25113 and PA01 cells were seeded and grown overnight. The following day, cells were diluted to OD ≈ 0.1 and grown in LB medium for approximately 40 min to enter the log phase of growth. 1×10^8 cells were used in each treated sample. Cells were centrifuged at 13 000 g for 60s at 25°C and washed twice and resuspended in 500 μL of PBS. Stapled peptides were incubated with the bacteria at 37°C for 90 min to a final concentration of 4 μM. After washing once with PBS like before, the bacteria were resuspended with PBS again and 0.4% (w/v) Trypan Blue to quench extracellular fluorescence. Finally, cells were washed and resuspended in 500 μL to be placed within the flow cytometer. The following voltages were used on the flow cytometer to determine cell population localization: side scatter at 253 ADC, forward scatter at 213 ADC, and FL1 at 550 ADC.